STUDIES OF ELECTRON CLOUD GROWTH AND MITIGATION AT CESR-TA

A Dissertation

Presented to the Faculty of the Graduate School

of Cornell University

in Partial Fulfillment of the Requirements for the Degree of

Doctor of Philosophy

by

Joseph Calvey

August 2013

STUDIES OF ELECTRON CLOUD GROWTH AND MITIGATION AT CESR-TA

Joseph Calvey, Ph.D.

Cornell University 2013

The electron cloud effect is a well known phenomenon in particle accelerators, in which a high density of low energy electrons builds up inside the vacuum chamber. These electrons can cause various undesirable effects, including emittance blowup and beam instabilities. Electron cloud has been observed in several currently operating machines, and is expected to be a major limiting factor in the design of the damping rings of future linear colliders. As part of an effort to understand and mitigate this effect, the Cornell Electron Storage Ring (CESR) has been reconfigured into a damping ring-like setting, and instrumented with a large number of electron cloud diagnostic devices. In particular, more than 30 Retarding Field Analyzers (RFAs) have been installed. These devices, which measure the local electron cloud density and energy distribution, have been deployed in drift, dipole, quadrupole, and wiggler field regions, and have been used to evaluate the efficacy of cloud mitigation techniques in each element. Understanding RFA measurements through the use of specially modified cloud buildup simulations results in a great deal of insight into the behavior of the electron cloud, and provides essential information on the properties of the instrumented chamber surfaces.

BIOGRAPHICAL SKETCH

Joe Calvey is a graduate student at Cornell University, and current affiliate at LBNL. His primary area of research is in the growth and mitigation of the electron cloud effect, as part of the CESR-TA program. He holds a Bachelor's degree from the University of Illinois Urbana-Champaign, and a Master's degree from Cornell.

This document is dedicated to mom.

ACKNOWLEDGEMENTS

The author is eternally grateful for the support and guidance received from M. Palmer, G. Dugan, D. Rubin, and M. Furman.

The results presented here were made possible by the hard work of the CESR-TA collaboration, especially L. Bartnik, M.G. Billing, J.V. Conway, J.A. Crittenden, M. Forster, S. Greenwald, Y. Li, X. Liu, R.E. Meller, S. Roy, S. Santos, R.M. Schwartz, J. Sikora, and C.R. Strohman. We are also grateful to S. Calatroni and G. Rumolo at CERN for providing us with the aC coated chambers, and S. Kato at KEK for the DLC chamber.

Finally, the author would like to thank the international collaborators who contributed to the CESR-TA RFA program: S. Calatroni, G. Rumolo, and C. Yin-Vallgren at CERN; S. Kato, K. Kanazawa, and Y. Suetsugu at KEK; K. Harkay and L. Boon at APS; M. Venturini and C. Celata at LBNL; M. Pivi and L. Wang at SLAC.

TABLE OF CONTENTS

LIST OF TABLES

LIST OF FIGURES

CHAPTER 1

INTRODUCTION

The electron cloud effect is a well known phenomenon in particle accelerators (see, for example, [27]), in which a high density of low energy electrons builds up inside the vacuum chamber. Typical densities are on the order of 10^{11} - 10^{12} e^- / m^3, and most electrons have energies less than a few hundred eV. These electrons can cause a wide variety of undesirable effects, including emittance growth and beam instabilities. These effects are particularly strong for positively charged beams with high intensity, low emittance and short bunch spacing.

The cloud is typically seeded by photoelectrons generated by synchrotron radiation, or by ionization of residual gas. The collision of these "primary" electrons with the beam pipe can then produce one or more ("secondary") electrons, depending on the secondary electron yield (SEY) of the material. If the average SEY is greater than unity, the cloud density will grow exponentially, until a saturation is reached. This process is illustrated in Fig. 1.1. Once the bunch train

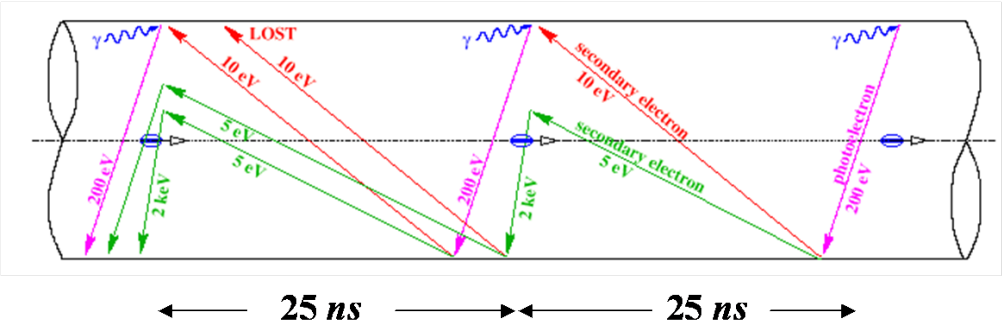

Figure 1.1: Illustration of the electron cloud buildup process (in the LHC), courtesy F. Ruggerio.

has passed, the cloud will typically decay away within a few hundred ns.

Electron cloud has been observed in many existing facilities (including, for example, PEP-II [4], CERN SPS [50], KEKB [48], ANL APS [25], FNAL Main Injector [24], and the LHC [21]), and is expected to be a major limiting factor in next generation storage rings. It is of particular concern in the damping rings of electron-positron colliders, which will produce a large amount of synchrotron radiation and require very small emittances [42].

In 2008, the Cornell Electron Storage Ring (CESR) was reconfigured to study issues related to the design of International Linear Collider (ILC) damping ring, including electron cloud. A significant component of this program, called CESR Test Accelerator (CESR-TA) was the installation of several retarding field analyzers (RFAs) throughout the ring, in drift, dipole, quadrupole, and wiggler field regions. A great deal of data has been collected with these detectors, in different beam conditions, over long periods of time, and in the presence of different cloud mitigation techniques. Through the use of specially modified cloud buildup simulations, these measurements have been analyzed on a quantitative level. These results have been presented in a series of conference and journal papers [5, 8, 12, 7, 11, 13, 10, 6, 9, 14]; in this thesis I hope to bring everything together into a coherent picture of electron cloud growth and mitigation in an accelerator.

The combined analysis of measurements and simulations allows us to characterize electronic properties (photoemission and secondary emission) of the surface of many portions of the vacuum chamber without resorting to external measuring devices. This process has the virtue that all surface conditioning effects due to the beam are intrinsically taken into account. Additionally, by com-

paring data and simulation on a detailed level we have substantially validated the electron emission model embodied in the simulation codes, and therefore reinforced our confidence in their applicability in other situations, in particular to hadron storage rings. Finally, we have been able to study several mitigation techniques in detail, and evaluate their effectiveness in preventing electron cloud build-up.

1.1 Electron Cloud

1.1.1 History and Motivation

Electron cloud has been known to exist in accelerators (although not always by that name) since the mid 1960's, when it was identified as a cause of a two-stream instabilities in the proton storage rings at BINP [22]. It was observed at other proton rings over the next 30 years, including the Argonne ZGS, BNL AGS, LBL Bevatron, CERN ISR, and LANL PSR [**?**].

The first discovery of electron cloud at a lepton machine occurred in 1995 at the KEK photon factory, where a coupled bunch instability was observed that behaved differently for electron and positron beams [33]. In particular, the positron beam instability was found to be very sensitive to bunch spacing, but was not eliminated by introducing a "clearing gap." It was eventually determined that this instability was caused by synchrotron radiation generated photoelectrons [39, 32], combined with secondary electrons, building up inside the vacuum chamber. The same effect lead to performance limitation in the PEP-II and KEKB B-Factories, which needed to employ cloud mitigations (namely antechambers, TiN coating and solenoid windings) to achieve their desired lu-

minosities.

Interest in electron cloud has remained high in the past 20 years. Dedicated EC experiments have been performed at several labs, including the Argonne APS, BEPC, SLAC PEP-II, KEKB, Fermilab Main Injector, and at CESR.

It was realized shortly after the "discovery" of EC that it could be a limiting factor in operation of the LHC. As a result, several preventative measures were adopted, including TiZrV coating in the warm sections, and a sawtooth structure (to reduce the specular photon reflectivity) in the cold sections. The LHC currently relies on beam scrubbing to achieve high luminosity with 50 ns spacing; at 25 ns spacing operation is still limited by EC [21]. This situation is likely to get worse with the LHC upgrade planned for later this decade, which will require high bunch charge, smaller emittance, and/or shorter bunch spacing. Electron cloud is also expected to be a limiting factor in next generation lepton colliders, such as the ILC or CLIC.

1.1.2 Mitigation Techniques

Many different mitigation techniques have been deployed to help reduce the electron cloud effect, or control any instabilities it causes. Among the most common and effective techniques are vacuum chamber coatings, which reduce the effective primary and secondary emission yield of the vacuum chamber. Coatings that have been used include titanium nitride (TiN, see Fig. 1.2) [38], amorphous carbon (aC) [50], diamond-like carbon (DLC) [35], and Ti-Zr-V non-evaporable getter (NEG) [47]. The latter coating also provides vacuum pumping, but must be activated at high temperature in situ, preventing its use in any

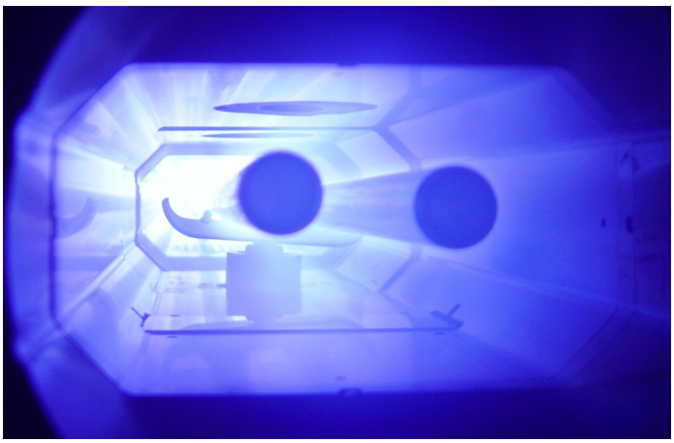

Figure 1.2: Glowing discharge during TiN coating of the grooved RFA beam pipe. The coating was performed in two stages, the first stage using two Ti rods (as shown) and the second stage with three rods (located in different transverse positions.) The two-stage coating is to minimize shadowing effects from the steeply grooved troughs.

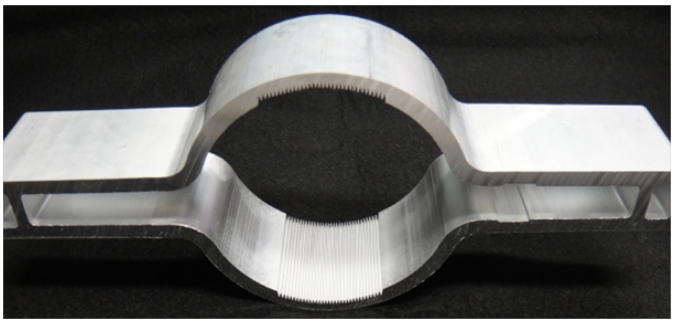

Figure 1.3: SuperKEKB vacuum chamber, with antechambers for absorbing direct synchrotron radiation.

cold sections of an accelerator.

In machines where photoelectrons are the primary seed for cloud growth, measures that reduce the effective photon flux near the beam can be effective. At KEK and PEP-II, antechambers have been used to capture the majority of direct synchrotron radiation generated electrons (Fig. 1.3). Similarly, at the LHC a sawtooth structure is used to reduce the specular reflection of the photons, keeping photoelectrons away from the beam.

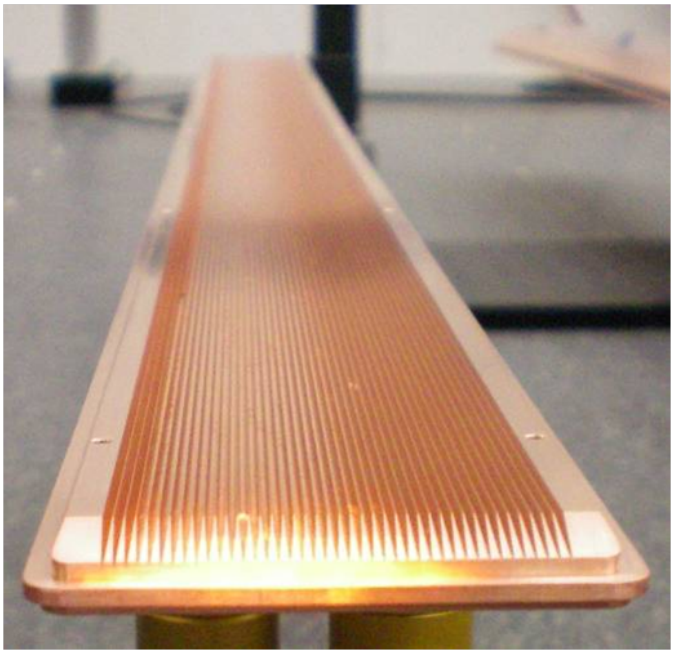

Figure 1.4: Grooved insert for CESR-TA wiggler.

In a dipole field, one can also use triangular grooves across the top and bottom of the vacuum chamber to suppress the effective primary and secondary emission yields (Fig. 1.4). Electrons generated inside the grooves will spiral around the field lines, and are likely to run into the groove before escaping into the vacuum chamber.

In a field free region, solenoid windings have been shown to be very effective at reducing cloud induced instabilities (Fig. 1.5). A low longitudinal field (on the order of 20 Gauss) is enough to trap the (low energy) secondary electrons near the vacuum chamber wall, safely away from the beam.

Finally, a "clearing electrode," which simply uses an electric field to push electrons toward the beam pipe wall, can be used to clear the vacuum chamber of electrons during the gaps between bunches (Fig. 1.6). An electrode energized with a few hundred volts can drastically reduce the cloud density seen by the

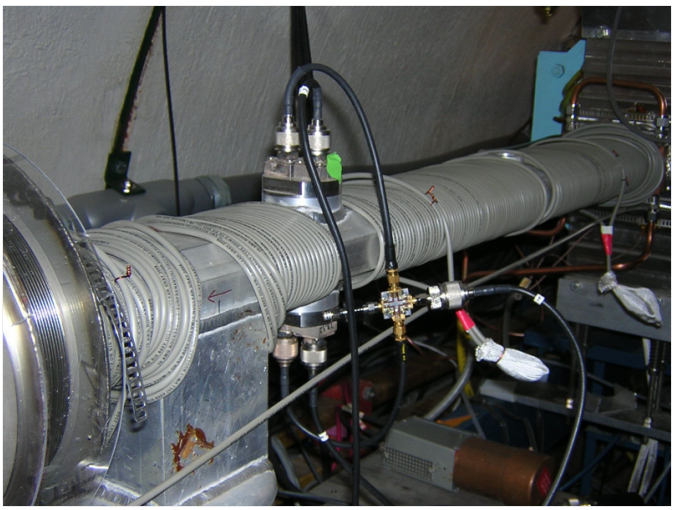

Figure 1.5: View of solenoid windings on one typical arc vacuum chamber.

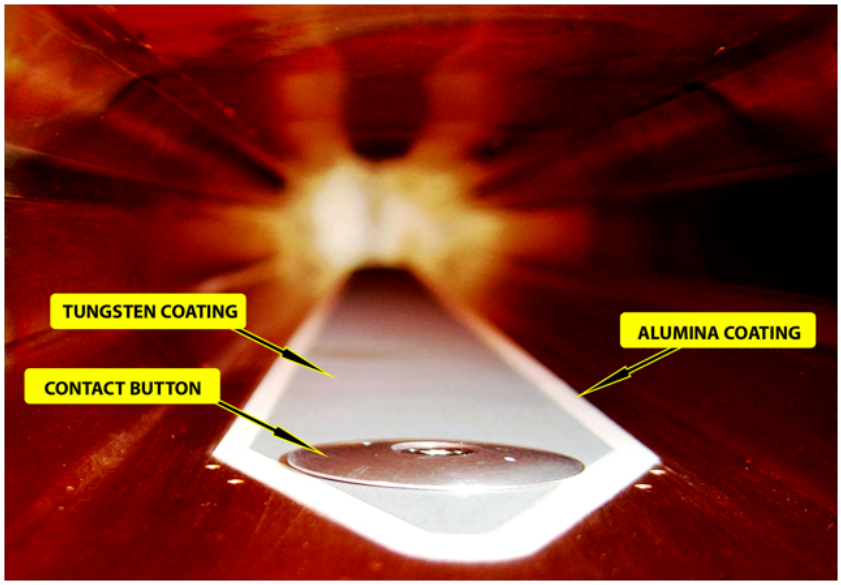

Figure 1.6: Photo of clearing electrode connection button on the bottom of a wiggler beam pipe.

beam, although there are some concerns about cost and long term viability of large scale application of this technique.

If no preventative measures are taken to mitigate the electron cloud in a machine, or if the measures taken prove insufficient, a few techniques can still be used to reduce the damaging effect of the cloud on the beam. The secondary

yield of many materials naturally decreases as the result of electron bombardment, in a process known as "scrubbing" or "processing." To take advantage of this effect, some machines (such as the LHC) make use of "scrubbing runs," in which as a very high beam current is stored in the machine for as long as possible, conditioning the machine before normal operation. If the cloud is still a problem, one can also increase the bunch spacing, or use strategic gaps in the train to allow the cloud to dissipate. And feedback systems can always be used to counteract any coupled-bunch instabilities that arise. Of course, as an ounce of prevention is worth a pound of cure, it is always better not to generate high cloud densities in the first place.

1.2 The CESR-TA Program

CESR-TA is an R+D program at Cornell, tasked with investigating issues related to the ILC damping ring. It has three main areas of research:

- Low emittance tuning
- Studies of electron cloud growth and mitigation
- Studies of electron cloud induced emittance growth and instabilities

1.2.1 CESR Conversion

In mid 2008 CESR was converted from a e+/e- collider to a damping ring configuration, for dedicated accelerator physics experiments. The largest part of this effort involved moving the arc wigglers to the L0 straight, and replacing

them with EC experiments. The wigglers were installed in the former location of the CLEO detector, where beams were collided for high energy experiments.

Seven sections of CESR have been instrumented with electron cloud detectors. They are:

- The L0 straight section, which contains three wigglers instrumented with RFAs (see Section 5.1).
- Long sections freed up by the removal of the wigglers at Q14E and Q14W (the names refer to their proximity to the 14E and 14W quadrupoles, respectively), used for early drift RFA studies (Section 2.1).
- Short drift sections at Q15E/W, designed to allow frequent swapping, to compare the effect of different mitigations.
- A long straight section at L3, containing a chicane of four dipole magnets (Section 3.1), a quadrupole instrumented with an RFA (Section 4.1), and a several meters of NEG coated pipe (Section 2.1.3).
- In 2011, one of the L0 wigglers was moved to the Q19E arc section, to study the development of the cloud in a wiggler in a more standard photon environment.

The vacuum chambers at Q15E/W are approximately elliptical and made of aluminum (as is most of CESR), while the chambers at L0 and Q14E/W are rectangular and made of copper, and the pipe is circular stainless steel at L3. Fig. 1.7 shows the locations of these experimental sections in the CESR ring, and Table 1.1 gives a list of RFAs at each location.

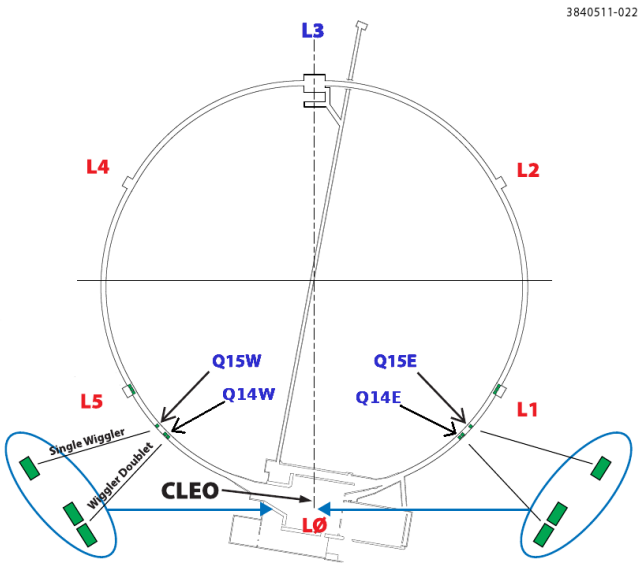

Figure 1.7: The reconfiguration of the CESR vacuum system provided space for several electron cloud experimental sections. RFAs are located at L0, Q14E/W, Q15E/W, Q19E, and L3.

Location	Field	RFA Type	Material	Shape
L0	Wiggler	Wiggler	Cu	Rectangular
12W	Dipole	Thin	Al	Elliptical
14W	Drift	Ins., APS	Cu	Rectangular
15W	Drift	Thin, Ins. II	Al	Elliptical
48W	Quad	Quad	Al	Circular
L3	Dipole	Chicane	Al	Circular
L3	Drift	APS	SST	Circular
19E	Wiggler	Wiggler	Cu	Rectangular
15E	Drift	Thin, Ins. II	Al	Elliptical
14E	Drift	Ins.	Cu	Rectangular

Table 1.1: List of RFA locations. Detailed descriptions of the various RFA styles are given in their respective chapters. "Material" refers to the base material; some locations have tested one or more mitigations. The vacuum chambers at all locations are 4.5 cm in height by 2.5 cm in width, with the exception of the circular chambers, which are 4.5 cm in radius.

CESR Parameters

The primary advantage of CESR as a test accelerator is its flexibility. At CESR-TA , we have been able to study the behavior of the electron cloud as a function of several different beam parameters, varying the number of bunches, bunch current, bunch spacing, beam energy, and species. As will be described in Section 2.5, this is very helpful for independently determining the photoelectron and secondary electron properties of the instrumented chambers. Table 1.2 gives some of the basic parameters of CESR, and lists some of the beam parameters used for electron cloud mitigation studies with RFAs. A more complete description of the full operating range of CESR can be found in [44].

1.2.2 Low Emittance Tuning

The low emittance tuning effort at CESR-TA has employed improved instrumentation for measuring the beam size and motion (including an upgraded BPM system and X-ray beam size monitor for measuring the vertical beam size), as well as new techniques for quantifying and compensating for lattice errors [45]. At 2.1 GeV, typical vertical emittances of $\lesssim$ 10 pm are routinely achieved.

1.2.3 Studies of EC Growth and Mitigation

Four main types of local electron cloud measurements have been employed at CESR-TA :

Table 1.2: CESR parameters and typical beam conditions for electron cloud mitigation studies

Parameter	Value(s)	Units
General Parameters		
Circumference	768	m
Revolution Period	2.56	μs
Harmonic number	1281	-
Number of bunches	9, 20, 30, 45	-
Bunch spacing	4 - 280	ns
Beam energy	2.1, 4, 5.3	GeV
2.1 GeV Parameters		
RMS Horizontal Emittance	2.6	nm
RMS Vertical Emittance	.02	nm
RMS Bunch Length	12.2	mm
Bunch current	0 - 5	mA[1]
Beam species	e^+, e^-	-
4 GeV Parameters		
RMS Horizontal Emittance	23	nm
RMS Vertical Emittance	.23	nm
RMS Bunch Length	9	mm
Bunch current	0 - 6	mA
Beam species	e^+	-
5.3 GeV Parameters		
RMS Horizontal Emittance	144	nm
RMS Vertical Emittance	1.3	nm
RMS Bunch Length	20.1	mm
Bunch current	0 - 10	mA
Beam species	e^+, e^-	-

- Retarding field analyzers (RFAs). These devices, which are the focus of the work presented here, provide a time integrated measurement of the electron cloud wall flux. From this we can infer the local cloud density, transverse distribution, and energy spectrum (see Section 1.3 for a more thorough introduction).

- Shielded pickups (SPUs). Essentially a BPM button shielded from direct beam signal, these detectors provide a cloud measurement which is resolved in time, but not energy or transverse position (Fig. 1.8). Thus they

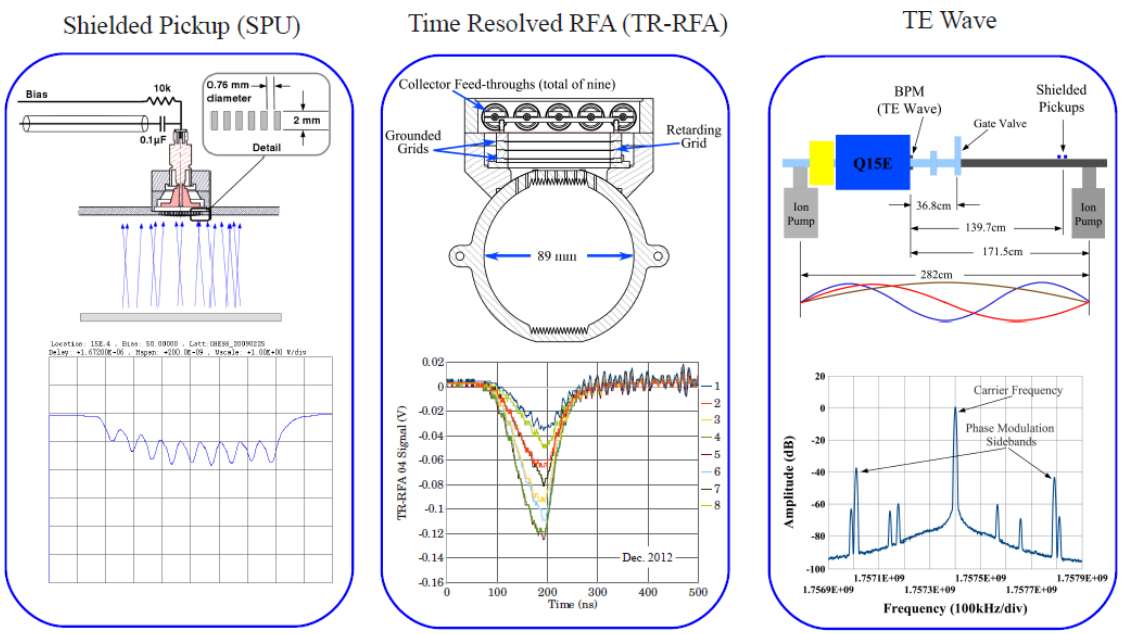

Figure 1.8: Other EC measurement techniques employed at CESR-TA .

are complimentary to the RFA measurements.

- Microwave transmission (TE-Wave, or TEW): By prorogating a microwave through a section of the vacuum chamber and measuring the phase shift caused by the presence of electron cloud, one can in principle directly obtain the local cloud density near the center of the vacuum chamber. However, practical considerations (e.g. variations in the vacuum chamber geometry) make interpreting these measurements challenging.

- Time resolved retarding field analyzers (TR-RFAs): Combining the basic geometry of a standard RFA with high bandwidth electronics, these devices can measure the electron cloud wall flux as a function of time, position, and energy. They have recently been installed in L3, and measurements have been done, but the analysis of the data is still in its infancy.

1.2.4 Studies of EC Induced Instabilities

Several global signatures of electron cloud have been observed at CESR-TA . The most prominent of these is a coherent tune shift along a train of bunches (which has opposite sign for electron and positron beams), caused by the linear focusing effect of the cloud. In effect, this provides an indirect measurement of the cloud density, averaged around the ring.

The nonlinear forces exerted by the cloud are more dangerous. At low cloud densities, they lead to emittance growth along the train, while high densities can lead to beam instabilities, in particular a head-tail instability. Both phenomena have been observed at CESR-TA . At very high densities, beam loss is unavoidable. We believe this is responsible for the current limits for positron beams at 2.1 and 4 GeV (Table 1.2).

1.3 Retarding Field Analyzers

RFA measurements have been a part of the CESR-TA program since it began in mid 2008. A more detailed description of the design and construction of the RFAs and experimental sections can be found in [1]; here we provide a brief overview.

A retarding field analyzer consists of three main components [43]: holes drilled in the beam pipe to allow electrons to enter the device; a "retarding grid," to which a voltage can be applied, rejecting electrons with less than a certain energy; and a positively biased collector, to capture any electrons which make it past the grid (Fig. 1.9). If space permits, additional (grounded) grids

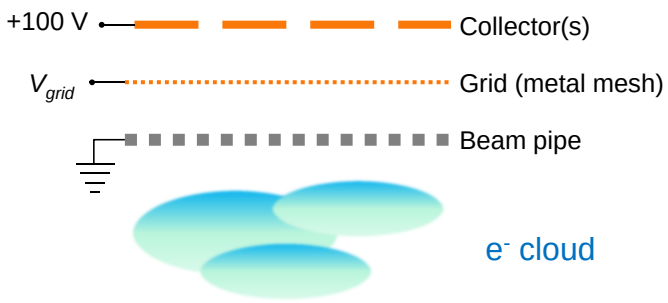

Figure 1.9: Idealized diagram of a retarding field analyzer.

can be added to allow for a more ideal retarding field. In addition, the collectors of most RFAs used in CESR-TA are segmented to allow characterization of the spatial structure of the cloud build-up. Thus a single RFA measurement provides information on the local cloud density, energy, and transverse distribution. Most of the data presented here are one of two types: "voltage scans," in which the retarding voltage is varied (typically from +100 to -250 V or -400 V) while beam conditions are held constant, or "current scans," in which the retarding grid is set to a positive voltage (typically +50 V), and data are passively collected while the beam current is increased. The collector was set to +100 V for all of our measurements.

The use of RFAs for electron cloud studies was pioneered at APS [43]; additional studies have been performed at the FNAL Main Injector [49], PEP-II [41], and KEKB [34]. However, the CESR-TA RFA program is unprecedented in terms of scale. We have used RFAs to probe the local behavior of the cloud at multiple locations in CESR, in different magnetic field environments, under many sets of beam conditions, in the presence of several different mitigation schemes, and over long periods of time.

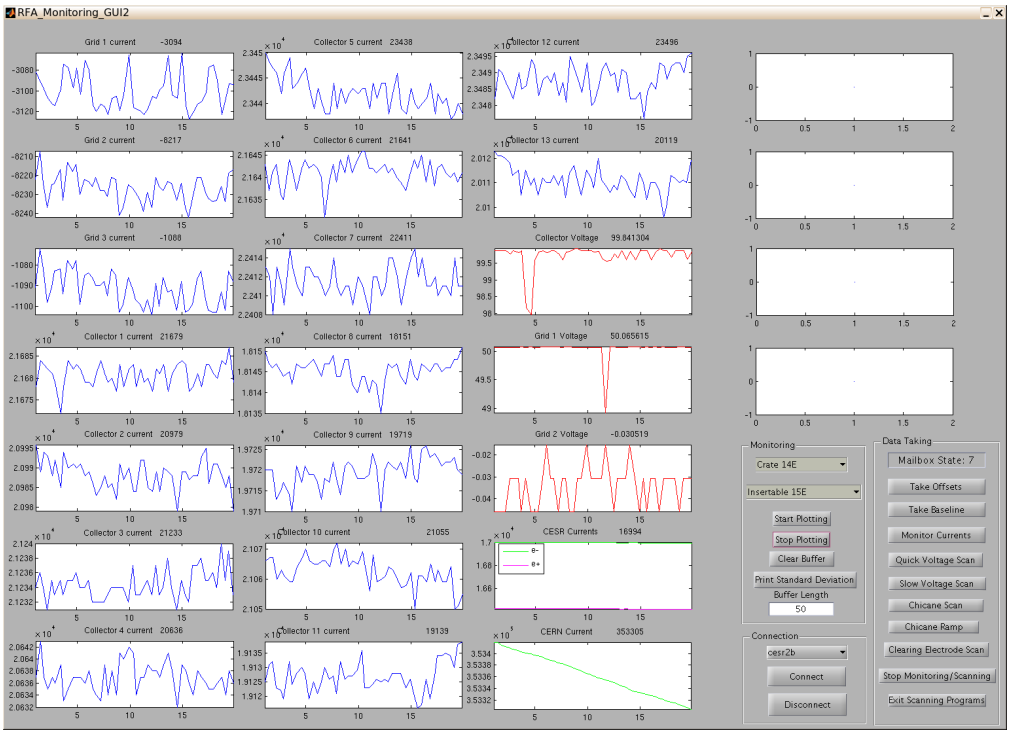

Figure 1.10: MATLAB GUI used for RFA machine studies, showing real time readout of the grid and collector currents and voltages, as well as the beam current.

1.3.1 Data Acquisition System

A modular high voltage power supply and precision current monitoring system has been designed to support simultaneous RFA measurements at multiple locations around CESR [40]. Data acquisition is controlled through a MATLAB based graphical user interface (Fig. 1.10), which also allows for real time monitoring and control of any RFA. Data are collected simultaneously by all the RFAs, and the GUI allows for commands to be issued to all the devices at once.

1.4 Cloud Simulations

As the behavior of the electron cloud can be very complicated and depends on many parameters, it is best understood on a quantitative level through the use of computer simulations. The majority of the results presented here were obtained with the particle tracking code POSINST [29, 28, 26]. In this code, the electrons are dynamical (and represented by macroparticles), while the beam is not (and is instead represented by a prescribed function of time and space). As such, it is useful for modeling buildup of the cloud, but not the effect of the cloud on the beam. Other codes, with a dynamic beam but static cloud, or with both beam and cloud modeled dynamically, can be used for this purpose [**?**].

In POSINST, a simulated photoelectron is generated on the chamber surface and tracked (F=ma) under the action of the beam. Secondary electrons can be generated via a probabilistic process. Space charge and image charge are also included. Electron motion is fully 3D, but the space charge forces are only calculated in two dimensions. Effectively this assumes periodic boundary conditions. POSINST has been used to model cloud buildup at many labs, including LBL, Argonne, SLAC, LANL, and CESR.

1.4.1 Simulation Parameters

There are many parameters related to primary and secondary electron emission that are relevant to this analysis. The secondary electron yield model in POSINST contains three components- "true" secondaries, which are emitted at low (<~20 eV) energy regardless of the incident particle energy; "elastic" sec-

ondaries, which are emitted at the same energy as the incident particle; and "rediffused" secondaries, which are emitted with a uniform energy spectrum, ranging between 0 and the incident particle energy. The peak true secondary yield (characterized by the parameter `dtspk` in POSINST) occurs for primary electrons with an incident energy (POSINST parameter `E0epk`) around 300 eV. The peak elastic yield (POSINST parameter `P1epk`) occurs at low energy (we assume 0 eV), while the rediffused yield reaches a steady state value for high energy primaries (POSINST parameter `P1rinf`). Fig. 1.11 shows a typical SEY curve, and indicates how each of these parameters contributes to the total secondary yield (POSINST parameter `dtotpk`).

Under typical beam conditions, the cloud is seeded by photoelectrons, but secondary electrons (especially "true" secondaries) tend to dominate towards the end of the train. This is especially true for high current beams, which will drive the average electron energy up into the hundreds of eV range, where the secondary electron yield is highest. After the train passes, the energy of the cloud quickly decreases, and elastic secondaries take over. Roughly speaking, true secondaries determine the the peak cloud density during the train, while the elastic yield determines the decay time. The rediffused yield contributes to both the buildup and decay. Fig. 1.12 plots the average cloud density as a function of time for typical CESR-TA beam conditions, and shows where each type of electron dominates.

POSINST also makes use of several parameters that describe the properties of emitted secondary electrons. The parameters that define the true-secondary emission energy distribution were chosen to give a peak emission energy of 1.5 eV, based on RFA measurements done in a dipole [6]. Secondaries are emitted

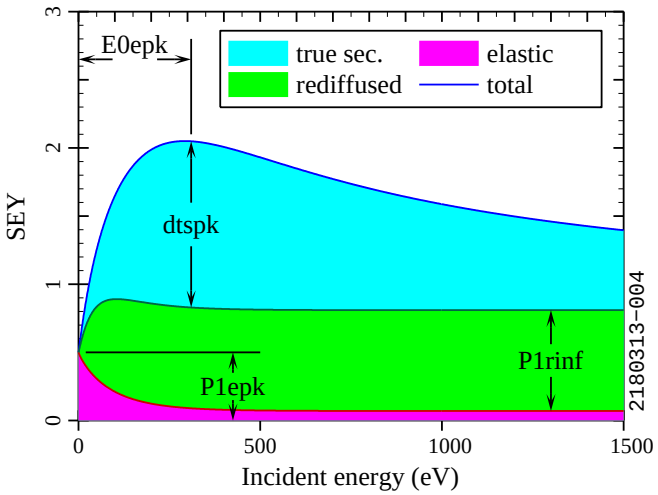

Figure 1.11: The POSINST model for secondary electron yield as a function of energy, with important parameters indicated.

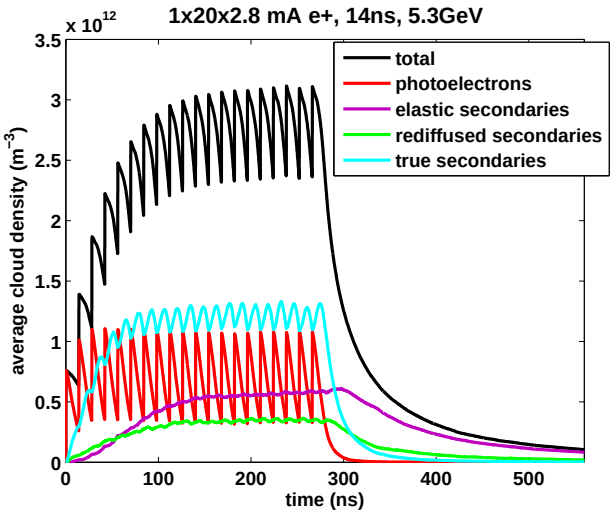

Figure 1.12: Average cloud density vs time, broken down by electron type.

with angular distribution $\partial dN/\partial\theta \propto \sin(\theta)\cos(\theta)$, where θ is the angle relative to the normal to the surface at the emission point.

The model for photoelectron emission in POSINST is simpler than the secondary model, but still involves several important parameters. The most significant of these is the quantum efficiency (`queffp`). In addition, we have found

that in order to have any RFA signal for a high current electron beam simulation, a high energy component in the photoelectron energy spectrum is required. This is accomplished by using a Lorentzian photoelectron energy distribution (which has been observed in some measurements [17]), with a low peak energy (5 eV), and a width that scales with the average photon energy incident at the RFA position. For example, for an electron beam at Q15E, the width is 12 eV for a 2.1 GeV beam, and 150 eV for a 5.3 GeV beam. The RFA data does not constrain the exact shape of the distribution. Measurements with a shielded pickup detector [19] provide a method to probe these parameters in more detail.

For most of the simulations shown here, the photon flux and azimuthal distribution at the RFA are determined by a 3 dimensional simulation of photon production and reflection [23], which includes diffuse scattering and a realistic model of the CESR vacuum chamber geometry.

CHAPTER 2

FIELD FREE RFA STUDIES

We have taken more RFA data in a field free environment than in any kind of magnetic field. The relatively simple dynamics of the cloud in a drift has enabled detailed quantitative analysis of this data.

2.1 Drift Instrumentation

Of the seven EC experimental sections in CESR (Section 1.2.1), five have been instrumented with drift RFAs: Q14E/W, Q15E/W, and L3.

2.1.1 Q14W and Q14E Test Sections

Upon the removal of the CESR-c superconducting wigglers, two electron cloud experimental sections were created on both east and west arcs of CESR. Measurements in the Q14W test section confirmed that an "Insertable I" style RFA gives results comparable to the well understood "APS" style [40] (see below for descriptions of the different RFA styles). At Q14E, the copper beam pipe was coated with TiN thin film for half of its length (while the other half remained bare copper). Insertable RFAs were installed at each end of this test chamber to compare electron cloud intensity in the two sections.

Table 2.1: Summary of Q15W and Q15E Experimental Vacuum Chambers (VCs)

VC	Surface	Run	RFA Style	Test Period	Location	Note
1	Al	1	Thin	Jul 2009-Nov 2009	E	Reference surface
		2	Thin	Apr 2010-Aug 2010	W	
		3	Insertable II	Aug 2012-present	E	
2	TiN	1	Thin	Dec 2009-Apr 2010	E	Coated by DC sputtering at Cornell
		2	Thin	Aug 2010-Jan 2011	W	
		3	Insertable II	Feb 2011-Jul 2011	W	
		4	Insertable II	Aug 2012-present	W	
3	aC	1	Thin	Jul 2009-Apr 2010	W	Coated by DC sputtering at CERN
4	aC	1	Thin	Apr 2010-Jan 2011	E	Coated by DC sputtering at CERN
		2	Insertable II	Jul 2011-Jul 2012	W	
5	DLC	1	Insertable II	Feb 2011-Jul 2012	E	Coated by pulsed DC chemical vapor deposition, supplied by KEK

2.1.2 Q15W and Q15E Mitigation Comparison Chambers

To allow for frequent exchange of the test chambers while minimizing the impact on the accelerator operations, two very short experimental regions were created in the Q15W and Q15E locations in the arcs. Over the course of the CESR-TA program, four chamber surfaces were tested in these locations: bare aluminum (as it was originally extruded), aC coatings (coated by CERN/CLIC), TiN coating (by Cornell) and DLC coating (by KEK). Table 2.1 gives detailed information on these chambers, and Fig. 2.1 shows a typical installation at Q15W.

There is some evidence the aC coated chambers may have been contaminated by silicone tape present during the bakeout of the chamber [1], raising the effective SEY. However, as described in Section 2.3.2, these chambers still showed good performance in situ.

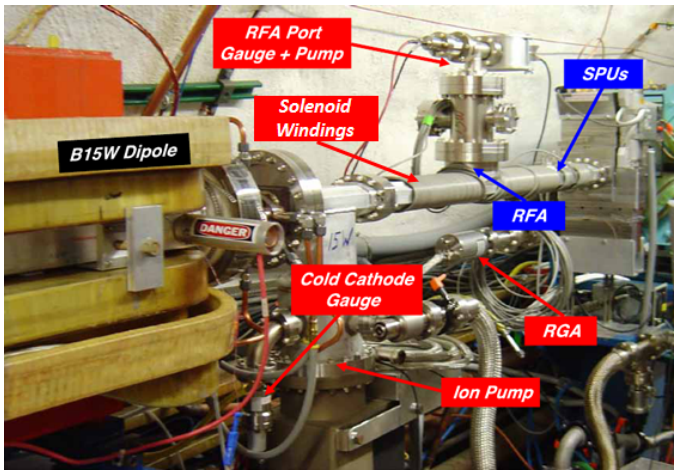

Figure 2.1: A Q15 experimental chamber installed at Q15W in CESR. In addition to the RFA, the chamber contains 4 shielded pickups (SPUs) [19].

2.1.3 L3 Test Section

A Ti-Zr-V non-evaporable getter (NEG) thin film [47] has been shown to have a low SEY, after its activation at elevated temperatures under vacuum. The activated NEG coating also has the benefit of providing vacuum pumping. A NEG-coated test chamber was built and tested in the drift section of the L3 experimental region in CESR. To prevent rapid saturation of the activated coating from residual gases in the surrounding beam pipes, the test chamber was sandwiched between two 1-m long NEG coated beam pipes. The chamber was equipped with three APS-style RFAs at three different azimuthal angles (see Fig. 2.2). All three chambers were made of stainless steel (Type 304L).

2.1.4 Drift RFA Styles

Several different styles of RFA have been deployed throughout drift sections in CESR. Table 2.2 summarizes the key parameters of each style, and Table 2.3

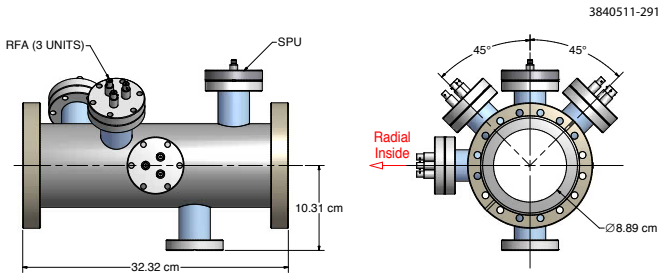

Figure 2.2: Electron cloud diagnostic chamber with NEG thin film coating.

Table 2.2: Drift RFA styles deployed in CESR. Each RFA has one retarding grid. For RFAs with multiple grids, the additional grids are grounded.

Type	Grids	Collectors	Grid Type
Thin Test	1	1	Etched
APS	2	1	Mesh
Insertable I	2	5	Etched
Insertable II	3	11	HT Mesh
Thin	1	9	HT Mesh

describes the different types of grids used. A more detailed description of each RFA style follows:

"Thin test" style The "thin test" style RFA was designed to test whether RFAs could perform in vacuum chambers where detector space is severely limited due to magnet apertures, and to serve as a stepping stone to the more complex models described below. It consists of a single grid and single collector, spaced by 1 mm. A self supporting stainless steel grid with an etched bi-conical hole structure (.18 mm diameter holes with a .25 mm pitch) was chosen for the grid.

Table 2.3: Grid types used in CESR RFAs. Note that "transparency" refers to the optical transparency.

Type	Transparency	Material	Thickness
Etched	40%	Gold coated SST	150 μm
Mesh	46%	SST	76 μm
HT Mesh	90%	Copper	13 μm

In addition, the grid layer was vacuum-coated with a thin gold layer (several hundred nm) to reduce its secondary electron yield. The electron collector pad was laid out on copper-clad Kapton sheet using standard printed circuit board fabrication techniques.

APS style This design is based on a well understood style of RFA [43], and was used as a cross check to verify reasonable operation of the "Insertable I" style, described below. It consists of a single collector, and two stainless steel meshes for grids. APS style RFAs were also deployed in the L3 NEG test chamber (Section 2.1.3).

Insertable I Deployed in the Q14E and Q14W experimental regions of CESR, these RFAs were designed to be "inserted" on top of a standard vacuum chamber. They have two stainless steel grids, spaced by 3 mm. Transverse resolution is provided by five (Kapton) collectors. Holes are drilled in the beam pipe in five segments; each segment has 25 holes, with diameter 1.5 mm and depth 5.1 mm. The dimensions of the RFA holes are chosen to ensure no significant leakage of the beam's RF fields into the detector signals, while maximizing the transparency of the RFA to the vacuum chamber. Fig. 2.3 gives a detailed picture of this RFA.

Thin style Designed for use inside a CESR dipole, where aperture space is limited, the thin style detector was also used in the Q15E and Q15W drift sections. The RFA housing is machined from a separated block of explosion-bonded aluminum-to-stainless steel material, and is welded to the cutout on top of the beam pipe. The lower face of the RFA housing matches the curva-

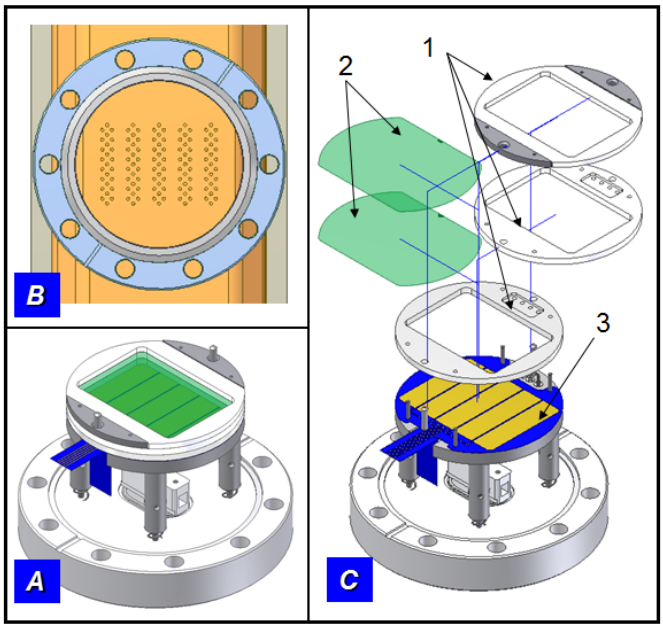

Figure 2.3: Engineering diagram of an "Insertable I" style RFA. (A) Assembled RFA structure. (B) Vacuum chamber hole pattern. (C) Exploded view of the RFA, showing (1) Macor spacers, (2) stainless steel grids, and (3) flexible circuit collectors.

ture of the beam pipe aperture, while the upper face is divided into three flat sections. Each section has one retarding grid, which is made of high efficiency electro-formed copper mesh, held in place by a stainless steel frame. There are three collectors in each section, for a total of nine. The total distance from the outside of the vacuum chamber to the collectors is 2.5 mm. The beam pipe holes are 0.75 mm in diameter and ~2.5 mm in thickness, maintaining the same ratio of diameter to thickness used for the "Insertable I" style. There are 44 holes per collector. A diagram of a Q15 test chamber, which includes a thin RFA (as well as 4 shielded pickup detectors [19]) is shown in Fig. 2.4.

Insertable II The second generation insertable RFA has three grids, consisting of high-transparency copper meshes, spaced by 5.7 mm. The retarding voltage is applied to the middle grid. Insertable II RFAs were installed in the 5^{th} Q15

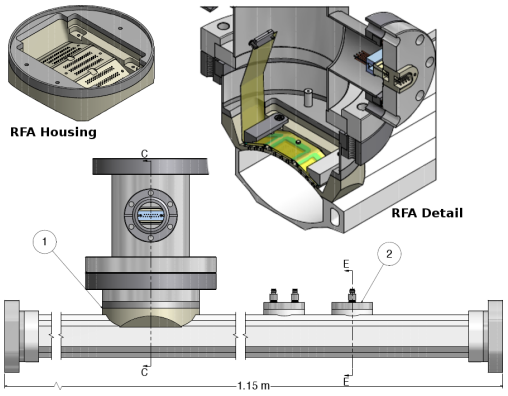

Figure 2.4: Q15 EC Test Chamber, equipped with an RFA (1) and 4 shielded pickups (2)

test chambers, replacing the "thin" style detectors. The additional grids and increased spacing between them results in a more ideal retarding field, and reduces some of the troublesome complications observed in the "thin" RFA (see Section 2.4). It also allows for higher retarding voltage, up to -400 V. To provide cross calibration between the two RFA designs, a TiN-coated test chamber in Q15W was instrumented with both styles (refer to Table 2.1).

2.2 Measurements

Many of our earliest detailed measurements were done with "Insertable I" style RFAs (Table 2.2). Fig 2.5 shows an example of a voltage scan done with one of these detectors, in typical CESR-TA beam conditions. The RFA response is plotted as a function of collector number and retarding voltage. Roughly speaking, this is a description of the transverse and energy distribution of the cloud. Collector 1 is closest to the outside of the chamber (where direct synchrotron radiation hits); the central collector (3 in this case) is aligned with the beam. The sign convention for retarding voltage is chosen so that so a positive value on this axis

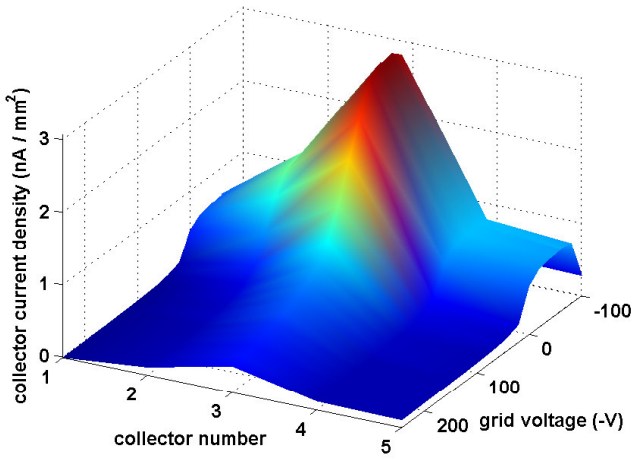

Figure 2.5: RFA voltage scan with an "Insertable I" style drift RFA in a Cu chamber, 1x45x1.25 mA e^+, 14 ns, 5.3 GeV

corresponds to a negative physical voltage on the grid (and thus a rejection of lower energy electrons). In this example, the signal is fairly broad across all five collectors, indicating that the cloud density is not strongly peaked around the beam. It also falls off quickly with retarding voltage, indicating that the majority of cloud particles have low energy. The RFA signal is expressed in terms of current density in nA/mm^2, normalized to the transparency of the RFA beam pipe and grids. In principle, this gives the time averaged electron current density incident on the beam pipe wall. The beam conditions are given as "1x45x1.25 mA e^+, 14 ns, 5.3 GeV." This notation, which will be used throughout this section, indicates one train of 45 bunches, with 1.25 mA/bunch (for CESR, a beam of 1 mA has 1.6×10^{10} particles), with positrons, 14 ns spacing, and at beam energy 5.3 GeV.

As described in Section 2.1.4, both "thin" and "Insertable II" style RFAs have been installed at Q15E and Q15W. Example measurements done with both of these RFA styles, in a TiN-coated chamber, can be found in Fig. 2.6. These mea-

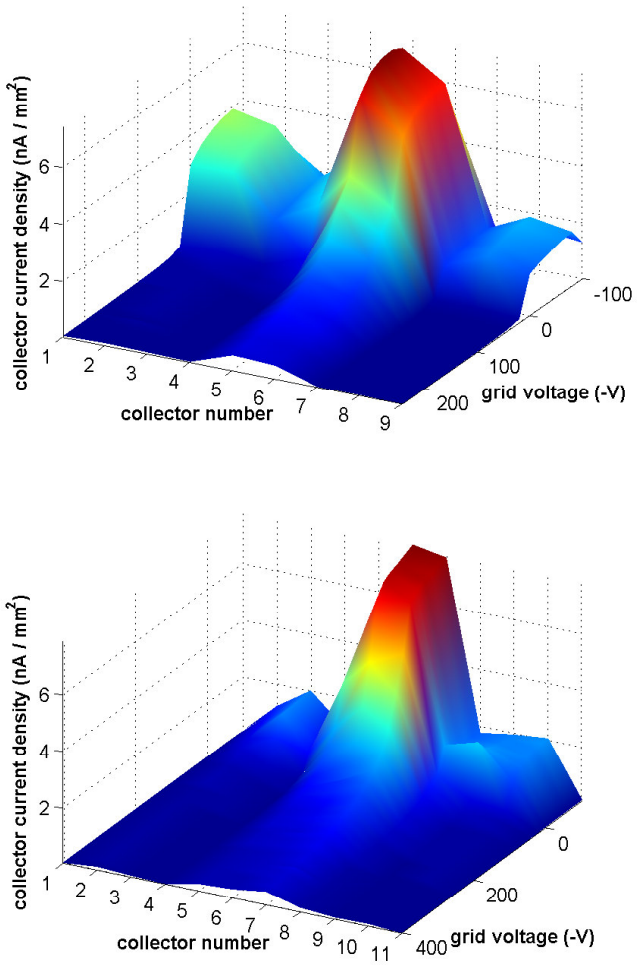

Figure 2.6: Example voltage scans with thin (top) and Insertable II (bottom) style drift RFAs in the same location (Q15W). Both are TiN-coated, beam conditions are 1x45x1.25 mA, 5.3 GeV, 14 ns.

surements can be contrasted with one done at higher bunch current (Fig. 2.7). Here we observe the signal extends to much higher energy, and is more strongly peaked in the central collector.

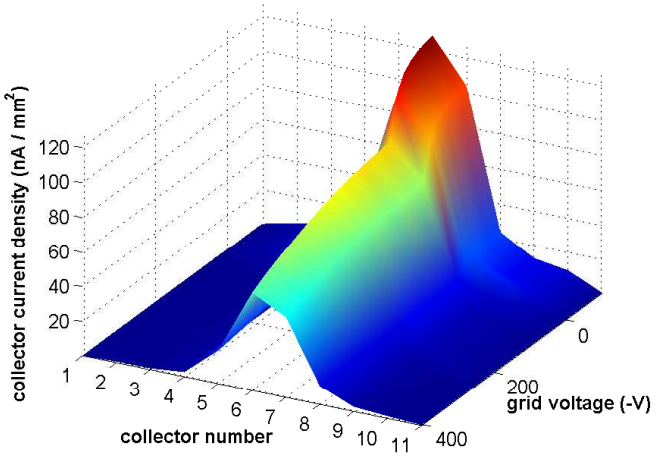

Figure 2.7: Voltage scan at high bunch current, 1x20x10 mA e^+, 5.3 GeV, 14 ns, Insertable II RFA, in a TiN-coated chamber at Q15W.

2.2.1 Bunch Spacing Comparison

Although our RFA measurements are not time resolved, we can probe the time scale of cloud development by examining the RFA response as a function of bunch spacing, which can be varied in 4 ns increments. Fig. 2.8 shows such a comparison for the Q15W aC coated RFA. We observe that the signal at high retarding voltage (i.e. the number of high energy cloud particles) is highest for the 4 ns data, and falls off quickly and monotonically with increasing bunch spacing. With short bunch spacing, a typical electron will receive multiple beam kicks before colliding with the vacuum chamber, gaining 100s of eV in the process. However, the total signal (including high and low energy electrons) is actually highest for 16 ns. This is consistent with a multipacting resonance [30, 31], in which the kick from the beam gives secondary electrons near the vacuum chamber wall just enough energy to reach the opposite wall in time for the next bunch. These electrons generate more secondaries, which are again given energy by the beam. This process continues, resulting in a resonant buildup of the

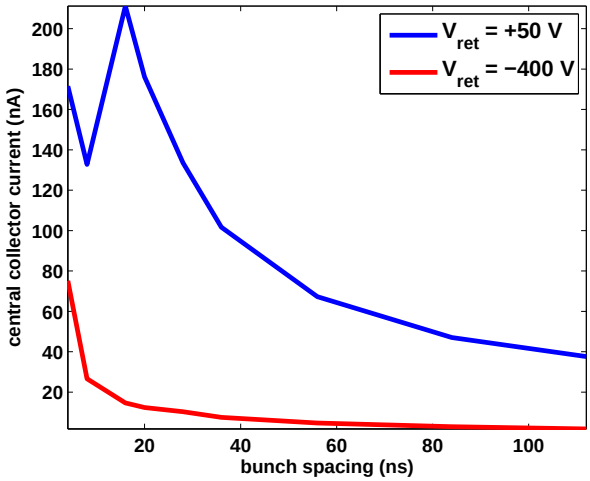

Figure 2.8: Central collector signal as a function of bunch spacing, 1x20x3.6mA e^+, 5.3GeV, in an aC coated chamber at Q15W.

cloud. The resonant condition is given by Eq. 2.1. Here t_b is the bunch spacing, b is the chamber half-height, r_e is the classical electron radius, and N_b is the bunch population. For the beam conditions in Fig. 2.8, this comes out to 13 ns, consistent with the 16 ns peak observed.

$$t_b = \frac{b^2}{c r_e N_b} \tag{2.1}$$

2.3 Mitigation comparisons

An important component of the CESR-TA program is the direct comparison of different electron cloud mitigating coatings, tested at Q14E, Q15E/W, and L3. In this section we compare "current scans" (RFA signal as a function of beam current), for different mitigations in each of the instrumented sections of CESR. The transverse distribution observed at a given beam current was substantially

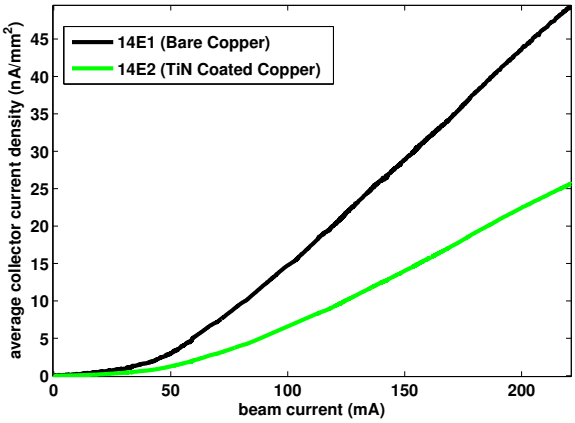

Figure 2.9: Comparison of insertable drift RFAs, 1x20 e^+, 5.3GeV, 14ns

the same for different chambers, so the plots shown below average over the RFA collectors. All of the measurements were done with the retarding grid biased to +50 V in order to measure cloud electrons of all energies.

2.3.1 Comparison of adjacent chambers at Q14E

Fig. 2.9 compares a current scan measurement done simultaneously with two adjacent RFAs in the Q14E section (Section 2.1.1), one in a bare copper chamber, and one in a TiN-coated copper chamber. Here we compare the average collector current density in the two detectors, as a function of beam current, and find that it is lower in the coated chamber by a factor of two. The photon flux is actually about 50% higher in the TiN coated chamber, so a more direct comparison would show an even larger improvement.

2.3.2 Comparisons of chambers with different coatings installed at the same locations at Q15E/W

The majority of our mitigation studies were done with RFAs in the Q15W and Q15E experimental sections (Section 2.1.2). The photon flux from a positron beam at Q15W is about twice that of Q15E, and vice versa for an electron beam. Measurements have been taken at both locations with TiN and aC coatings, as well as with an uncoated aluminum chamber (see Table 2.1). In addition, a chamber with DLC coating has been installed at Q15E. By comparing measurements taken at the same location in CESR, we ensure the comparisons can be made under identical beam conditions, including photon flux. Figs. 2.10 through 2.12 compare the RFA signal with each of these coatings for typical sets of CESR-TA beam conditions. The beam energy is 5.3 GeV in all cases; the comparisons are for one train of 20 bunches spaced by 14 ns (positrons in Fig. 2.10, electrons in Fig. 2.11) and 9 bunches of positrons spaced by 280 ns (Fig. 2.12). We have generally found that data taken with 20 bunches of positrons at high current shows the biggest difference between the different chambers. It is under these conditions that we expect to be most sensitive to the secondary electron yield.

There was some concern that these measurements could be affected by the adjacent aluminum chambers (which should have a higher cloud density). To address this issue, 100 Gauss dipole magnets were installed on either side of the coated chambers, to prevent the spilling of electrons from the aluminum chambers into the coated chambers. We found that the use of these magnets had little effect on the RFA measurements.

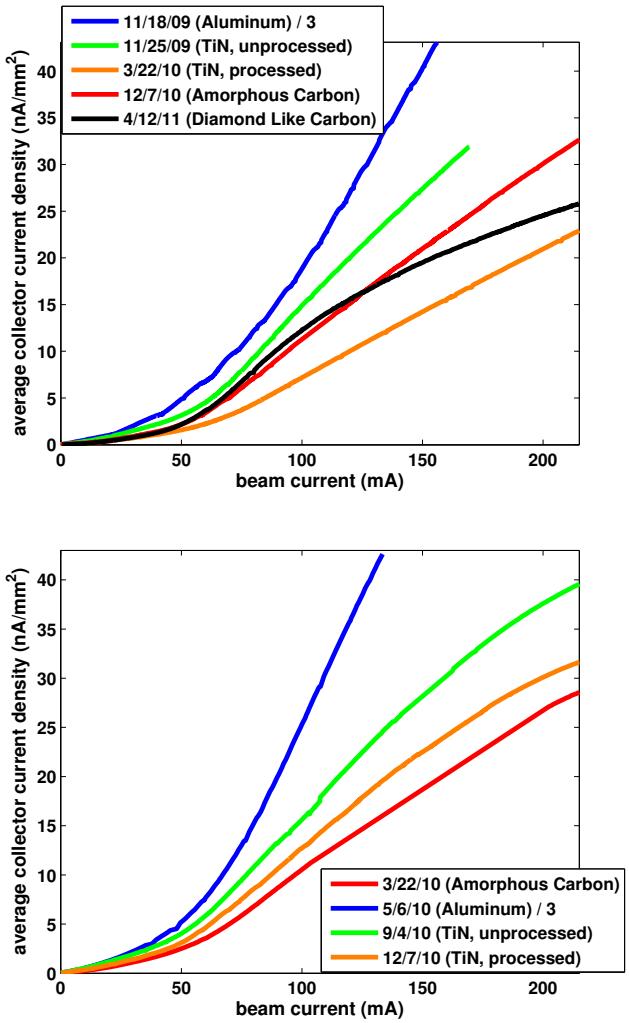

Figure 2.10: Comparison of different beam pipe coatings, Q15E (top), and Q15W (bottom) drift RFAs. Plots show average collector signal vs beam current for 20 bunches of positrons with 14 ns spacing, at beam energy 5.3 GeV. Note that the aluminum chamber signals are divided by 3.

All coated chambers show a sizeable reduction in signal when compared to uncoated aluminum. We have found that exposure to electron cloud bombardment significantly improved the performance of the TiN-coated chamber. This effect, known as "scrubbing" or "processing," is well known [18], and has been observed in direct measurements of the SEY of a TiN coated chamber [38]. In these plots, "unprocessed" TiN refers to data taken after 2.5 A-hrs of beam processing, while the "processed" chamber received 940 A-hrs. The aC chamber's

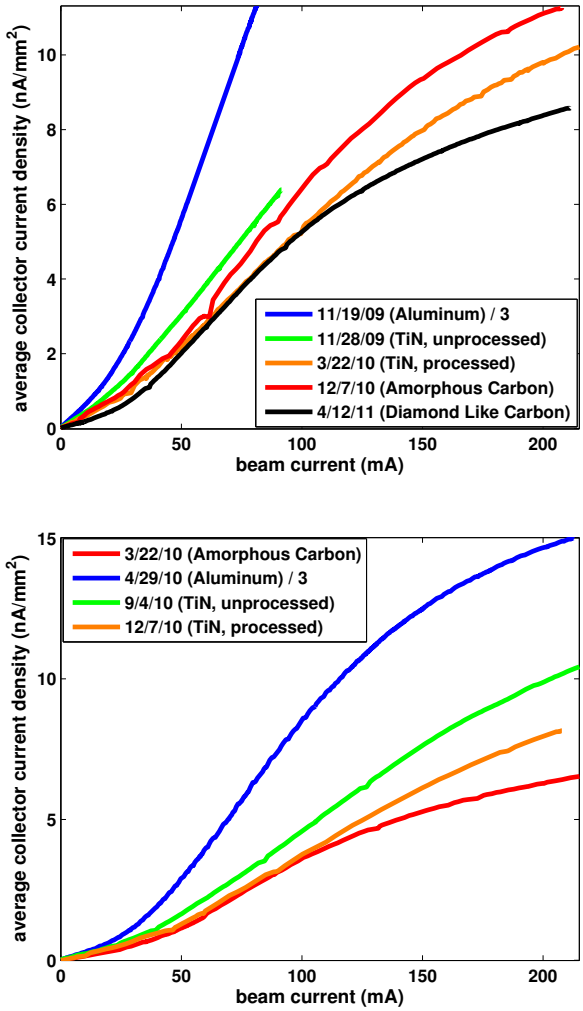

Figure 2.11: Comparison of different beam pipe coatings, Q15E (top), and Q15W (bottom) drift RFAs. Plots show average collector signal vs beam current for 20 bunches of electrons with 14 ns spacing, at beam energy 5.3 GeV. Note that the aluminum chamber signals are divided by 3.

signal was initially low, and we did not observe a significant change in signal with EC bombardment. After extensive processing of the TiN chamber, TiN and aC showed similar mitigation performance.

At first glance, it appears DLC may perform better than other coatings at very high beam current. However, it should be noted that bench measurements of the Secondary Electron Yield (SEY) of DLC have found that the material can

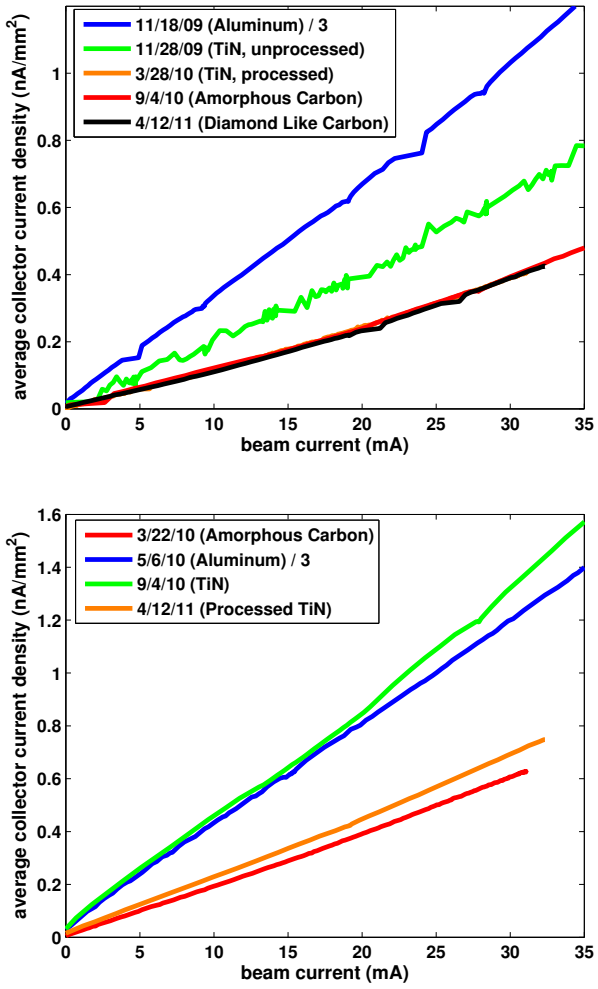

Figure 2.12: Comparison of different beam pipe coatings, Q15E (top), and Q15W (bottom) drift RFAs. Plots show average collector signal vs beam current for 9 equally spaced (280 ns) bunches of positrons, at beam energy 5.3 GeV. Note that the aluminum chamber signals are divided by 3. In the top plot, the curve for processed TiN is difficult to see, because it lies almost directly under the curve for aC.

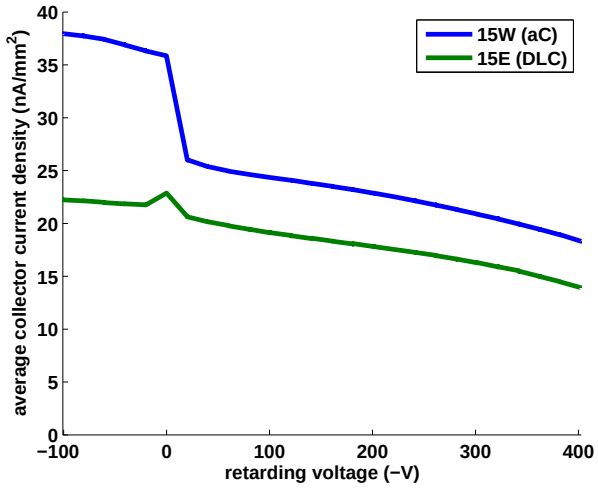

Figure 2.13: Comparison of amorphous and diamond-like carbon at high beam current, 1x20x10mA e^+, 5.3 GeV, 14 ns.

retain charge if bombarded with a sufficiently high electron flux, thus modifying the apparent SEY performance [36]. This effect may also be influencing the in situ measurements presented here. Evidence for this hypothesis can be found in Fig. 2.13, which compares a voltage scan done at high beam current in a DLC and aC chamber. The aC shows an enhancement at positive retarding voltage, which is seen in almost all of our drift RFA data (see Section 2.4). The DLC chamber instead shows a nonphysical spike at 0 V, but no enhancement at positive voltage. This could be the result of charge around the beam pipe holes influencing the transmission of low energy electrons.

2.3.3 Long Term Behavior

Another important issue addressed by the CESR RFA measurements is the long term reliability of various chambers and coatings. Figures 2.10 - 2.12 show that significant processing was observed in TiN-coated chambers in both Q15E and

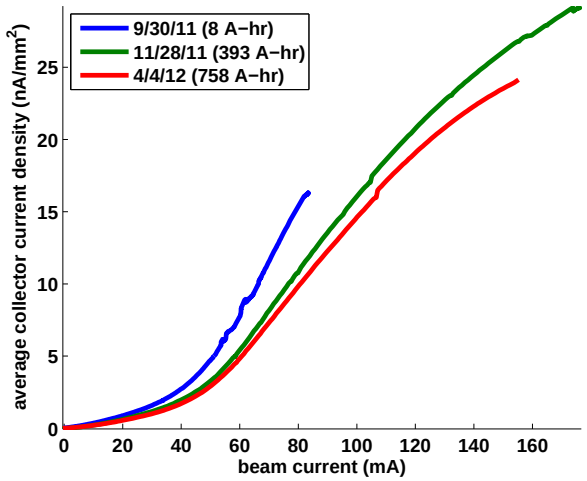

Figure 2.14: Processing history in the newer Q15W aC coated chamber, 1x20 e^+, 5.3GeV, 14ns. Integrated beam doses are given for each measurement.

Q15W; this was not observed in the aC chambers. However, more recent measurements (Fig. 2.14) have shown some processing in an aC coated chamber. While reduction of the secondary yield has not been observed in aC, this decrease in signal could be explained by a reduction in the quantum efficiency [20]. This effect was not observed in the other aC data, most likely because RFA measurements were not made soon enough after installation.

The signal measured in the DLC chamber varied significantly over time (Fig. 2.15). Apart from some initial processing, the measurements in this chamber do not appear to show any obvious trend. It is possible that the properties of the DLC depend on the recent beam history before the measurement.

2.3.4 Activation and processing of NEG coated chambers in L3

The performance of the L3 NEG coated chamber (Section 2.1.3) has also been monitored using RFAs. Fig. 2.16 compares the current measured by one of

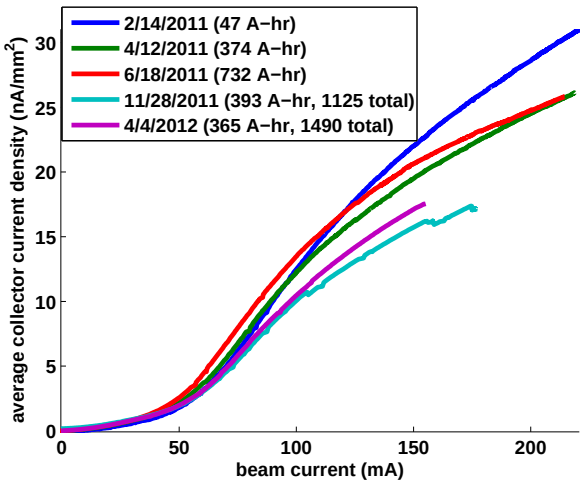

Figure 2.15: Performance of Q15E DLC chamber over time, 1x20 e^+, 5.3GeV, 14ns. Integrated beam doses are given for each measurement. Where two doses are shown, the first is counted from the last CESR down, and the second from the installation of the chamber.

these RFAs on several different dates, corresponding to different states of activation and processing of the NEG coating. It was observed that both activation and initial processing reduced the signal measured by this RFA. After a CESR down (during which the NEG was activated again), the signal rose somewhat, but it processed back down to its minimum value after a few months of beam time. The other two detectors showed a similar trend. These signals remained consistent in subsequent runs.

2.4 Drift RFA Modeling

To understand the measurements described above on a more fundamental level, we need a way of translating an RFA measurement into physical quantities relating to the development of the electron cloud. To bridge this gap, accurate models of both the cloud development and the RFA itself are required. The

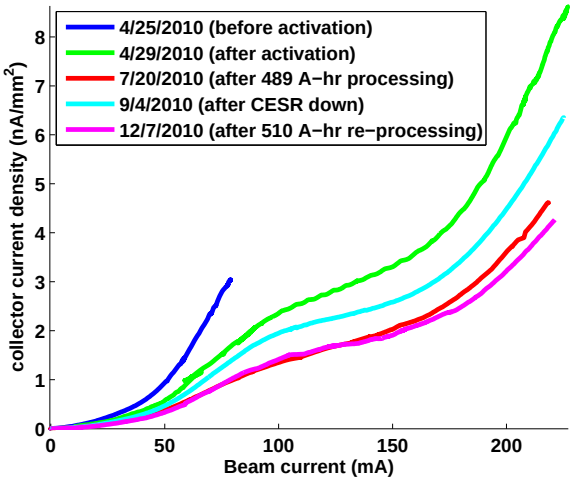

Figure 2.16: NEG RFA comparison, 1x20 e^+, 5.3GeV, 14ns

former task is handled by the well validated cloud simulation code POSINST (Section 1.4), which tracks the motion of cloud particles during and after the passage of a bunch train. We have modified POSINST to include a model of the RFA, which automatically generates an output file containing the simulated RFA signals.

This integrated RFA model is implemented as a special function that is called when a macroelectron in the simulation collides with the vacuum chamber wall, immediately before the code section that simulates secondary emission. First, this function checks if the macroelectron is in the region covered by the RFA. If so, a certain fraction of the particle's charge, which depends on the incident angle and energy (as well as the overall beam pipe transparency), is added to the collector signal. The RFA acceptance as a function of angle and energy is calculated by a separate particle tracking code, described below. The charge is binned by energy and transverse position, reproducing the energy and position resolution of the RFA. The macroelectron then has its charge reduced by the amount that went into the detector, and the simulation continues as normal.

This process is shown diagrammatically in Fig. 2.17.

In order for this method to work, we need to know the RFA response to a particle with a given incident energy and angle. To answer this question, we developed a specialized code, which tracks electrons through a model of the RFA. The model includes a detailed replica of the beam pipe, grid(s), and collector, as well as a realistic map of the electric fields inside the RFA, generated by the electrostatic calculation tool Opera 3D (Fig. 2.18). The tracking code also allows for the production of secondary electrons on both the beam pipe and grid(s). The secondary emission model is a simplified version of the one used in POSINST, and includes both elastic and "true" secondaries (see Section 2.5.1). The output of the simulation is a table which maps the incident particle energy and angle to both a "direct" and (low energy) "secondary" collector signal. POSINST can then consult this table to determine the RFA response to a given macroelectron-wall collision.

The production of secondary electrons in the beam pipe holes and on the retarding grid is an especially important effect, and results in an enhanced low energy signal in most of our drift RFA measurements. Fig. 2.19 shows the simulated secondary signal in a thin style RFA, as a function of incident angle, for different incident electron energies. The effect is particularly strong for electrons with high energy and moderate angle.

2.4.1 Bench Measurement

To aid in the development of our model, we constructed a bench experiment to study the response of a test RFA under controlled conditions. The system

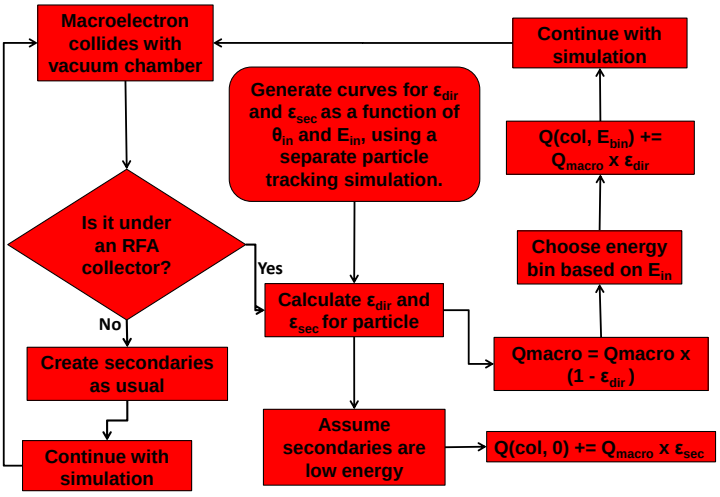

Figure 2.17: Conceptual flowchart of the RFA model in POSINST. The charge deposited in the collector is binned by energy and collector number ($Q(col, E_{bin})$). The magnitude of this quantity depends on the macroelectron charge (Q_{macro}) and the efficiency of the RFA (ε_{dir}), which in turn depends on the incident particle energy (E_{in}) and angle (θ_{in}). In addition, the macroelectron can generate low energy "secondary" charge ($Q(col, 0)$), depending on the secondary efficiency (ε_{sec}). Charge that enters the RFA is removed from the macroelectron.

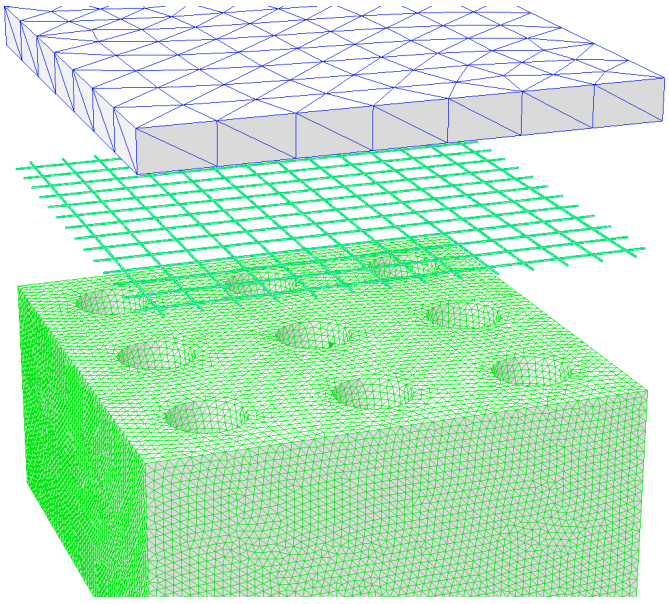

Figure 2.18: Opera 3D model of a typical drift RFA, showing (from top to bottom) the collector, thin retarding grid, and faceplate/vacuum chamber.

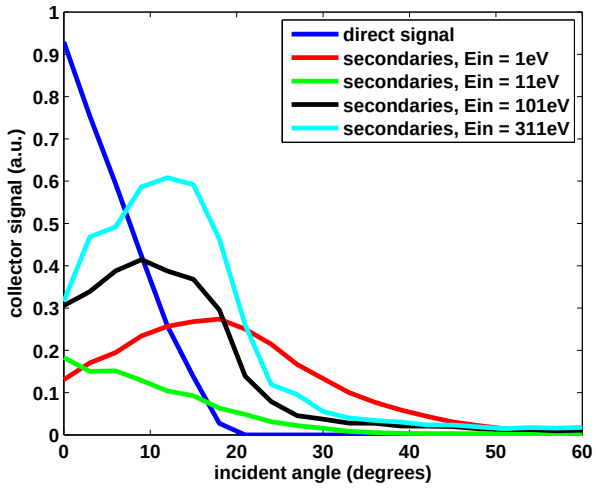

Figure 2.19: Simulated collector current caused by a uniform beam of electrons incident on the thin RFA model. The direct signal is determined only by the angular acceptance of the beam pipe holes. The "secondary" signal is caused by the production of (low energy) secondary electrons in the beam pipe holes and retarding grid, and depends on the energy of the incident electrons.

consists of an electron gun, which can produce a monoenergetic and roughly uniform beam of electrons, aimed at a test RFA. The electron gun and RFA are installed in a vacuum chamber with mu metal for shielding of ambient magnetic fields. The RFA includes a faceplate with holes drilled in it to mimic the vacuum chamber, a high efficiency (nominally 92%) retarding grid, and a collector. We are able to independently control the voltage and read the current on the collector, grid, and faceplate, as well as a top ring surrounding the faceplate. To do a measurement with this system, we set the electron gun to a specific energy, and adjust the deflection and focusing of the gun until the beam just covers the faceplate (i.e. until no current is observed on the top ring). We can then study the response of the RFA as a function of gun energy. Fig. 2.20 shows a series of retarding voltage scans done with our bench setup at different electron gun energies, and compares them to predictions from the particle tracking model. A few things are worth noting about these measurements:

- The collector signal is mostly flat for a retarding voltage between 0 and the gun energy, as expected for a monoenergetic beam.
- When the grid voltage is positive, there is a strong enhancement of the signal, caused by the production of low energy secondary electrons in the faceplate holes (described above).
- With +100 V on the grid (on the left side of the plots), the signal drops back down somewhat. This is because secondaries produced on the collector (which is also set to +100 V) are now able to escape.
- If the RFAs were ideal, the collector signal would drop to zero when the retarding voltage exceeds the gun energy. In the 100 eV and 200 eV scans, the signal does not immediately vanish, but drops off steadily, reaching zero current at −120 V and −230 V respectively. This effect is caused by focusing of the electrons by the non-ideal field of the grid, which allows electrons with energy slightly lower than the retarding voltage to slip by. This effect has also been observed in studies of RFA performance done at FNAL [49].

The simulation matches all important features of the data, including the enhancement at positive voltage and the non-ideal energy cutoff. The agreement is nearly perfect for 100eV, and 200eV, but the simulation slightly underestimates the collector signal at positive voltage for 500eV and 1keV. This aspect of the data is not understood, but could be due to a change in the beam profile at high gun energy, which is not included in our model. Nonetheless, the agreement between the measurement and model is excellent overall.

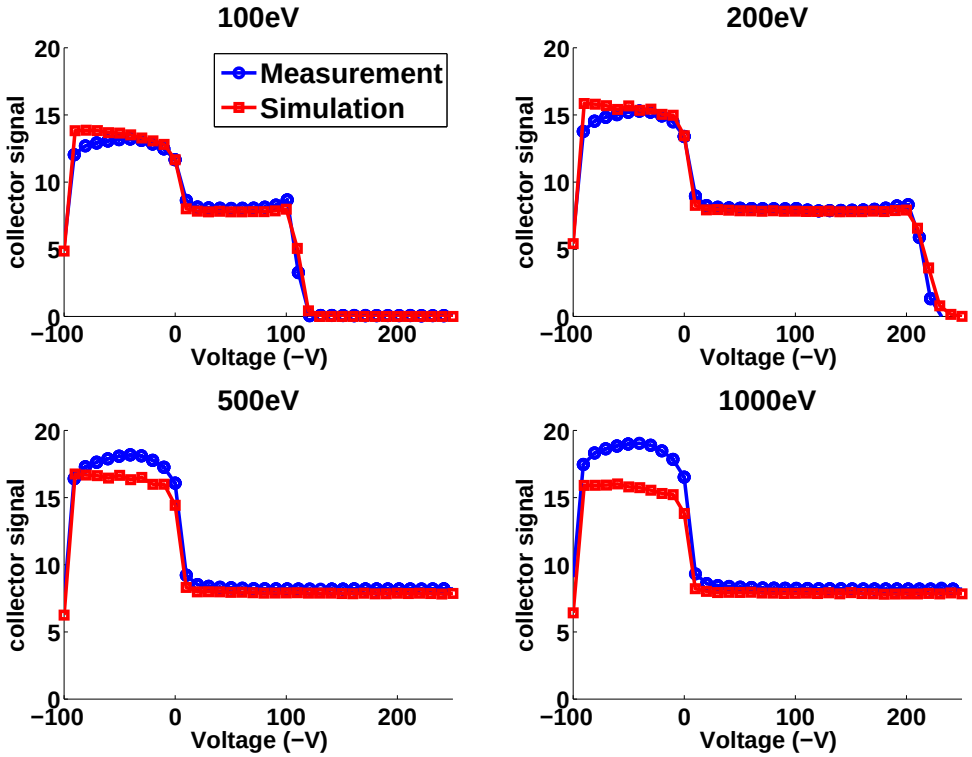

Figure 2.20: Comparison of bench measurement and simulation, with electron gun energy 100 eV (top left), 200 eV (top right), 500 eV (bottom left), and 1 keV (bottom right).

2.5 Simulations and comparison with data

The large quantity of RFA data obtained during the CESR-TA program necessitates a systematic method for detailed analysis. Our approach has been to take a large set of voltage scan data, and find a set of simulation parameters that bring data and simulation into as close agreement as possible. Simultaneously fitting data taken under a wide variety of beam conditions gives us confidence that our model is producing a reasonable description of the growth and dynamics of the electron cloud.

More specifically, we want to minimize χ^2, as defined in Eq. (2.2). Here $\mathbf{y_d}$ is a vector of data points, $\mathbf{y_s}$ is a vector of simulation points, β_0 is the vector of

nominal parameter values, and β is the vector of new parameter values. $\mathbf{X}$ is the Jacobian matrix ($X_{i,j} \equiv \frac{\partial y_i}{\partial \beta_j}$), and $\mathbf{W}$ is a diagonal matrix whose elements are $\frac{1}{\sigma_i^2}$, where σ_i is the error on data point i. Both the data and simulation can contribute to this error. The T superscript denotes the matrix transpose. Note that $\mathbf{X}$ and $\mathbf{y_s}$ are both evaluated at $\beta_\mathbf{0}$. Once a new set of parameter values is obtained, the process can be repeated with this new set as the "nominal" values. As this method uses a linear approximation for the dependence of $\mathbf{y_s}$ on β, it will need to be iterated a few times before it converges on the actual minimum value of χ^2.

$$\chi^2 = \varepsilon^T \, \mathbf{W} \, \varepsilon \tag{2.2}$$

$$\varepsilon \equiv \mathbf{y_d} - (\mathbf{y_s} + \mathbf{X}(\beta - \beta_\mathbf{0})) \tag{2.3}$$

2.5.1 Simulation Parameters

See section 2.5.1 for a general discussion of POSINST parameters.

Generally speaking, the true secondary yield and quantum efficiency (`dtspk` and `queffp`) need to be included in the fitting procedure to get good agreement with the RFA data. Other strong parameters include `P1epk`, `P1rinf`, and `powts`, but they are highly correlated with each other (i.e. have similar effects on the RFA simulation), so only one of the three is needed. For the uncoated chambers (Al and Cu), we varied `P1epk`. For the coated chambers (aC, TiN, DLC, NEG), we found this parameter usually tended towards 0 in the fits, so we assumed a low value (.05), and varied `P1rinf` instead. The quantum efficiency was allowed to be different for different beam energies and species,

Table 2.4: Summary of relevant POSINST parameters. The last column indicates whether the parameter was used in fits always (A), in some cases (S), or never (N).

Parameter	Description	Fit?
dtspk	True secondary yield	A
P1epk	Elastic yield	S
P1rinf	Rediffused yield	S
dtotpk	**Total peak yield**	**N**
E0epk	Peak yield energy	N
powts	Shape parameter	N
queffp	Quantum efficiency	A

since it will in general depend on photon energy [3]. In addition, the analysis uses one arbitrary parameter: a "chamber hole SEY," which is an overall scaling of the effect of secondaries generated in the RFA on the low energy signal (Fig. 2.19). The fitted values for this parameter are within the expected range; a typical number for the effective hole SEY is on the order of 1.5.

Table 2.4 summarizes the POSINST parameters most relevant to our analysis and indicates whether the parameter was used in the fits. Note that `dtotpk` is not an independent parameter, but rather the sum of the three SEY components (`dtspk`, `P1epk`, and `P1rinf`) at the peak yield energy (`E0epk`). It is highlighted in bold, as it is generally considered the most significant parameter in describing the SEY curve.

2.5.2 Fitting the Data

In performing the χ^2 analysis, the choice of which data to fit and which simulation parameters to vary are both important. We want a set of parameters that have a strong effect on the simulations, and a set of voltage scans that determine

Table 2.5: List of beam conditions used for one round of fitting (15W Al chamber, May 2010), and which parameter they most strongly determined

Bunches	Bunch current	Bunch Spacing	Beam Energy	Parameter
-	(mA)	(ns)	(GeV)	-
45 e^-	2.89	4	5.3	`dtspk`
45 e^+	2.3	14	2.1	`dtspk`
20 e^+	7.5	14	2.1	`dtspk`
20 e^-	2.8	14	5.3	`dtspk`
20 e^+	2.8	4	4	`dtspk`
9 e^-	3.78	280	2.1	`P1epk`
20 e^+	10.75	14	5.3	`P1epk`
9 e^+	3.78	280	2.1	`P1epk`
9 e^+	3.78	280	4	`P1epk`
9 e^+	4.11	280	5.3	`P1epk`
45 e^+	0.75	14	5.3	`queffp`
45 e^-	1.25	4	5.3	`queffp`
45 e^+	0.75	14	4	`queffp`
45 e^+	0.75	14	2.1	`queffp`
45 e^-	2	14	2.1	`queffp`

these parameters as independently as possible. For example, the true secondary yield is highest for ~300 eV electrons, so it is best determined by data taken under beam conditions where a typical electron energy is on that order. This tends to mean short bunch spacing and moderately high current. The elastic yield mainly affects the decay of the cloud, when most of the cloud particles have low energy. It is best derived from data where the cloud is repeatedly generated and allowed to decay, i.e. for large bunch spacing. The quantum efficiency is most significant in regimes where secondary emission is less important, namely for low current data. Table 2.5 gives a list of data sets used in one round of fitting, and indicates which parameter was best determined by each.

Several sources of error can complicate the analysis, and must be added (in quadrature) when constructing the error matrix (**W** in Eq. (2.2)). They are listed below. For the purpose of comparison, a typical signal in the 15E/W RFAs is on

the scale of 100's of nA.

- Noise in the measurements (typically quite small, a few tenths of a nA)
- Statistical errors in simulations. This can be reduced by increasing the number of macroelectrons used in the simulation, at the cost of increased run time. Typical values are on the order of a few nA.
- A general error of 10% was added to account for systematic uncertainties in the data. One such uncertainty is unevenness in bunch currents along the train, which is not accounted for in the simulation. The choice of 10% is somewhat arbitrary, but was chosen to reflect our confidence in the repeatability of the measurements.
- We have observed a slow drift of baseline (zero current value) in measurements, on the order of ~ .2% of full scale. This amounts to ~20 nA on the lowest gain setting, and ~.02 nA on the highest one (2 nA for a typical case).
- An extra 20% error was added to the signal in the simulation caused by beam pipe hole secondaries, to account for uncertainty in the modeling of this phenomenon. Again this choice is somewhat arbitrary.
- Since the gradient for the Jacobian matrix ($\mathbf{X}$) is determined by simulation, it will also have an associated error. This cannot be included in the $\mathbf{W}$ matrix, because it will be different for each parameter. However, it can still be calculated, and its effect on the final parameter errors can be estimated.

2.5.3 Results

Figs. 2.21 and 2.22 show some of the results of the χ^2 analysis, for an uncoated aluminum drift chamber. The plots compare both the transverse and energy distribution of the data and fitted simulation. The error bars shown reflect all of the uncertainties described above. Overall the two are in good agreement for a wide variety of beam conditions. The biggest discrepancy between data and simulation occurs for high current electron beam data. These are the conditions most likely to produce ion effects, which are not included in our model, and may be leading to this discrepancy.

The covariance matrix for the parameters is $(\mathbf{X}^T\,\mathbf{W}\,\mathbf{X})^{-1}$. The standard errors on each parameter are equal to the square root of the diagonal elements of this matrix. These errors are one dimensional 68% confidence intervals for each parameter individually, without regard for the values of the other parameters. The errors extracted from the covariance matrix are multiplied by the "χ^2 per degree of freedom" ($\frac{\chi^2}{n-p}$, where n is the number of data points and p is the number of parameters fitted). Effectively this scales up the uncertainty on the data points, to include (in a somewhat ad hoc manner) any errors that have been left out of the analysis. The values listed for the error bars also include an estimate of the uncertainty introduced by errors in the Jacobian matrix, which is added in quadrature to the standard error. The correlation coefficient of two parameters is defined as $\rho \equiv \frac{C_{i,j}}{\sqrt{C_{i,i}\times C_{j,j}}}$, where $C_{i,j}$ is the i, jth element of the covariance matrix. In general the correlation between parameters is significant. For example, in the fits shown in Figs. 2.21 and 2.22, ρ = .42 for `dtspk` and `P1epk`, .22 for `dtspk` and `queffp`, and .31 for `P1epk` and `queffp`.

It should be noted that, given the large number of parameters involved in the

analysis and the limited range in which we have allowed them to vary, it is impossible to conclusively state that we have arrived at the global minimum value of χ^2 in parameter space. Nonetheless, the ability of this method to achieve a good fit for data taken under a wide variety of beam conditions strongly implies that the primary and secondary emission models used are reproducing reality to a reasonable degree.

The best fit values and 68% confidence intervals for the aluminum chamber fit are shown in Table 2.6. This chamber was installed in the Q15W location (see Section 2.1.2), and the fit used data taken during May 2010 (listed in Table 2.5). Tables 2.7 through 2.11 give the best fit values for (fully processed) aC, TiN, DLC, bare Cu, and NEG, respectively. In these tables, the quantum efficiency best fit values are given for positron beam data; the complete set of quantum efficiency fits is shown in Table 2.12.

Each of these results represents a fit using to a series of voltage scans done during one CESR-TA machine studies run, typically within a few days of each other. Several such fits were done for most of the chambers, and the results were usually found to be consistent, with a few exceptions. In particular, some of the fits for aC showed a higher quantum efficiency, but somewhat lower rediffused yield. This may represent a different state of processing of the chamber. In the results presented below, the fit with the lowest χ^2 for each chamber was chosen.

Some of the more significant features of these results include:

- The true secondary yield (dtspk) for the uncoated Al chamber was found to be very high (> 2). All of the coated chambers (aC, TiN, DLC, and NEG) had much lower values, corresponding in all cases to a peak SEY ≤ .9. The

value for TiN and DLC in particular are very low, implying a peak SEY on the order of 0.7.

- The DLC fit also required a very low value for the "chamber hole SEY" parameter described above. This could be understood as compensating for a suppression of the low energy signal due to charging of the chamber (see Section 2.3.2).
- The best fit values for quantum efficiency were also lower for the coated chambers. Amorphous carbon consistently had the lowest values, less than 5% for all cases.
- Since we don't have a direct measurement of the SEY curve for NEG, the initial values for the parameters were (somewhat arbitrarily) taken from TiN. The fitted values for NEG indicate a much higher rediffused yield than the other coated chambers.
- The best fit value for the elastic yield was found to be low for both uncoated (Al and Cu) chambers. This parameter was not varied for the coated chambers, but the fits were generally found to be better if a very low value (.05) was assumed. For these chambers, the rediffused yield was varied instead.
- In most cases, the quantum efficiency fit was significantly higher for 5.3 GeV than for 2.1 GeV.

The SEY curves generated by the best fit parameters for each chamber are shown in Fig. 2.23.

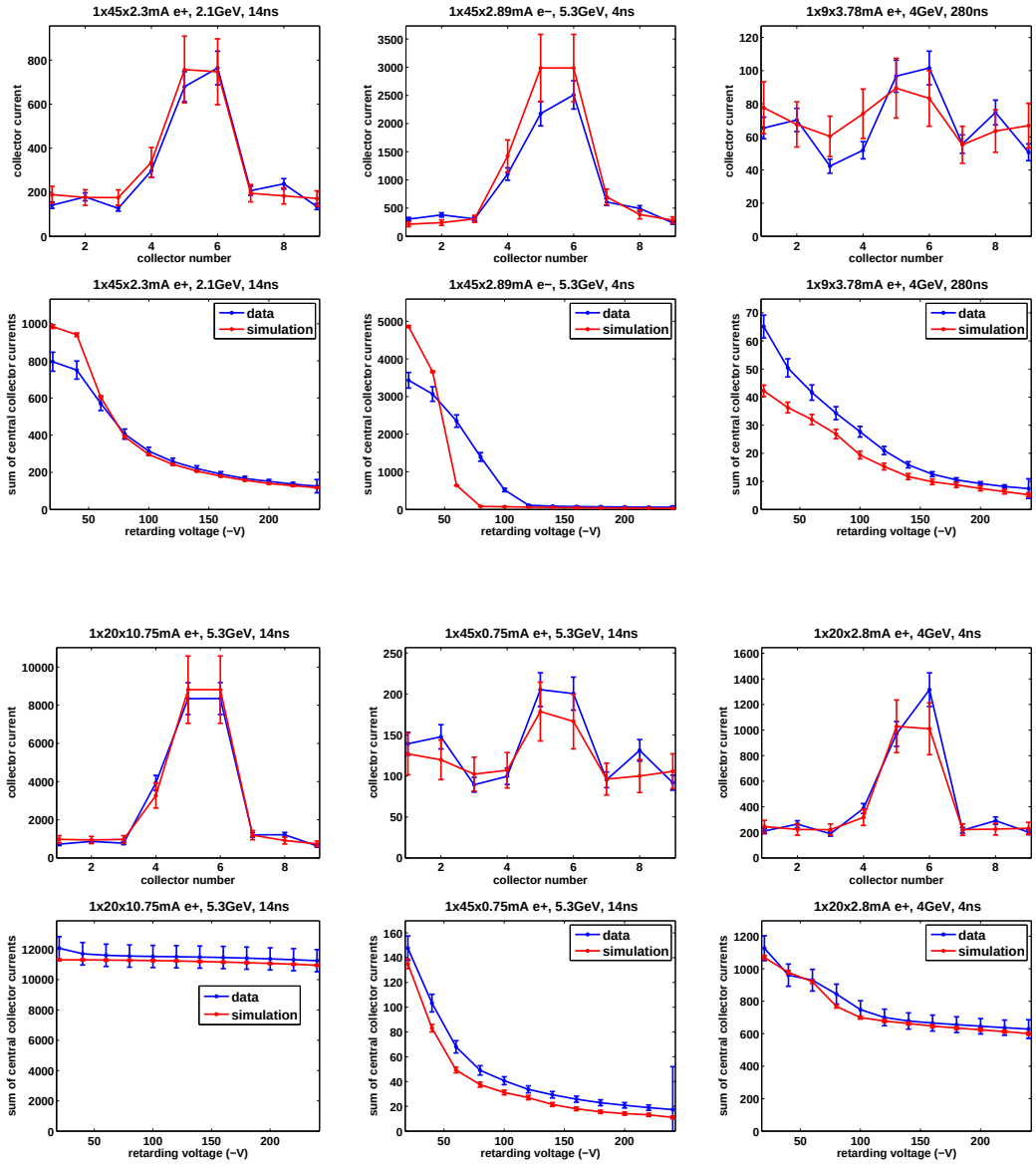

Figure 2.21: Comparison of Q15W Al RFA data and simulation, using best fit parameters (Table 2.6). The top plots show the total signal across the 9 RFA collectors (with +50 V on the grid); the bottom plots show the signal in the central three collectors vs retarding voltage.

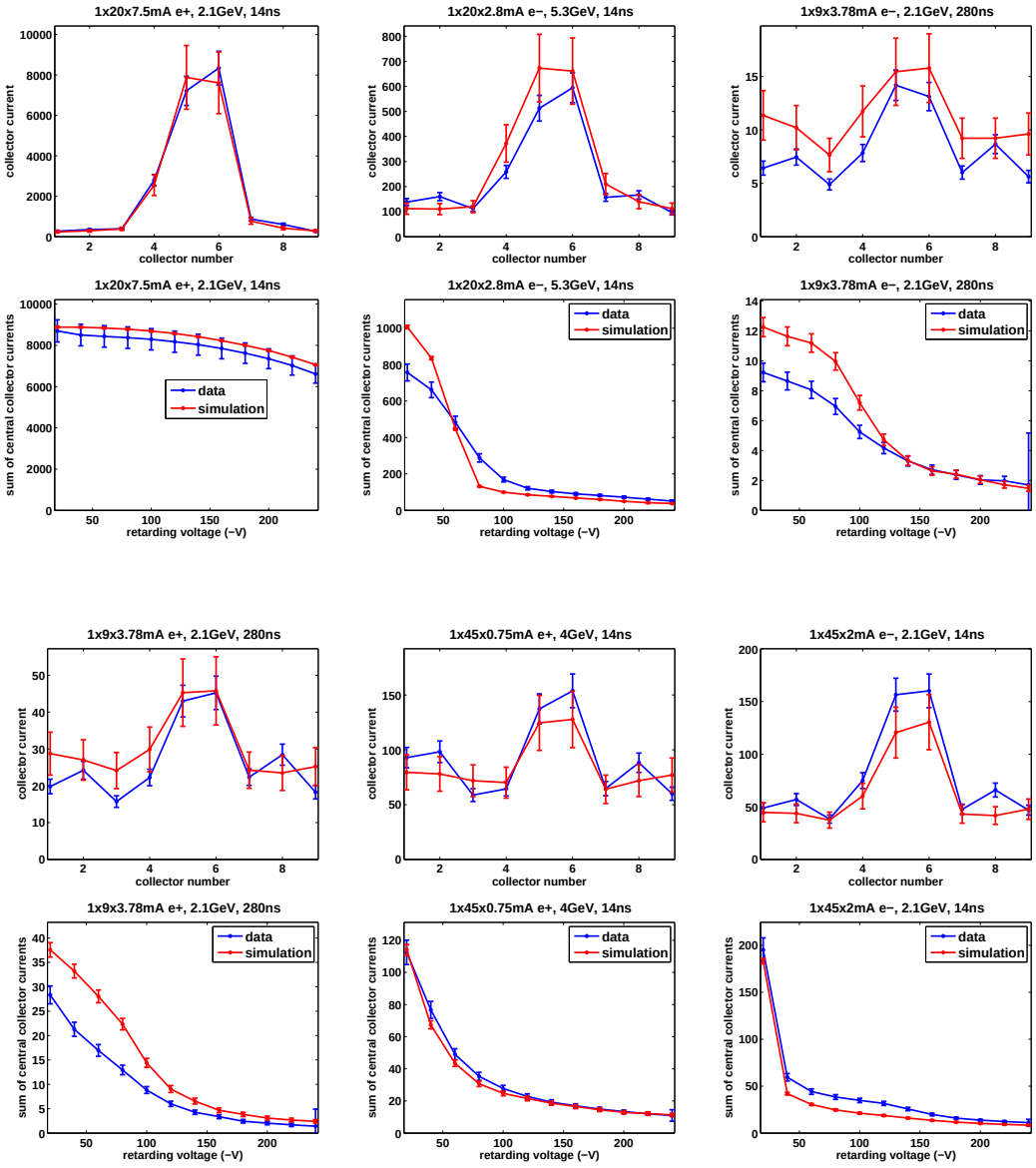

Figure 2.22: Comparison of Q15W Al RFA data and simulation, using best fit parameters (Table 2.6). The top plots show the total signal across the 9 RFA collectors (with +50 V on the grid); the bottom plots show the signal in the central three collectors vs retarding voltage.

Table 2.6: Best fit parameters- Q15W aluminum chamber, May 2010

Parameter	Base Value	Final Value
dtspk	1.37	2.08 ± .09
P1epk	.5	.36 ± .03
P1rinf	.2	.2
dtotpk	**1.59**	**2.3 ± .1**
E0epk	280eV	280eV
powts	1.54	1.54
queffp, 5.3GeV	.1	.10 ± .01
queffp, 2.1GeV	.1	.11 ± .01

Table 2.7: Best fit parameters- Q15E aC coated chamber, December 2010

Parameter	Base Value	Final Value
dtspk	.76	.59 ± .05
P1epk	.05	.05
P1rinf	.2	.30 ± .05
dtotpk	**.98**	**.91 ± .07**
E0epk	300eV	300eV
powts	1.77	1.77
queffp, 5.3GeV	.1	.046 ± .005
queffp, 2.1GeV	.1	.036 ± .005

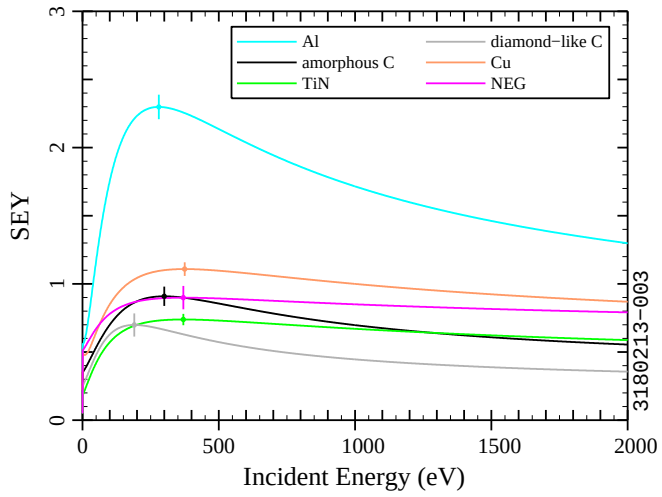

Figure 2.23: Secondary electron yield curves generated by the best fit parameters for each chamber (Tables 2.6 - 2.11). Error bars are shown for the peak yield values.

Table 2.8: Best fit parameters- Q15W TiN-coated chamber, December 2010

Parameter	Base Value	Final Value
dtspk	.73	.59 ± .03
P1epk	.05	.05
P1rinf	.2	.13 ± .03
dtotpk	**.85**	**.75 ± .04**
E0epk	370eV	370eV
powts	1.32	1.32
queffp, 5.3GeV	.1	.089 ± .007
queffp, 2.1GeV	.1	.050 ± .004

Table 2.9: Best fit parameters- Q15E DLC coated chamber, April 2012

Parameter	Base Value	Final Value
dtspk	.76	.48 ± .06
P1epk	.05	.05
P1rinf	.2	.20 ± .06
dtotpk	**.98**	**.70 ± .08**
E0epk	190eV	190eV
powts	1.77	1.77
queffp, 5.3GeV	.1	.099 ± .011
queffp, 2.1GeV	.1	.042 ± .006

Table 2.10: Best fit parameters- Q14E bare Cu chamber, May 2010

Parameter	Base Value	Final Value
dtspk	.82	.81 ± .05
P1epk	.5	.22 ± .07
P1rinf	.28	.28
dtotpk	**1.12**	**1.11 ± .09**
E0epk	375eV	375eV
powts	1.38	1.38
queffp, 5.3GeV	.1	.15 ± .03
queffp, 2.1GeV	.1	.025 ± .008

2.6 Summary

Electronic properties of material surfaces, such as quantum efficiency and secondary emission yield, are traditionally measured employing dedicated, well-controlled laboratory devices applied to clean, smooth surfaces. The analysis

Table 2.11: Best fit parameters- L3 NEG-coated chamber, December 2010

Parameter	Base Value	Final Value
dtspk	.73	.42 ± .07
P1epk	.05	.05
P1rinf	.2	.46 ± .05
dtotpk	**.97**	**.90 ± .09**
E0epk	370eV	370eV
powts	1.32	1.32
queffp, 5.3GeV	.1	.14 ± .02
queffp, 2.1GeV	.1	.03 ± .01

Table 2.12: Table of best fit quantum efficiencies (in percent)

Material	2.1 GeV, e^+	2.1 GeV, e^-	4 GeV, e^+	5.3 GeV, e^+	5.3 GeV, e^-	Average
Al	11.3 ± 1.4	8.0 ± 1.1	10.0 ± 1.2	10.3 ± 1.2	10.5 ± 1.4	10.0
Cu	2.5 ± .8	4.7 ± .7	15.0 ± 2.0	15.3 ± 2.8	12.1 ± 1.8	9.9
TiN	4.9 ± .2	-	-	8.9 ± .7	5.0 ± .4	6.3
aC	3.6 ± .5	-	-	4.6 ± .6	4.9 ± .6	4.4
DLC	4.5 ± .6	7.1 ± .6	-	9.1 ± 1.1	7.1 ± .6	7.0
NEG	2.9 ± .9	-	-	14 ± 2	-	8.5

presented here, on the other hand, presents the determination of several model parameters via a simultaneous, multi-parameter fit to data obtained with RFAs installed in the CESR-TA vacuum chamber. Thus, while none of the above-mentioned parameters is determined with great precision, our exercise amounts to a more global fit to the model, and yields reasonable values for the parameters. In combination with many other kinds of measurements (published separately [19, 23, 36, 37]) within the CESR-TA program, our results lend validity to the electronic model embodied in the simulation code, and thus strengthens our confidence in its more general applicability.

Our approach has the additional advantage that it allows the assessment of the performance of various chamber materials vis-a-vis the electron-cloud problem for actual chamber surfaces within a realistic storage ring environment. As such, our analysis takes intrinsic account of such issues as surface roughness,

material composition, and beam conditioning.

CHAPTER 3

DIPOLE RFA STUDIES

In the presence of a dipole magnetic field, an electron will undergo helical motion, spiralling around the field lines. For a standard dipole magnet in an accelerator (with strength ~ 1 kG), a typical cloud electron (with energy ~ 10 - 100 eV) will have a cyclotron radius on the order of a few hundred μm. In other words, the motion of the electron will be approximately one dimensional, along the direction of the dipole field. This "pinning" of the motion to the field lines results in an electron cloud buildup that is both qualitatively and quantitatively different from the drift case.

3.1 Dipole Instrumentation

A more detailed description of the design and construction of the dipole and quadrupole RFAs can be found in [1]; here we present only a brief overview.

RFA data have been taken in the presence of a dipole field, both in a standard CESR dipole, and in a specially designed chicane which was built at SLAC [41] and inserted in the L3 region of CESR ring (see Fig. 1.7). Table 3.1 provides a summary of the properties of these RFAs.

Table 3.1: Dipole RFA styles deployed in CESR

Type	Grids	Collectors	Grid Trans.	Field Strength
CESR dipole	1	9	40%	790 G (2.1 GeV) - 2010 G (5.3 GeV)
SLAC chicane	3	17	90%	0 - 1460 G

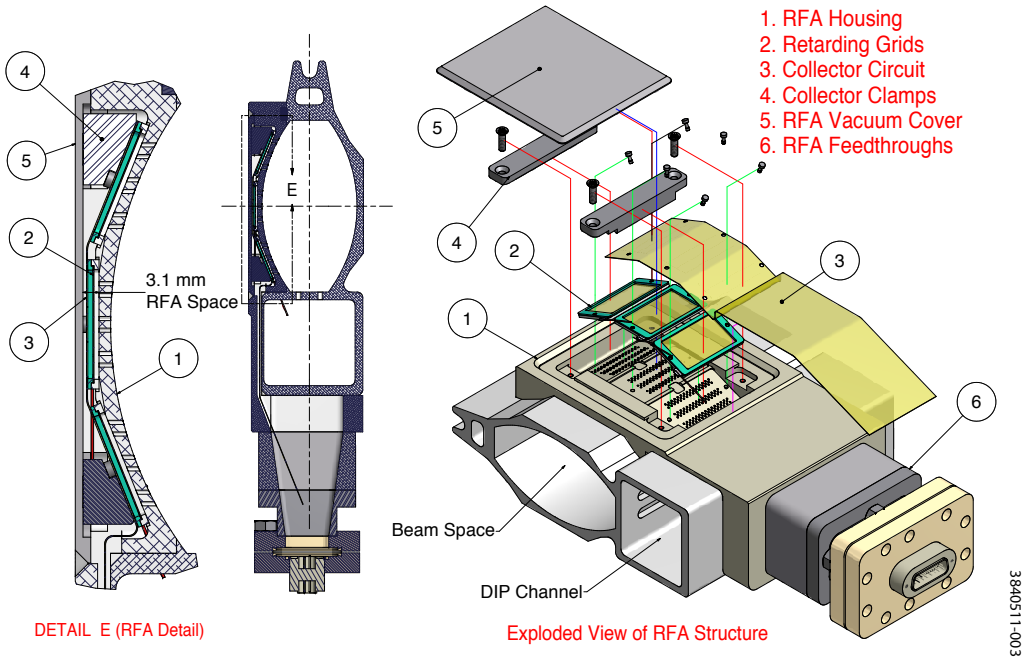

Figure 3.1: RFA design detail for a CESR dipole chamber.

CESR Dipole The RFA style deployed inside a CESR dipole is identical to the "thin" drift style (Section 2.1.4), except a lower efficiency grid was used (the "etched" grid, see Table 2.3). Designed to fit in the limited (3 mm) dipole aperture, this RFA has only a single (retarding) grid. Fig. 3.1 shows a detailed engineering diagram for the thin dipole RFA. It was installed in 12W arc in CESR. The magnetic field at this location depends on the beam energy: 790 G at 2.1 GeV, 1520 G at 4 GeV, and 2010 G at 5.3 GeV.

Chicane Dipoles A PEP-II 4-element dipole-magnet chicane was installed in the CESR-TA L3 experimental region (see Figure 1.7) for the continuation of studies of EC in a dipole field. The field of the chicane dipoles can be varied over the range of 0 to 1.46 kG. Most of our measurements were done in a nominal dipole field of 810 G. As shown in Figure 3.2, the 4 dipoles are spaced 73 cm apart, with aluminum beam pipes on either side, for a total length of ~4.2 m.

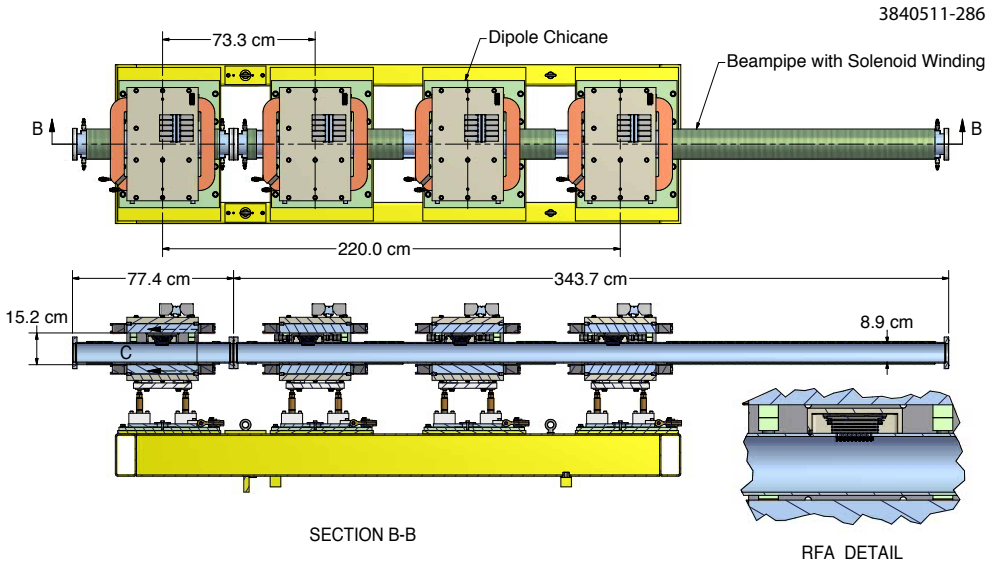

Figure 3.2: PEP-II 4-dipole magnet chicane and RFA-equipped EC chambers.

Four RFAs were installed on these test chambers, with each of the RFAs located within the dipole magnets. Each of the magnets tests a different type of surface- one is bare Aluminum, two are TiN coated, and one is both grooved and TiN coated. The grooves are triangular with a depth of 5.6 mm and an angle of 20°. Figure 3.3 shows the structure of these RFAs. Because there is no aperture limitation for these magnets, the RFAs were designed with three (high efficiency) grids, with a generous 5 mm spacing. Retarding voltage is applied to the middle grid.

3.2 Measurements

Fig. 3.4 shows a retarding voltage scan done with both the CESR dipole and Aluminum chicane RFAs. In both cases, one can see a strong multipacting peak in the central collector, aligned with the horizontal position of the beam. These can be compared with the TiN coated chicane RFA (Fig. 3.5), in which the peak

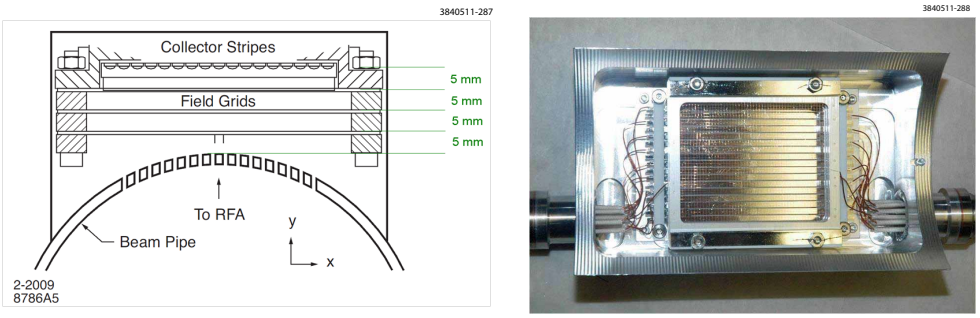

Figure 3.3: Four RFAs were welded onto the chicane beam pipes. LEFT: Cross-section view showing the structure of these RFAs. RIGHT: Photo showing the assembled RFA in its aluminum housing, welded on the top of the chicane beam pipes.

is greatly suppressed.

3.2.1 Bifurcation of Central Peak

For high bunch currents, we have observed a bifurcation of the central multipacting peak into two peaks with a dip in the middle. This is demonstrated in Fig 3.6, which shows the signal in all 17 RFA collectors vs beam current. Bifurcation occurs when the average energy of electrons in the center of the beam pipe is higher than the peak energy of the SEY curve, so that the location of the effective maximum yield is actually off center. The higher the bunch current, the further off center these peaks will be.

3.2.2 Cyclotron Resonances

By varying the strength of the chicane magnets, we can also study the behavior of the cloud at different dipole magnetic field values. Fig. 3.7 shows an example of RFA data taken as a function of magnetic field strength. The most promi-

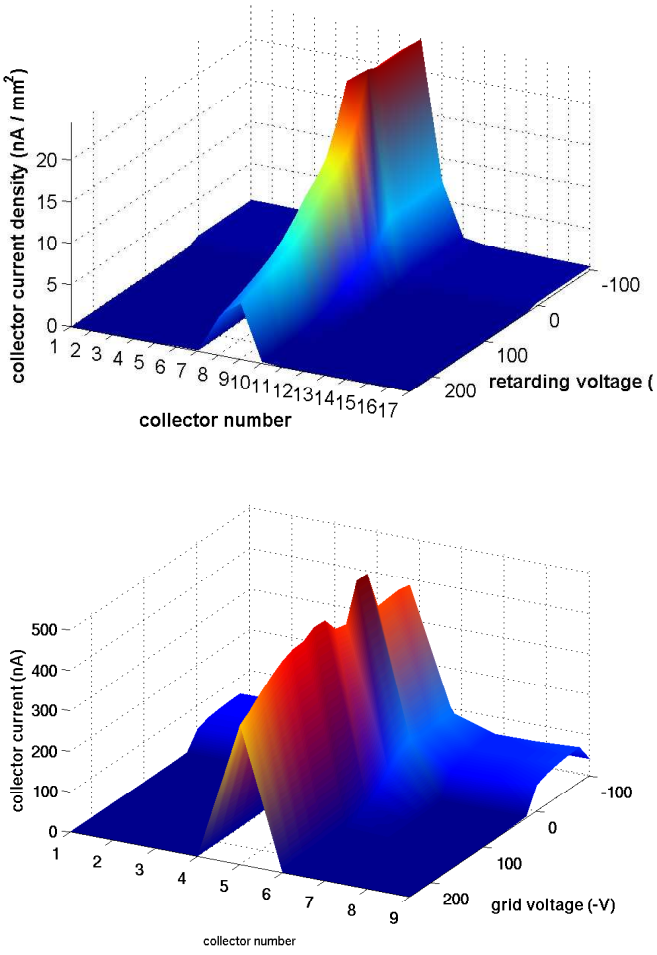

Figure 3.4: Typical Al dipole RFA voltage scans: 1x45x1.25mA e+, 5.3GeV, 14ns. Top: SLAC chicane RFA (810 Gauss); Bottom: CESR dipole RFA (2011 Gauss). In the top case, the central collector is no. 9, while in the bottom case it is no. 5.

nent feature of the data is regularly occurring spikes or dips in all three plotted chambers. These correspond to "cyclotron resonances," which occur whenever the cyclotron period of cloud electrons is an integral multiple of the bunch spacing [16]. For 4ns bunch spacing we expect them every 89 Gauss, which is what is seen in the data. Another interesting feature of this measurement is that these resonances appear as peaks in the RFA signal in the Aluminum chamber, but as dips in the coated chambers. This qualitative difference in the behavior of the two chamber materials is explained in Section 3.5.2.

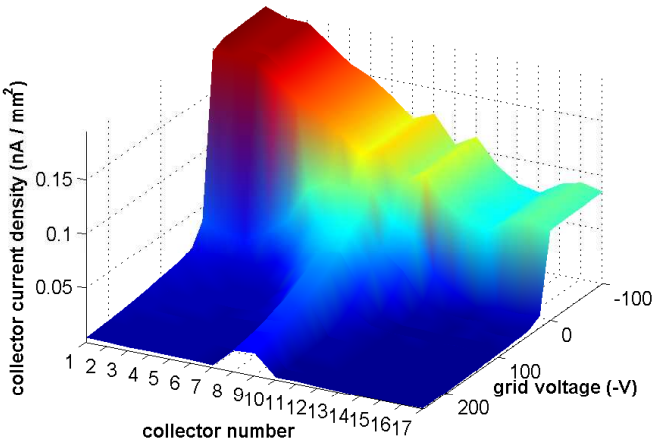

Figure 3.5: Voltage scan in TiN coated chicane chamber: 1x45x1.25mA e+, 5.3GeV, 14ns.

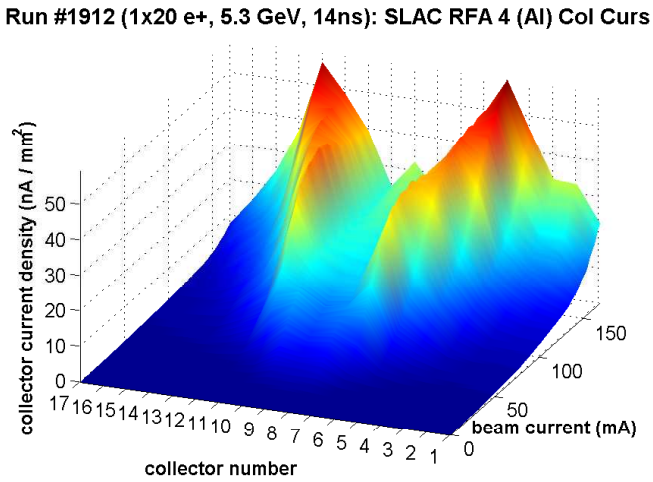

Figure 3.6: Bifurcation of peak cloud density in a Al dipole: 1x20 e+, 5.3GeV, 14ns

3.2.3 Bunch Spacing Studies

Because the electron cloud distribution can change over the course of nanoseconds (or shorter time scales), it is interesting to investigate its behavior as a function of bunch spacing. At CESR-TA we have taken RFA data with bunch spacings varying from 4ns to 112ns.

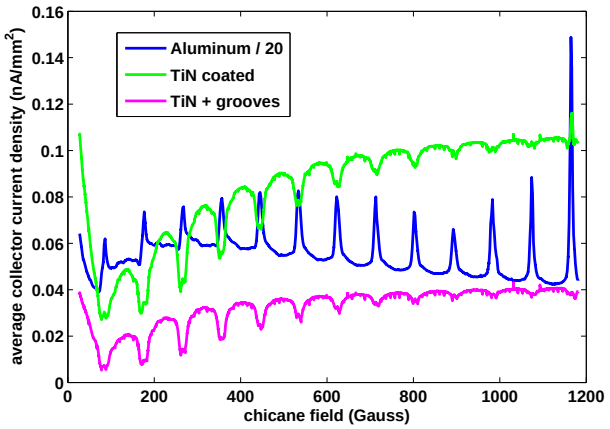

Figure 3.7: RFA signal as a function of chicane magnetic field: 1x45x1mA e+, 5GeV, 4ns. Cyclotron resonances are observed every 89G. Note that the Aluminum chamber signal is divided by 20.

Fig. 3.8 shows the signal in the central collector of two dipole RFAs as a function of bunch spacing. The top plot is for the Aluminum SLAC chicane RFA; the bottom is for the CESR dipole RFA (see Fig. 3.4). The SLAC chamber has a half-height of 4.4cm, while the CESR RFA has a half-height of 2.5cm.

For the SLAC RFA, we observe two distinct peaks in the positron data, at approximately 14ns and 60ns. The electron beam data shows almost no signal for bunch spacings less than 36ns, and is peaked around the same place as second the positron peak. The enhancement of the signal at 60ns could be due to a resonance between the bunch spacing and the cloud development (often called a "multipacting resonance"). This effect will be enhanced by the dipole field, which renders the motion of the electrons mostly one dimensional.

A very simple model for a multipacting resonance is that if the time for a typical secondary electron to travel to the center of the beam pipe is equal to the bunch spacing, this electron will be kicked strongly by the beam, and is likely to produce more secondary electrons. In reality, peak secondary production

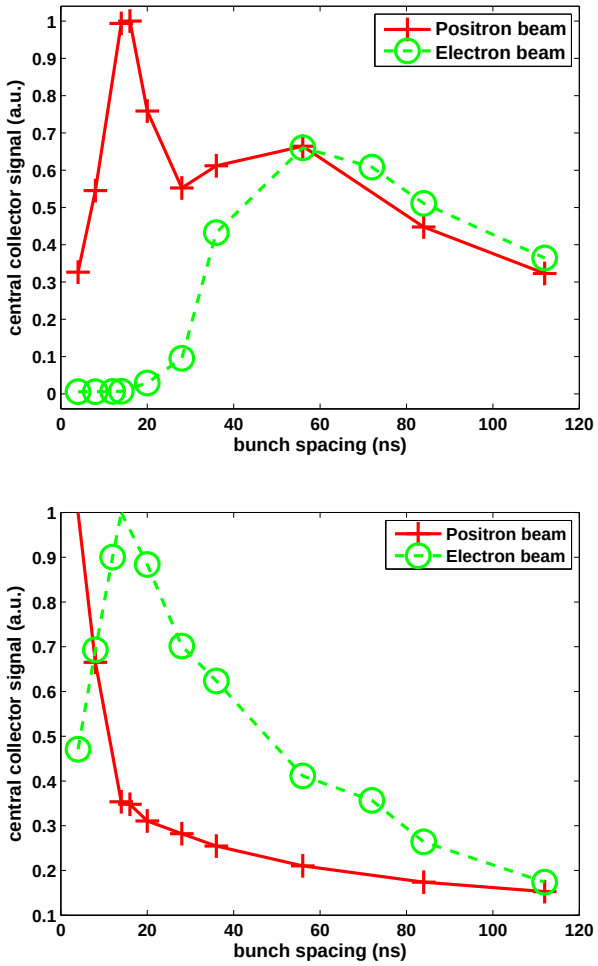

Figure 3.8: Central collector signal in a dipole RFA as a function of bunch spacing, for a 20 bunch train with 3.5mA (5.6×10^{10} particles) per bunch, at 5.3 GeV. Top: SLAC chicane RFA, bottom: CESR dipole RFA

will occur when this electron is given an amount of energy corresponding to the peak of the SEY curve. However, for aluminum the SEY is greater than 1 well into the keV range, so an electron anywhere near the beam is a candidate to produce more secondaries. Thus we expect the "resonance" to be somewhat broad.

If we ignore the time for the kicked electron to travel to the beam pipe wall (which will be small if the kick is strong), the resonance condition is simply

$t_b = b/v_{sec}$, where t_b is the bunch spacing, b is the chamber half-height (i.e. the distance from the wall to the beam), and v_{sec} is a characteristic secondary electron velocity. For a 1.5eV electron, this peak will occur at 61ns. The fact that there is a finite width to the secondary energy distribution will further smear out the peak.

The lower energy peak in the positron data could be a higher order multipacting resonance, where it takes two bunches to set up the resonance condition. Here we consider the case where the first bunch gives some additional energy to the electron, so that it makes it to the center of the chamber in time for the second bunch. If we again neglect the time for the kicked electron to reach the beam pipe wall, the resonance condition becomes:

$$t_{b,2} = \frac{b-r_1}{v_{sec}} = \frac{r_1}{v_2} \tag{3.1}$$

$$v_2 = v_{sec} + \frac{2cN_b r_e}{r_1} \tag{3.2}$$

Here r_1 is the distance from the electron to the beam during the first bunch passage, v_2 is the velocity of the electron after it is kicked by the first bunch, N_b is the bunch population and r_e is the classical electron radius. Solving for $t_{b,2}$ gives us Eq. 3.3, where we have defined $k \equiv 2cN_b r_e$.

$$t_{b,2} = \frac{k + 3bv_{sec} - \sqrt{k^2 + 6kbv_{sec} + b^2 v_{sec}^2}}{4v_{sec}^2} \tag{3.3}$$

For a 1.5eV secondary electron, $t_{b,2}$ is 11ns, somewhat less than the 14ns that is observed. A more sophisticated model (which would include, among other things, the time for the kicked electron to reach the wall) may yield a more accu-

rate result. Note that this resonance condition applies only to positron beams, so only one peak is predicted for the electron data (which is what we find). Overall, a multipacting scenario with a 1.5eV peak secondary energy is approximately consistent with the SLAC chicane data, for both the positron and electron beam data.

The predictions for our CESR dipole (Fig. 3.8, bottom) would then be t_b = 34ns and $t_{b,2}$ = 4ns. The former is higher than what is observed, though the latter is consistent with the data. A better fit would be for an 8eV electron, then t_b = 15ns and $t_{b,2}$ = 3ns. It is also possible that a more sophisticated model would fit the CESR dipole data better.

3.3 Mitigation comparison

Fig. 3.9 shows a current scan comparison between three of the chicane RFAs. We observe a large difference between uncoated and coated chambers. At high beam current, the TiN coated chamber shows a signal smaller by two orders of magnitude than the bare Al chamber, while the coated and grooved chamber performs better still.

A similar comparison, done with an electron beam, is shown in Fig. 3.10. Here we observe a threshold current, at which the aluminum chamber signal "turns on," and shows a dramatic increase with current. This threshold occurs when the kick from the electron beam on low energy cloud particles near the vacuum chamber (which drives them back into the wall) is strong enough to result in significant secondary emission. The threshold is not observed in any of the mitigated chambers, where the secondary emission yield is below unity

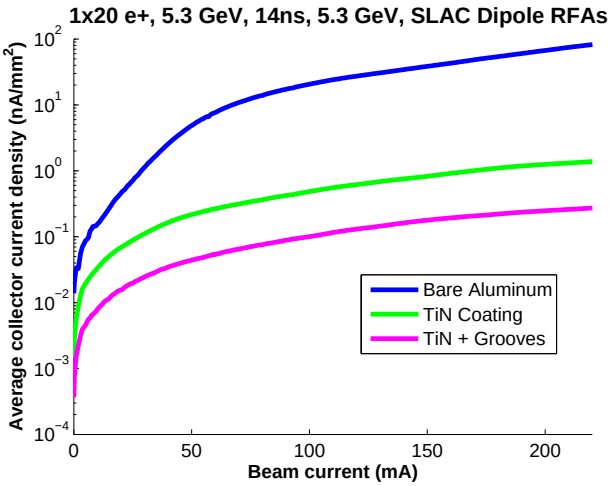

Figure 3.9: Dipole RFA mitigation comparison, 1x20 e+, 5.3GeV, 14ns, 810 Gauss.

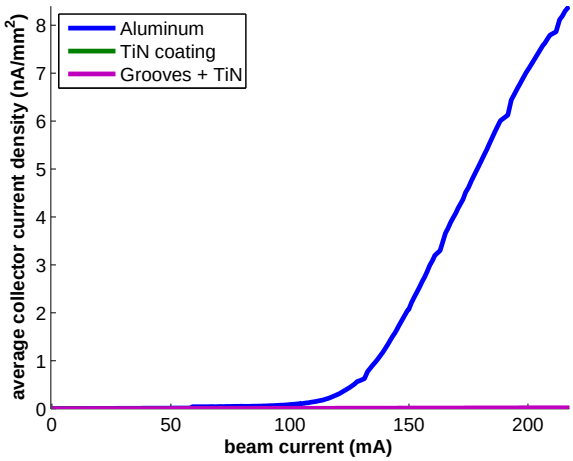

Figure 3.10: Dipole RFA mitigation comparison, 1x20 e-, 5.3GeV, 14ns, 810 Gauss.

even at high energies. It is present in electron beam data with the CESR dipole RFA (Fig. 3.11), though the threshold occurs at a lower current. This is what one would expect, since the chamber at 12W is narrower than at L3, so the beam kicks at the wall will be stronger.

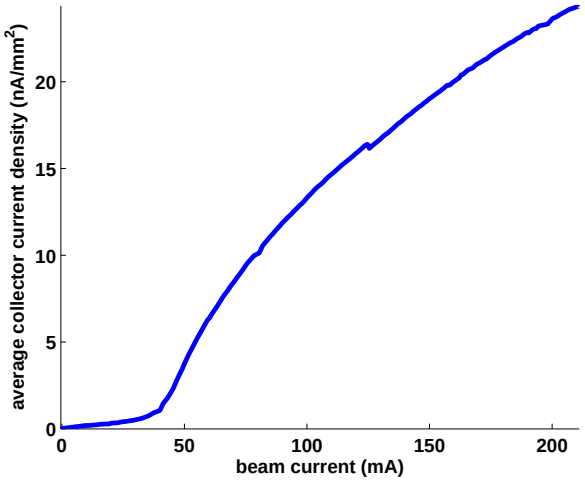

Figure 3.11: Threshold behavior in CESR dipole RFA, 1x20 e-, 5.3GeV, 14ns

3.4 Dipole RFA modeling

A model for both types of dipole RFA has been incorporated into POSINST [26]; as in the drift case (see Section 2.4) predicted RFA signals are produced automatically by the simulation.

Modeling an RFA in a dipole magnetic field presents a unique set of challenges. Fig. 3.12 shows the efficiency (probability of making it through the beam pipe hole) as a function of incident angle in this RFA, calculated using a specialized particle tracking code (Section 2.4). Note that low energy particles have a very high efficiency, due to their small cyclotron radius.

In addition, when simulating a dipole RFA, one must accurately model the exact locations of the beam pipe holes. This is because in a strong dipole field, electrons are mostly pinned to the field lines, and do not move very far transversely. So in a real measurement, the RFA will deplete the cloud in precisely the region it is sampling, i.e. under the beam pipe holes. Not taking this into ac-

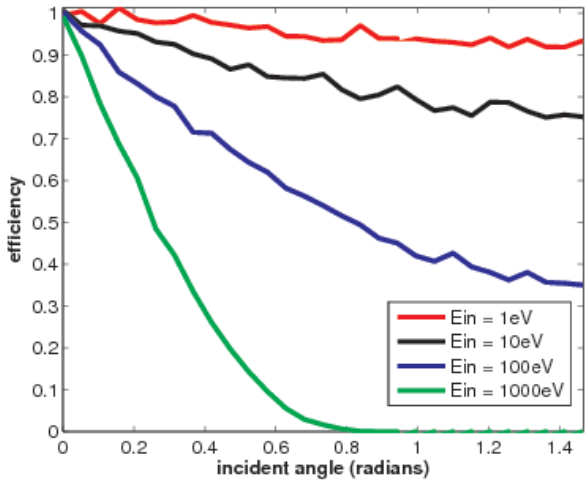

Figure 3.12: Simulated RFA efficiency vs incident angle for a SLAC chicane dipole RFA, with a .081 T magnetic field.

count will result in an overestimate of the RFA signal, especially at low energy (where the electrons are most strongly pinned to the field lines).

3.5 Simulations

Using the model described above, and SEY parameters taken from fits to the drift data (Section 2.5.3), we ran simulations for the dipole RFAs, for various beam conditions. Fig. 3.13 shows a typical example, for the Aluminum and TiN-coated chicane RFAs. Overall, the agreement is reasonable without any additional tuning of the SEY parameters.

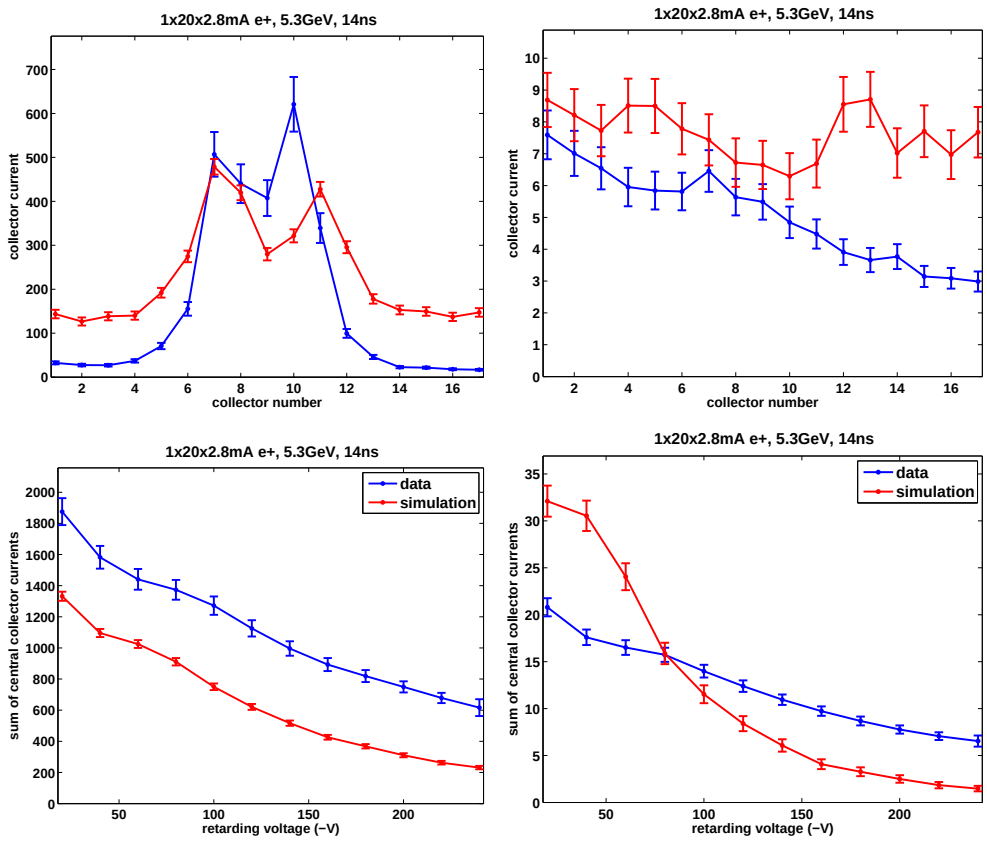

Figure 3.13: Comparison of chicane RFA data and simulation, using best fit parameters for aluminum (left, see Table 2.6), and TiN (right, see Table **??**). The top plots show the total signal across the 17 RFA collectors (with +50 V on the grid); the bottom plots show the signal in the central five collectors vs retarding voltage.

3.5.1 Simulation of Bifurcation

We have also been able to reproduce many of the qualitative phenomena described in Section 3.2. Fig. 3.14 shows a series of simulations done with different beam currents, reproducing the "bifurcation" effect shown in Fig. 3.6. The beam current at which the bifurcation occurs is sensitive to the POSINST parameter `E0epk` (the peak yield energy).

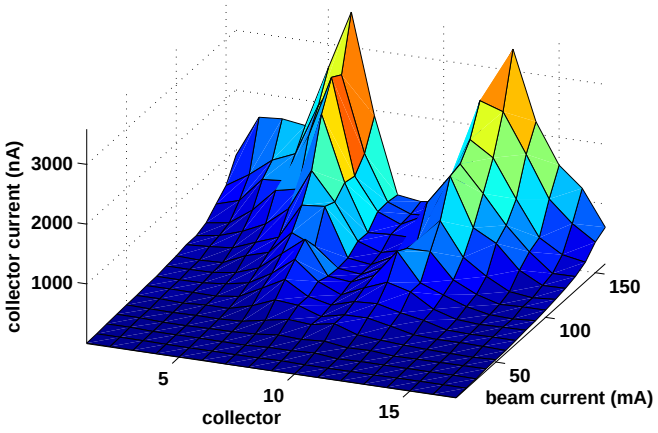

Figure 3.14: Simulation of the bifurcation of peak cloud density: 1x20 e+, 5.3GeV, 14ns. Compare to Fig. 3.6

3.5.2 Simulation of Cyclotron Resonances

A "cyclotron resonance" occurs when the bunch spacing is an integral multiple of the cyclotron period of an electron in a dipole field. Under these conditions, the transverse beam kick to a given electron will always be in the same direction, resulting in a steady increase in the particle's energy, and (usually) a higher secondary electron yield when it hits the vacuum chamber wall. Thus we expect to see a increase in the RFA signal when the chicane field is set to a cyclotron resonance. As discussed in Section 3.2.2, we do indeed observe peaks in the RFA current in the aluminum chicane chamber, but in the TiN-coated chambers we observe dips. Fig. 3.15 shows a simulated magnetic field scan over a cyclotron resonance, in both an aluminum and TiN-coated chamber. Consistent with the data, we observe an increase in the aluminum chamber signal, but a decrease in the TiN chamber signal. Fig. 3.16 provides an explanation- since the additional energy in the resonant electrons comes from transverse beam kicks, these electrons will have a larger cyclotron radius, and thus a lower RFA efficiency (see

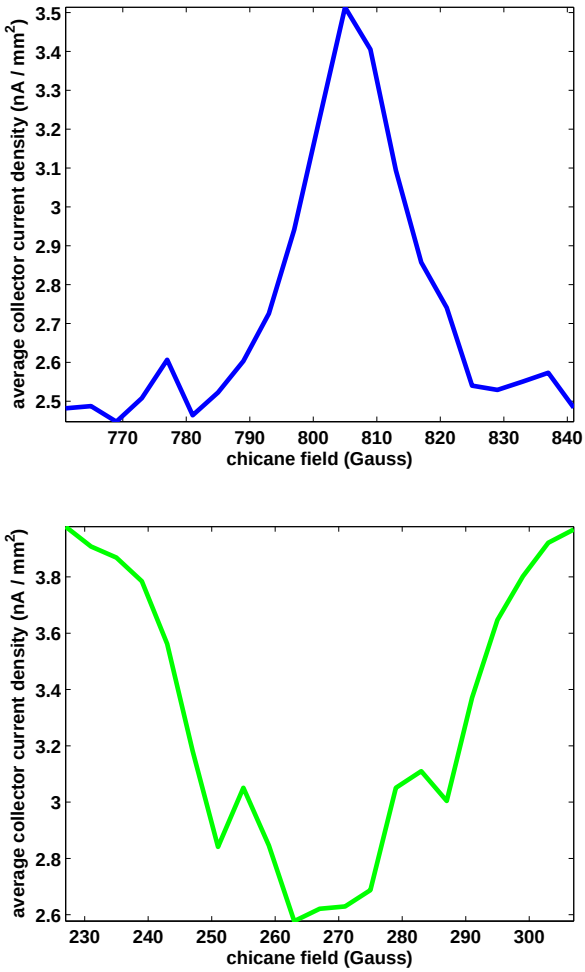

Figure 3.15: Simulation of cyclotron resonances observed by an RFA in aluminum (top) and TiN (bottom) chambers, 1x45x1 mA e+, 4 ns, 5 GeV. Note that, as in Fig. 3.7, the resonance appears as an increase in the aluminum chamber signal, but a decrease in the TiN chamber signal.

Fig. 3.12). Thus there are two competing effects- an increased cloud density due to a higher average SEY, and lower overall detector sensitivity. In the aluminum chamber (where the peak SEY is high) the former effect dominates, while in the coated chamber (where the peak SEY is low) the latter one does. The net result is resonant peaks in the uncoated chamber, and dips in the coated one.

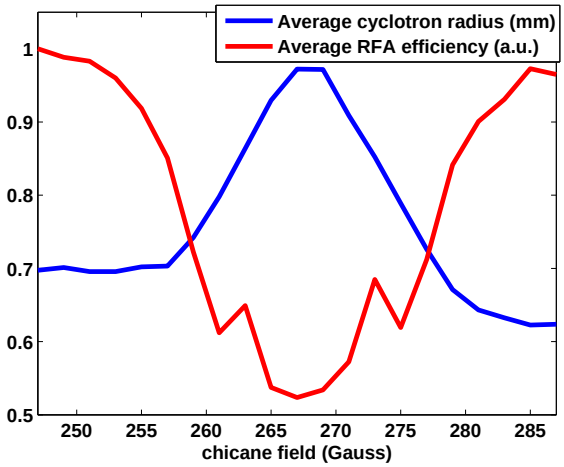

Figure 3.16: Effect of cyclotron resonance on RFA efficiency, 1x45x1 mA e+, 4 ns, 5 GeV. Under the resonant field, the average electron cyclotron radius increases, resulting in a decrease in the average RFA efficiency.

3.5.3 Simulation of Multipacting Resonances

The multipacting resonances described in Section 3.2.3 are also observed in simulation. Fig. 3.17 plots the simulated central collector signal as a function of bunch spacing, for the Al chicane RFA (compare with Fig. 3.8). As in the data, we observe a sharp peak at ~12 ns for a positron beam and a broad one at ~60 ns for both positron and electron beams. These simulations were done with a peak secondary energy spectrum that peaks at an electron emission energy of 1.5 eV, consistent with the analytical model detailed in Section 3.2.3. Changing the secondary energy spectrum changes the location of the peaks, as predicted by the model.

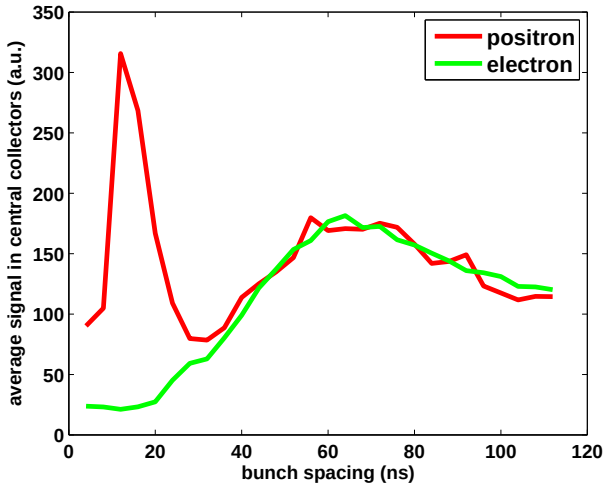

Figure 3.17: Simulation of the multipacting resonances: 1x20x3.5 mA, 5.3GeV. Compare to Fig. 3.8

3.6 Summary

Data taken with RFAs in a dipole field have revealed many interesting phenomena, including bifurcation of the central peak, multipacting resonances, and cyclotron resonances. Although the one dimensional nature of the electron dynamics in a dipole field makes quantitative analysis of the data difficult, we have been able to qualitatively reproduce many of these observations with simulation, reinforcing our understanding of them.

CHAPTER 4

QUADRUPOLE RFA STUDIES

Although only one quadrupole in CESR has been instrumented with an RFA, it has provided a wealth of useful information. Of particular interest is the possibility of long term cloud trapping in the quad.

4.1 Quadrupole Instrumentation

Thin-style RFAs were implemented in beam pipes in a quadrupole magnet in CESR, in the L3 experimental region (see Figure 1.7). The design of the quadrupole RFA beam pipe is illustrated in Figure 4.1. The structure of the RFA consists of high-transparency gold-plated copper meshes nested in PEEK frames and a segmented collector made of flexible circuit, similar to the RFA designs used in the CESR dipole and wigglers. Many (1740) small holes (0.75 mm in diameter) were drilled through the beam pipe to allow electrons to reach the RFA, while filtering out beam-induced RF. These 1740 holes are grouped into 12 angular segments, matching the 12 RFA collector elements on the flexible circuit. The angular coverage and resolution of the RFA is shown in Figure 4.2.

4.2 Measurements

A typical quadrupole RFA measurement is shown in Fig. 4.3. We find that the collector that is lined up with the quad pole tip (no. 10) sees a large amount of current, while the rest of the collectors see relatively little. This suggests that the majority of the cloud in the quad is streaming between two pole tips, a fact that

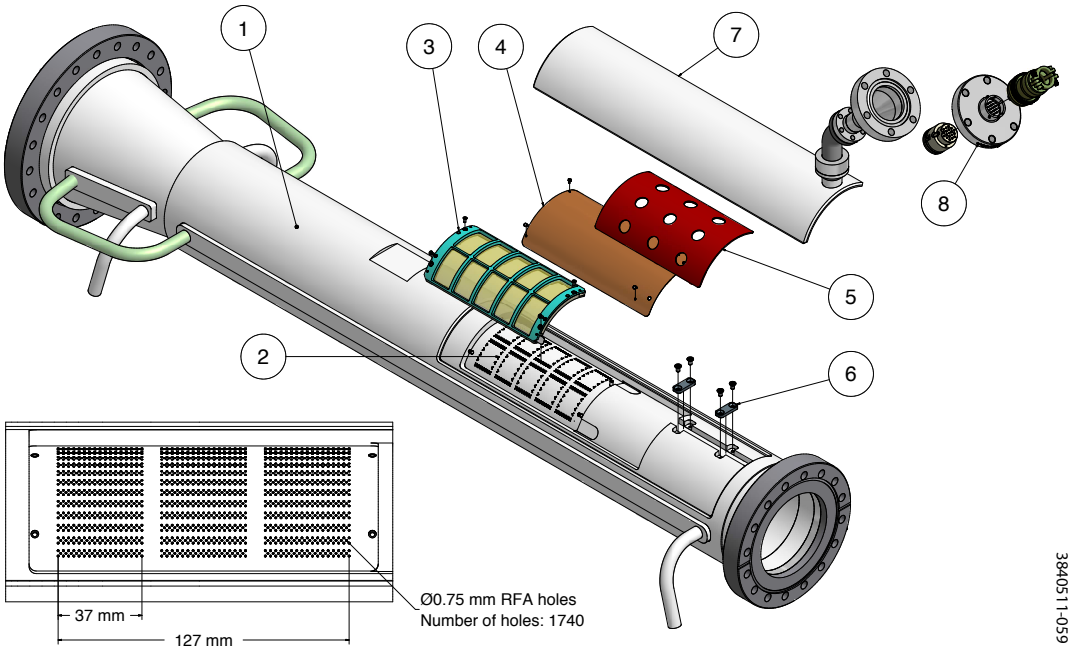

Figure 4.1: Exploded view of the structure of the RFA within a CESR quadrupole beam pipe. The major components of the RFA beam pipe include: (1) Aluminum beam pipe with cooling channels; (2) RFA housing and wiring channels; (3) Retarding grids, consisting of high-transparency gold-coated meshes nested in PEEK frames; (4) RFA collector flexible circuit; (5) Stainless steel backing plate; (6) Wire clamps; (7) RFA vacuum cover with connection port; (8) 19-pin electric feedthrough for RFA connector

is clearly and consistently seen in simulations (Section 4.4).

4.2.1 Bunch Spacing Study

One potential side effect of the cloud mirroring between the quad pole tips is that it may become trapped for a long time. As seen in Fig. 4.4, for a positron beam we do not observe a strong dependence on bunch spacing, though there does seem to be a modest enhancement around 14ns. The data for an electron beam is even more surprising, actually showing a monotonic increase with bunch spacing. Both of these measurements are consistent with a timescale for

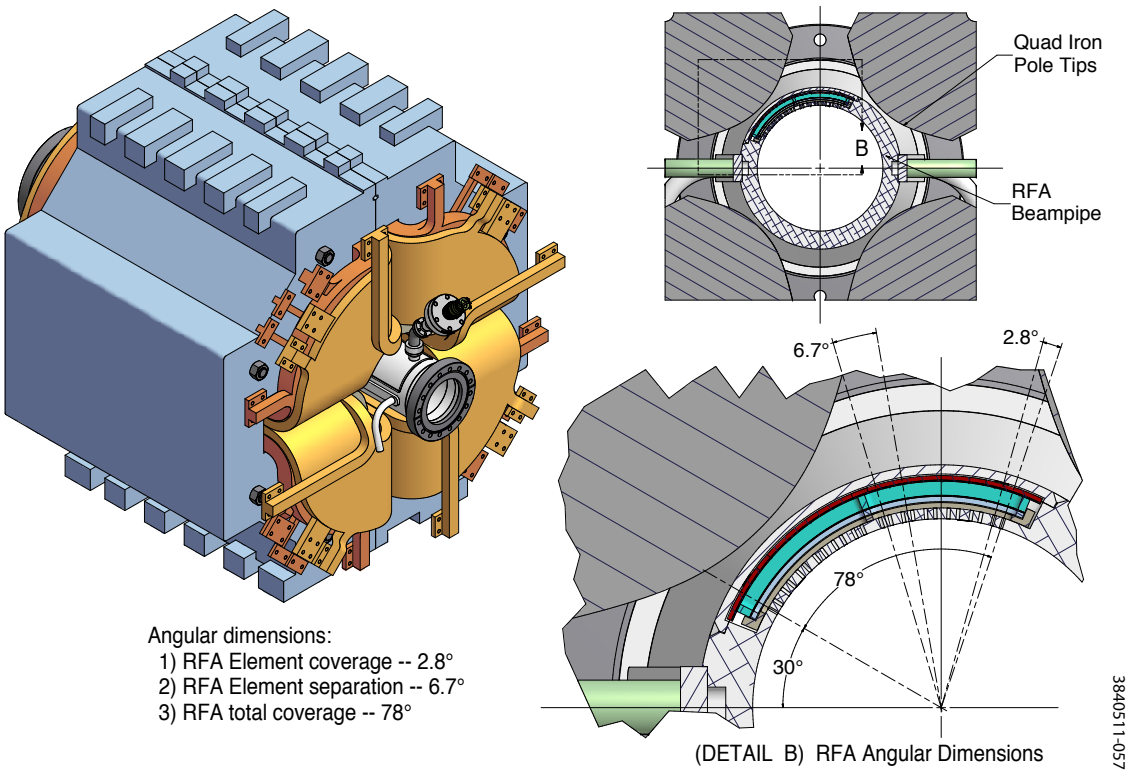

Figure 4.2: The RFA beam pipe in the Q48W quad (left). The RFA angular coverage (right).

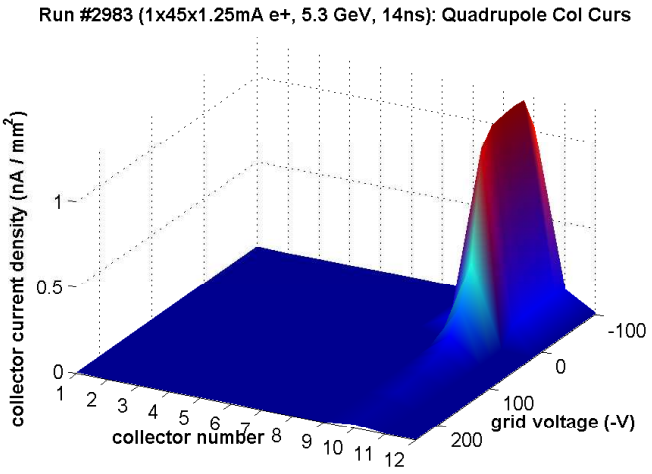

Figure 4.3: Quadrupole RFA voltage scan: 1x45x1.25mA e+, 5.3GeV, 14ns

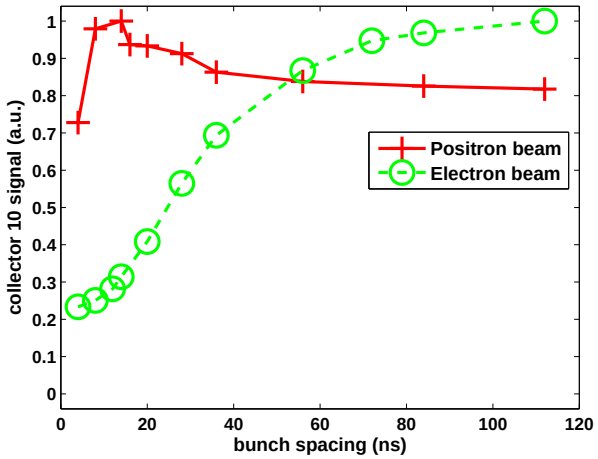

Figure 4.4: Signal in a quadrupole RFA as a function of bunch spacing, for the same beam conditions as in Fig. 3.8. The collector which is in line with the quad pole tip is plotted.

cloud development in the quad that is much longer than 100ns.

4.3 Mitigation comparison

Fig. 4.5 shows a comparison of a bare Aluminum (both processed and unprocessed) quadrupole chamber with the TiN-coated chamber that has replaced it. In this comparison only collector 10 is being plotted. The signal in the TiN chamber was found to be reduced by well over an order of magnitude.

4.4 Simulations

Some preliminary simulations have been done for the quadrupole RFA installed in CESR. The simulations reproduce the behavior described above, where the majority of the signal is concentrated in one collector (Fig. 4.6). Interestingly,

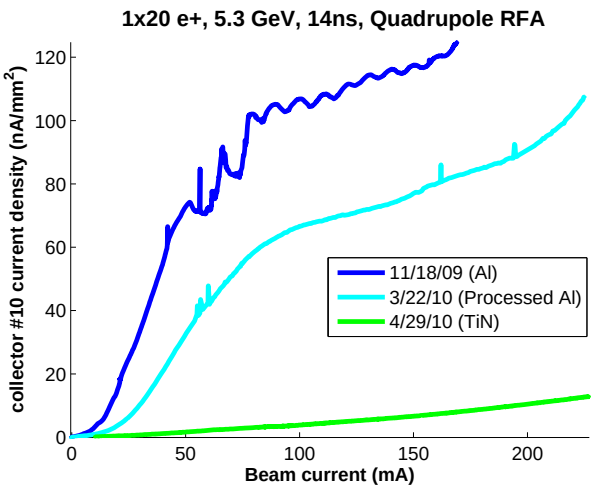

Figure 4.5: Quadrupole mitigation comparison, 1x20 e+, 5.3GeV, 14ns

they also give some indirect evidence that the cloud can become trapped in the quadrupole for long periods of time.

Fig 4.7 shows the signal in collector no. 10 for a voltage scan done with a 45 bunch train of positrons at 1mA/bunch. Also plotted are simulations done in ECLOUD [51] of these conditions. If one does a simulation for only one beam revolution period (2.56μs), the simulated signal is too low at all retarding voltages by over an order of magnitude. However, if one continues the simulation for multiple turns, one finds that the data and simulation start to get closer. By 19 turns, they are in very good agreement at high voltage, and within a factor of 2 at low voltage. This implies that the cloud builds up over several turns, and that the RFA is sensitive to this slow buildup.

4.5 Summary

Measurements done with a quadrupole RFA imply that the majority of the cloud streams between the pole tips. TiN coating does seem to be effective in mitigat-

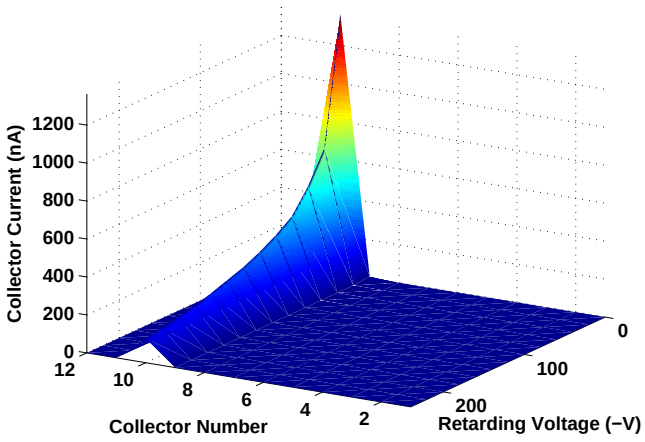

Figure 4.6: Quadrupole RFA simulation: 1x45x1 mA e+, 5.3 GeV, 14ns

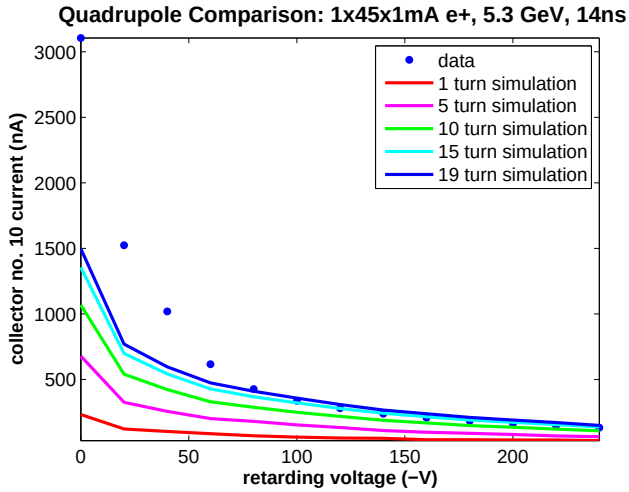

Figure 4.7: Quadrupole RFA simulation showing long term cloud buildup: 45 bunches, 1mA/bunch, e+, 5.3 GeV, 14ns

ing cloud buildup in the quad. We also have evidence, from both data and simulations, that the decay time of the cloud in a quadrupole field is much longer than in a drift or dipole.

CHAPTER 5

WIGGLER RFA STUDIES

Wigglers are an important component of next generation lepton colliders, as they greatly increase the radiation damping of the beam [2]. However, the high rate of photon production in wigglers, combined with the complex three dimensional nature of their magnetic fields, makes electron cloud buildup inside them a serious concern [15]. To address this question at CESR-TA , superconducting wigglers deployed in the L0 straight section (and later the 19E arc) were instrumented with RFAs.

5.1 Wiggler Instrumentation

A more detailed description of the design and construction of the superconducting wigglers and their RFAs can be found in [1]; here we present only a brief overview.

In 2008, the L0 straight section of CESR was completely reconfigured for the CesrTA program. The CLEO detector was removed, and six superconducting wigglers were installed (Section 1.2.1). The wigglers are 8-pole super-ferric magnets with main period of 40 cm and trimming end poles, and were typically operated with a peak transverse field of 1.9 T, closely matching the ILC DR wiggler requirements.

Three of these wigglers were equipped with RFAs (Fig. 5.1). Each instrumented wiggler has three RFAs: one in the center of a wiggler pole (where the field is mostly transverse), one in between poles (where the field is mostly longitudinal), and one in an intermediate region (where the field is essentially 3D, see

Fig. 5.2). These RFAs had to be specially designed to fit in the extremely narrow aperture of the wiggler magnet. They each have one retarding grid and twelve collectors. There are 240 small holes in the beam pipe to allow electrons to enter the RFA; these holes have a diameter of 0.75 mm (= 1/3 of wall thickness) to reduce the EMI into the RFA signals (Fig. 5.3).

Two generations of metallic meshes were used as the retarding grids. The first generation was made of photo-chemically etched 0.15 mm-thick stainless steel (SST) mesh, with an optical transparency of approximately 38%. To reduce the secondary emission from the grid, the SST meshes were coated with approximately 0.3 μm of gold. However, as described in section 5.4, these low efficiency grids lead to a significant interaction between the electron cloud and the RFA, complicating the interpretation of the measurements. Therefore the second generation grids were electroformed copper meshes, consisting of 15 μm wide and 13 μm thick copper wires with spacing 0.34 mm in both transverse directions and an optical transparency of approximately 92%. The electroformed copper meshes were also coated with gold (approximately 0.3 μm in thickness) via electroplating to reduce secondary electron emission. The collectors consist of flexible copper-clad/Kapton circuit laid on top of the ceramic frames of the grids and precisely positioned with ceramic head-pins.

Over the course of the CesrTA program, four different RFA instrumented wigglers have been constructed, each incorporating a different electron cloud mitigation mechanism. The fist two chambers, installed in fall 2008, were bare Cu and TiN coated Cu. In summer 2009, a chamber with triangular grooves on the bottom was constructed. Some of the electrons produced in the grooves will spiral into them as they move into the center of the chamber, resulting in

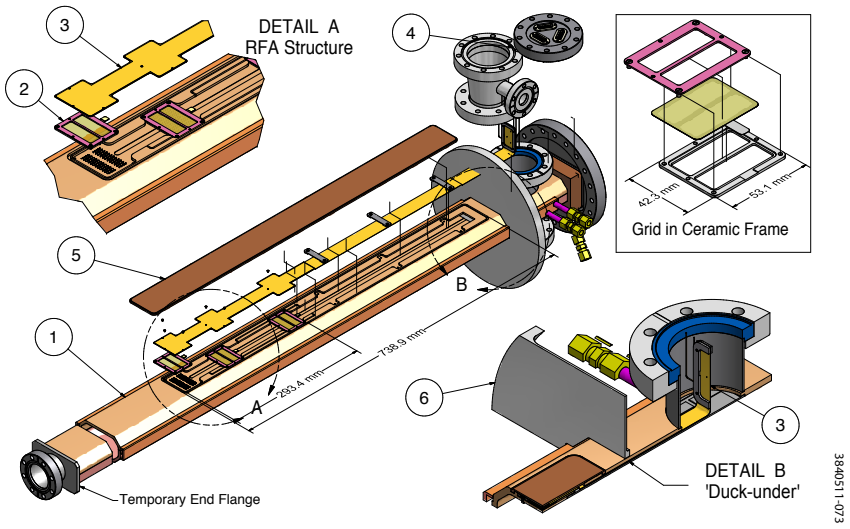

Figure 5.1: Exploded View of a SCW RFA beam pipe Assembly. The key components are: (1) beam pipe top half, housing the RFAs; (2) RFA grids (see upper right inset); (3) RFA collector; (4) RFA connection port; (5) RFA vacuum cover. The 'duck-under' channel, through which the kapton flexible circuit is fed after all heavy welding is complete, is shown in detail B.

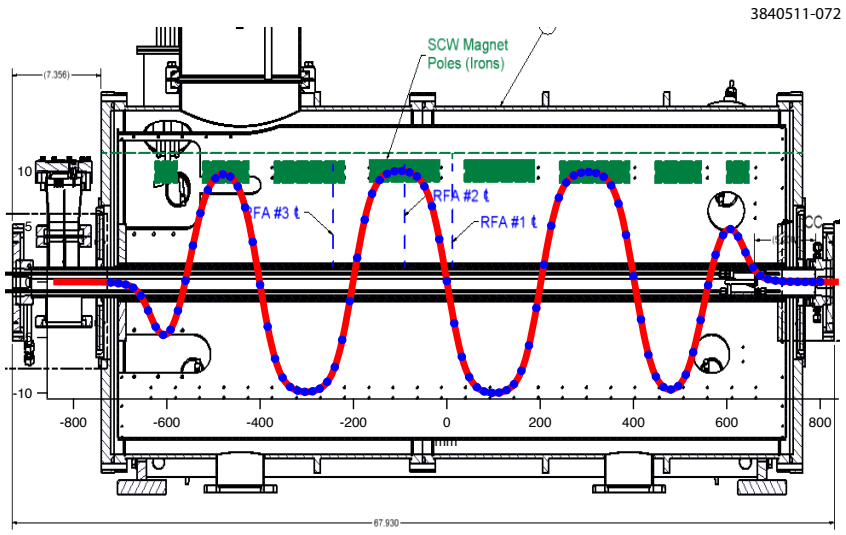

Figure 5.2: Three RFAs are built into each SCW RFA beam pipe. A plot of the B-field along the wiggler (red line with blue dots) is superimposed on the drawing of the wiggler. The RFAs are located at three strategic B-field locations, as shown.

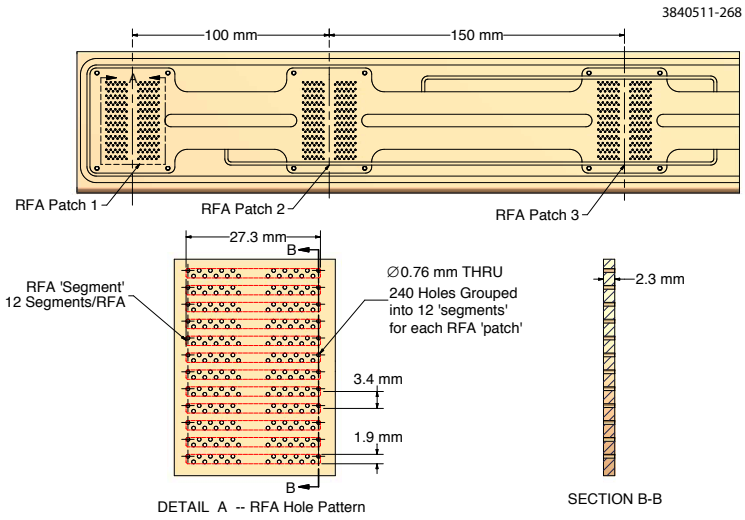

Figure 5.3: Small holes are drilled through top beam pipe to allow electrons in the beam pipe drift into RFAs. There are 240 holes for each RFA, and they are grouped into 12 segments to sample transverse EC density distribution.

an effective reduction of the primary and secondary electron yield. The grooves have 2mm depth and 20° angle.

The fourth cloud mitigation technique we have tested in a wiggler is a clearing electrode, which simply uses a DC electric field to pull electrons toward the chamber wall. The geometry of the clearing electrode is a thin stripline [46], which consists of an alumina ceramic layer on copper surface (of approx. 0.2 mm in thickness) as an insulator and a thin layer of tungsten on the ceramic surface (of approx. 0.1 mm in thickness) as the electrode. These two layers were deposited via a thermal spray technique and were tightly bonded to the copper chamber. The electrode was typically operated at 400V for our measurements.

These chambers have been rotated through the three available locations in L0, to directly compare the effectiveness of each mitigation in identical photon and beam conditions. In addition, one of the wigglers was moved to a location in the 19E arc of CESR, to study the response of the RFA in a more typical

Table 5.1: Locations of instrumented wiggler chambers

Dates	1W Loc	2WA Loc	2WB Loc
11/08 - 6/09	-	Cu	TiN
7/09 - 3/10	Cu	TiN	Grooves
4/10 - 12/10	Cu	TiN	Electrode
1/11 - present	Cu	Grooves+TiN	Electrode

photon environment. Table 5.1 gives the location of each instrumented wiggler throughout the CesrTA program. Note that in January 2011, the grooved chamber was coated with TiN, and the smooth TiN chamber was moved to 19E.

5.2 Measurements

Fig. 5.4 shows a typical voltage scan done in the center pole RFA of a Cu wiggler chamber, for a 45 bunch train of positrons at 1.25mA/bunch, 14ns spacing, and 2.1 GeV. The signal is fairly constant across all the collectors at low retarding voltage, but does become peaked at the center at high energy. There is also an anomalous spike in current at low (but nonzero) retarding voltage; this is due to a resonance between the bunch spacing and retarding voltage (see Section 5.4). A measurement done in the intermediate field RFA under the same beam conditions is shown in Fig. 5.5. It contains the spike at low retarding voltage seen in the center pole detector, and also a broader peak at higher voltage. Due to the complex 3 dimensional nature of the magnetic field at this location, this measurement is difficult to interpret.

Fig. 5.6 shows an example voltage scan from the grooved chamber. Because the spacing of the collectors is comparable to the distance between peaks of the grooved surface, we observe alternating dips and peaks in the collector currents.

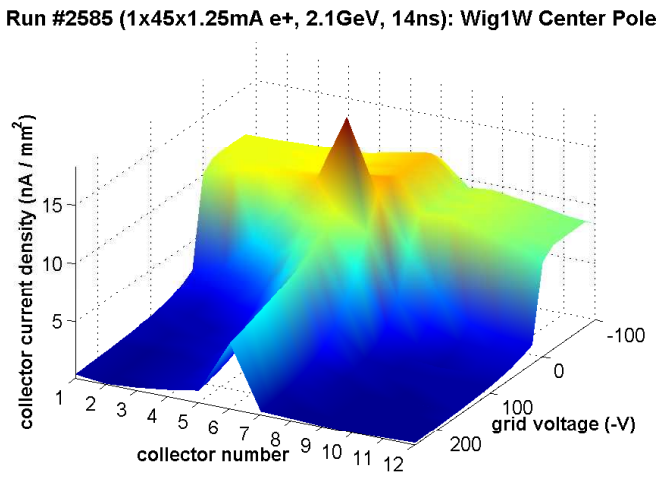

Figure 5.4: Cu wiggler pole center RFA measurement: 1x45x1.25mA e+, 2.1GeV, 14ns

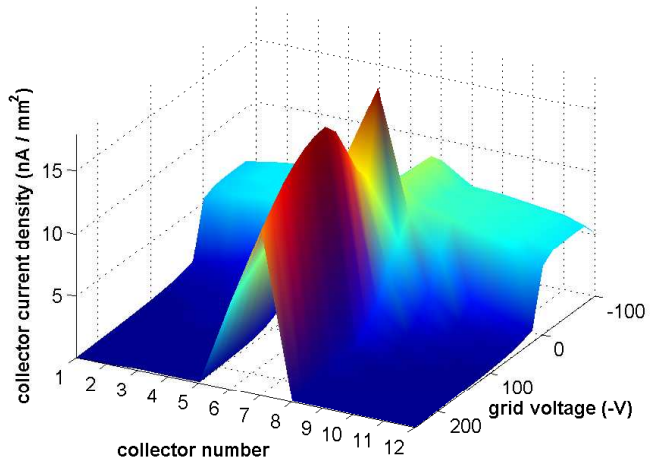

Figure 5.5: Cu wiggler intermediate field RFA measurement: 1x45x1.25mA e+, 2.1GeV, 14ns

During normal wiggler operation, no signal was ever observed in the RFAs located in the longitudinal field region. This means that no electrons in the cloud had sufficient transverse energy to cross the longitudinal field lines and reach the vacuum chamber wall. However, simulations have indicated that cloud could be trapped near the beam at these locations [15].

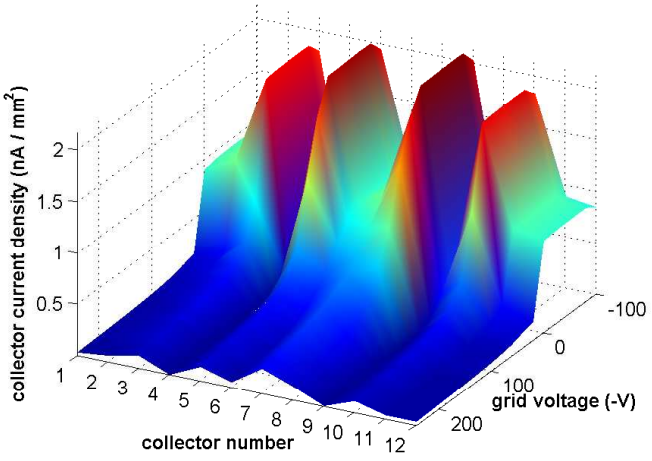

Figure 5.6: Grooved wiggler pole center RFA measurement: 1x45x1.25mA e+, 2.1GeV, 14ns

5.2.1 19E Comparison

In 2011, the TiN coated wiggler was moved from the L0 straight to the Q19E arc, to take wiggler RFA measurements in a more typical photon environment. We observed signals that looked qualitatively similar (though smaller, due to the difference in photon flux) to the measurements taken in L0. Fig. 5.7 shows an example comparison.

5.2.2 Clearing Electrode Scan

Fig. 5.8 shows the result of varying the clearing electrode voltage on the center pole RFA. The signal is reduced by an order of magnitude with only +50V on the electrode, and continues to decrease with higher voltage. Using a negative voltage actually slightly increases the RFA signal, because the field is pushing electrons into the RFA.

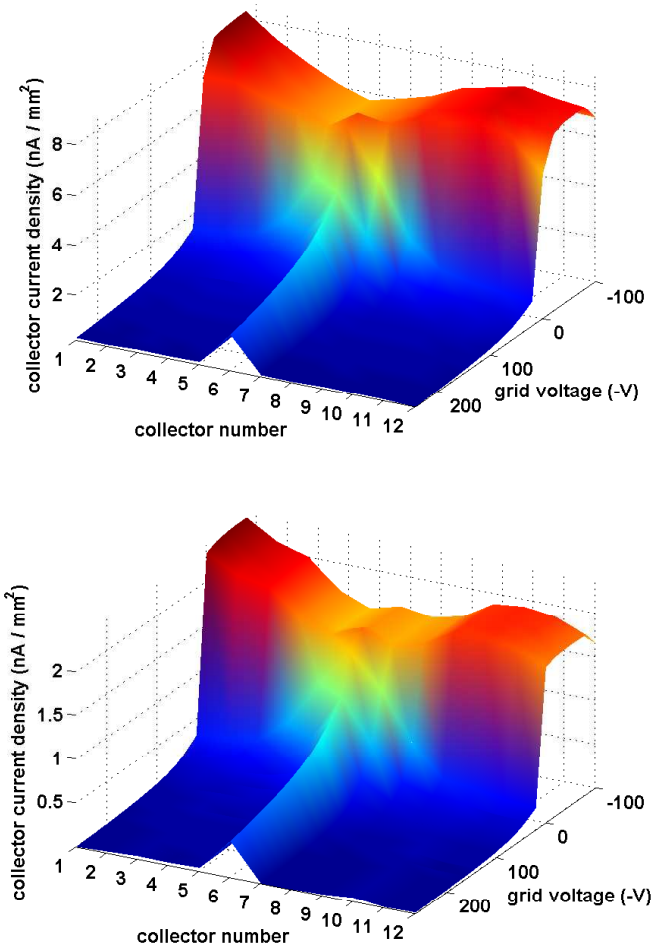

Figure 5.7: Comparison of wiggler pole center measurements in L0 (top) and Q19E (bottom): 1x45x.75 mA e+, 14 ns, 2.1 GeV

5.2.3 Wiggler Ramp Studies

Very little dipole radiation is expected to reach the downstream vacuum chambers in the L0 straight, but they will be illuminated by radiation from the wigglers. Therefore, by varying the field in the wiggler magnets, we can vary the number of photons striking the wall at a given point along the straight. This will also vary the number of photoelectrons produced there, so electron cloud diagnostic devices located in L0 can provide an indirect measurement of the

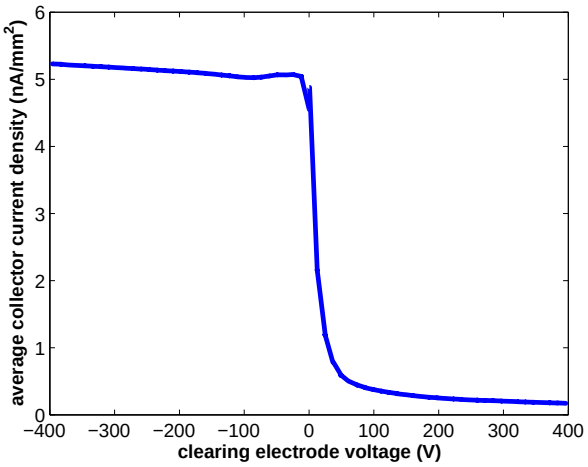

Figure 5.8: Clearing electrode scan: 1x45x1mA e+, 2.1GeV, 14ns

properties of the wiggler photons.

Fig. 5.9 shows the signal in three center-pole wiggler RFAs as a function of wiggler field strength. We observe a "turn on" of the signal in each detector at a specific wiggler field value. Note that the detectors that are further downstream (i.e. those with a higher s value) turn on first. This is because as the wiggler field is increased, the radiation fan becomes wider. The farther downstream a detector is, the less wide the fan must be for photons to hit at that location. This measurement can help us understand the scattering of photons in L0, since only photoelectrons produced on the top or bottom of the beam pipe can initiate the build-up of the part of the cloud detected by the RFA.

With the wiggler fields at nominal values, essentially no signal is observed in longitudinal field detectors, because there are no electrons with sufficient energy to cross the field lines. Fig. 5.10 shows the signal in a longitudinal field RFA (in the uncoated Copper wiggler), as a function of magnetic field strength. The signal is effectively gone by 1000 Gauss, well below the 1.9T full field value.

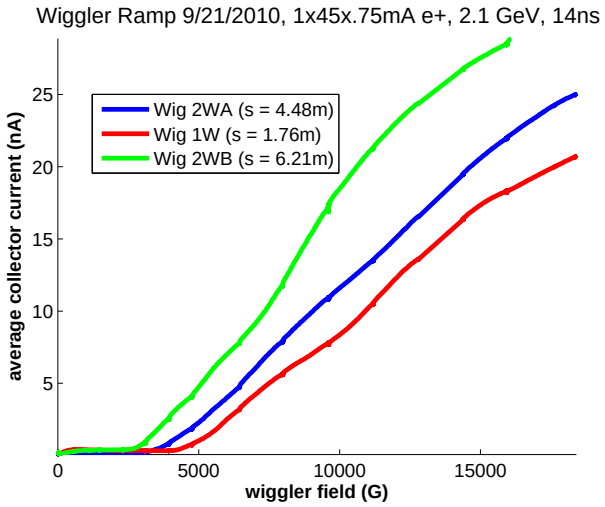

Figure 5.9: Wiggler ramp measurement: 1x45x.75mA e+, 2.1GeV, 14ns

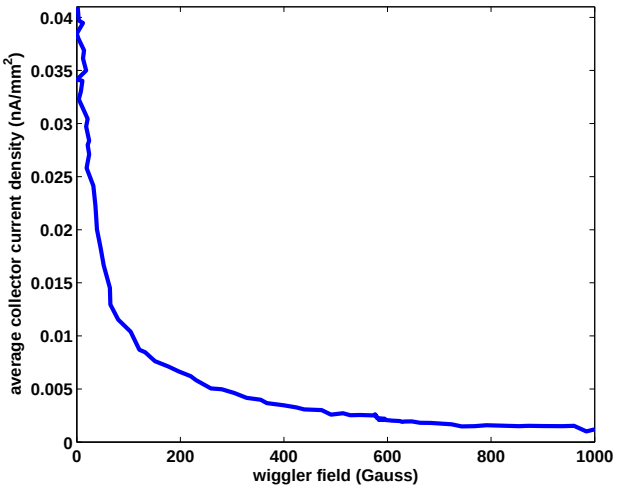

Figure 5.10: Wiggler ramp measurement in longitudinal field region: 1x45x.75mA e+, 2.1GeV, 14ns

5.3 Mitigation comparisons

As described above, cycling the location of the different wigglers has allowed us to compare the RFA response with different mitigation techniques at the same longitudinal position in the ring. Fig. 5.11 compares the average collector current (in the center pole RFA) vs beam current for different mitigation schemes,

at both the 2WA and 2WB locations. These locations have slightly different photon fluxes, but as the TiN coated chamber has been installed in both, it can be used (roughly) as a reference. Note that TiN coating by itself does not appear to lead to a reduction in the wiggler RFA current relative to bare copper. Grooves do lead to an improvement, and TiN coated grooves are better still. The chamber instrumented with a clearing electrode shows the smallest signal by a wide margin, improving on TiN by approximately a factor of 50. The electrode was set to 400V for this measurement.

5.4 Wiggler RFA modeling

Detailed analysis of the wiggler RFA data is complicated, because of the interaction between the cloud and the RFA itself. For an example of such an interaction, see Fig. 5.12. It shows a voltage scan done with an RFA in the center pole of a wiggler (approximated by a 1.9 T dipole field). Here one can see a clear enhancement in the signal at low (but nonzero) retarding voltage. Since the RFA should simply be collecting all electrons with an energy more than the magnitude of the retarding voltage, the signal should be a monotonically decreasing function of the voltage. So the RFA is not behaving simply as a passive monitor. Furthermore, the spike in collector current is accompanied by a corresponding dip in the grid current, suggesting that the grid is the source of the extra collector current.

This spurious signal comes from a resonance between the bunch spacing and retarding voltage. To understand this, consider an electron which collides with the retarding grid and generates a secondary. Because electrons are so strongly

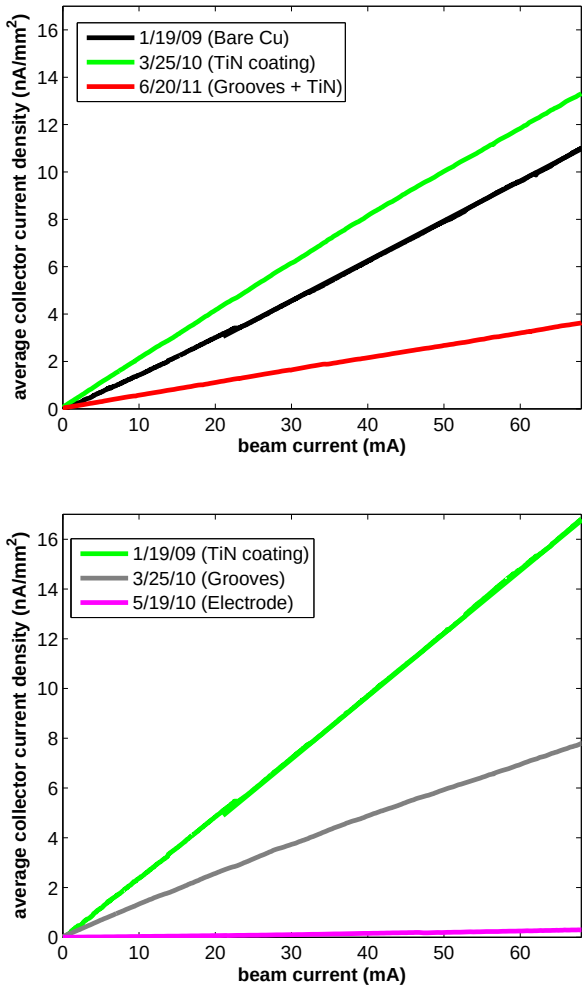

Figure 5.11: Wiggler RFA mitigation comparison: 1x45 e+, 2.1GeV, 14ns. Top: 2WA location, bottom: 2WB location. The 2WB location is further downstream in the wiggler straight, and therefore has a slightly higher photon flux.

pinned to the magnetic field lines in a 1.9T field, this electron is likely to escape through the same beam pipe hole through which it entered. An electron ejected from the grid will gain energy from the retarding field before it re-enters the vacuum chamber. If it is given the right amount of energy, it will be near the center of the vacuum chamber during the next bunch passage, and get a large beam kick, putting it in a position to generate even more secondaries. This process, which we have whimsically dubbed the "trampoline effect", results in

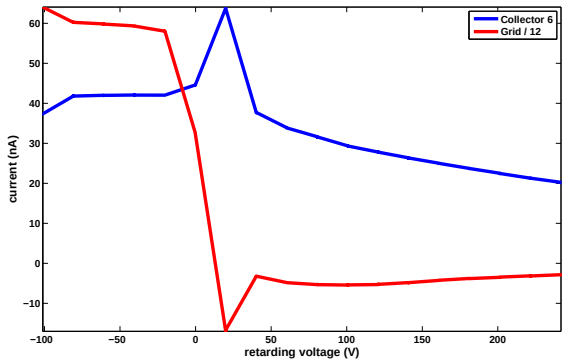

Figure 5.12: Resonant enhancement in wiggler data, 45 bunches, 1.25 mA/bunch, e+, 2.1 GeV, 14 ns. Note that there are 12 collectors, so collector 6 is one of the central ones. Also note that the grid signal is divided by 12.

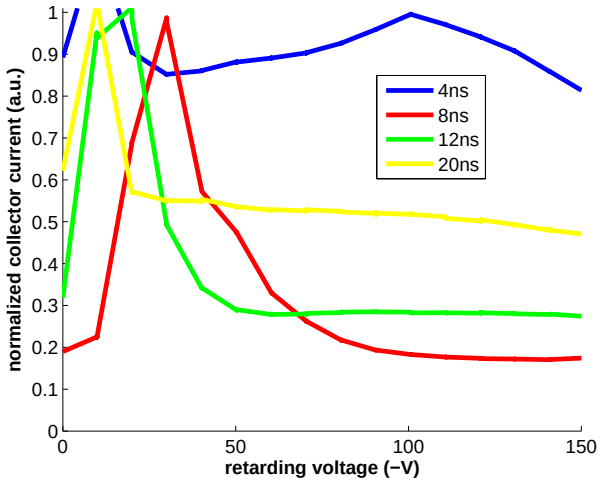

Figure 5.13: Resonant spike location at different bunch spacings, 1x45x1.25 mA e+, 5GeV. Only the signal in the central collector is plotted

a resonance condition for the retarding voltage that is inversely proportional to the square of the bunch spacing, since the shorter the bunch spacing, the more kinetic energy an electron needs to arrive at the beam in time for the next bunch passage [7]. Fig. 5.13 shows that this dependence is (roughly) present in the data, though the low energy spike in the 4ns data is not predicted by this model.

Motivated by these measurements, we have incorporated into POSINST a model of the RFA geared toward reproducing the geometry of the devices installed in the vacuum chambers of the CESR-TA wigglers. The motion of the electrons within the RFA, including the electrostatic force from the retarding field, is tracked using a special add-on routine. The grid is modeled realistically, and secondary electrons can be produced there, with the same secondary yield model used for normal vacuum chamber collisions. The peak secondary electron yield and peak yield energy can be specified separately for the grid.

5.5 Simulations

Because the actual retarding field is included in the wiggler RFA model, the retarding voltage must be specified in the input file, and a separate simulation must be run for each voltage desired. Fig 5.14 shows the result of running this simulation for a series of different retarding voltages, for one set of beam conditions. Notably, the simulation reproduces the resonant enhancement seen in the data, at approximately the same voltage (10V for 14ns spacing), and shows that the extra signal comes from the grid.

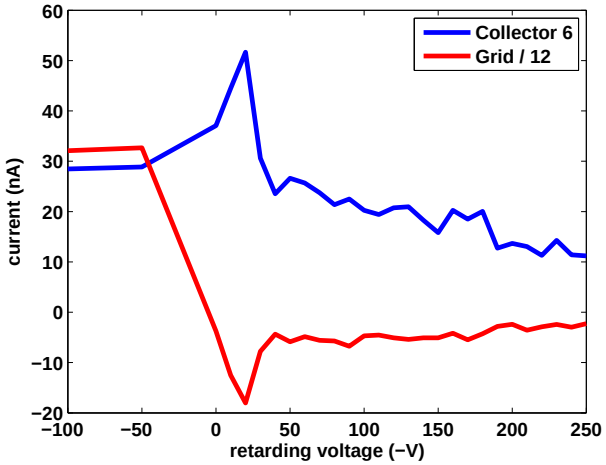

Figure 5.14: POSINST simulation showing resonant enhancement, 1x45x1.2 mA e+, 2.1GeV, 14ns, central collector. Compare to Fig. 5.12.

CHAPTER 6

COMPARISONS WITH OTHER METHODS

As described in Section 1.2.3, several other electron cloud detectors have been employed at CESR-TA . When possible, it is useful to compare these with RFA results, to bolster our confidence in both measurement techniques.

6.1 Shielded Pickup Comparison

RFA and shielded pickup detectors have been deployed in adjacent locations in the 15E and 15W arc sections of CESR (Section 2.1.2). Fig. 6.1 compares the time-averaged signal of the 15W SPU with the central collectors of the 15W RFA. The approximately linear relationship between the signal in the two detectors across a variety of beam conditions implies that their measurements can be directly compared.

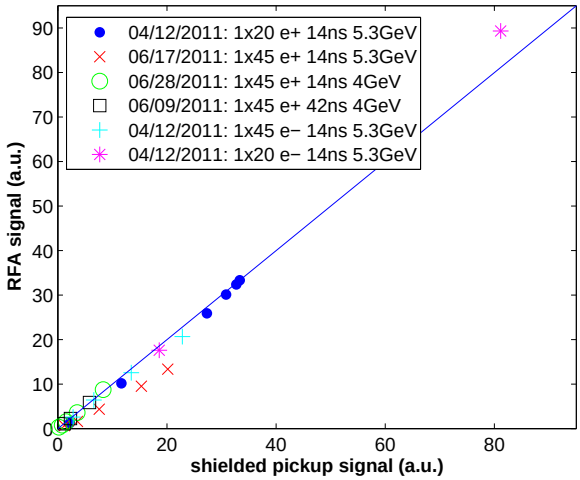

Figure 6.1: Comparison of RFA and SPU measurements, 15W TiN coated chamber. Each point represents a measurement with different beam conditions.

RFA and SPU simulations (see Section 2.5 and [20] respectively) have lead

to many of the same qualitative conclusions. The most significant of these are a very low secondary emission yield for TiN and amorphous carbon coated chambers, and the sensitivity of high current electron beam data to the high energy tail of the photoelectron energy distribution. A more detailed comparison of RFA and SPU data and simulations is an important area of future work.

6.2 TE-Wave Comparisons

The L0 wiggler straight is instrumented with both RFAs and TE-Wave hardware, which provides an opportunity to compare the two methods. Fig. 6.2 shows a wiggler ramp measurement (see Section 5.2.3), during which both RFA and TE-Wave data were taken. RFA data is plotted as solid lines, TE-Wave "transmission" measurements with dashed lines, and TE-Wave "resonant" measurements with dotted lines. Both detectors show the "turn on" behavior described above, and the threshold values of the magnetic field for the two methods are roughly consistent.

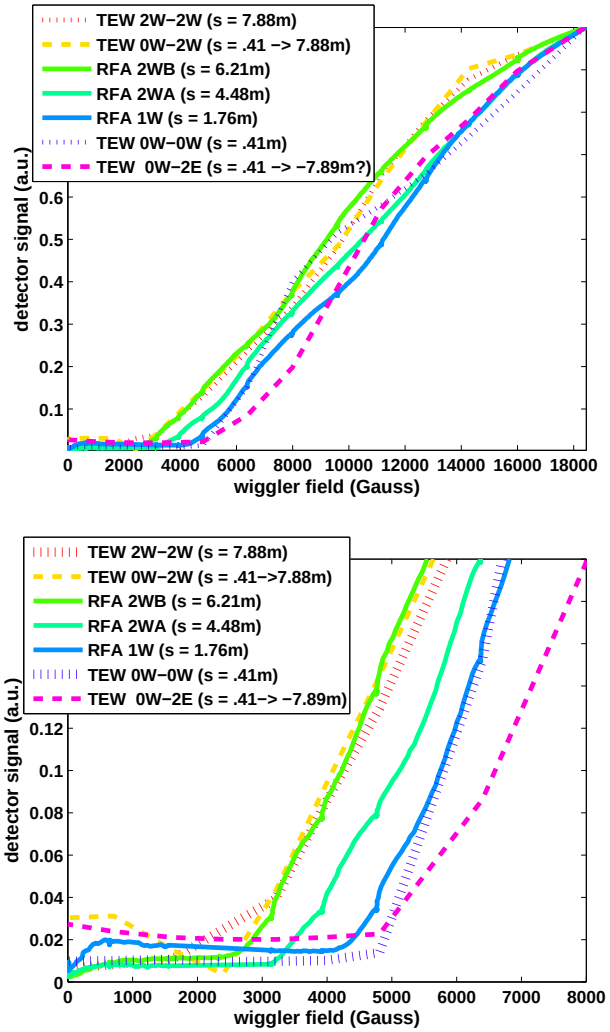

Figure 6.2: RFA/TE-Wave comparison during a wiggler ramp measurement. The bottom plot is zoomed in, to more clearly show the turn-on behavior. Beam conditions are 45 bunches of positrons at .75mA/bunch, 2.1GeV, 14ns spacing. Each of the signals is normalized to 1 at peak wiggler field (1.9T), because it is difficult to quantitatively compare RFA and TE-Wave data.

CHAPTER 7

CONCLUSIONS

Electron cloud is a ubiquitous problem in accelerators, and is often a limiting factor in their operation. It is especially serious for positively charged beams with low emittance, high intensity, and short bunch spacing. These conditions are essential features in many proposed next generation machines, as well as upgrades of existing machines. Therefore it is important to understand the electron cloud, and to mitigate it as far as possible. The CESR-TA program is a large step forward on both fronts. CESR-TA is (among other things) arguably the most extensive investigation of electron cloud in a single machine to date.

7.1 Results/accomplishments

Retarding field analyzers have been installed in drift, dipole, quadrupole, and wiggler field regions around CESR, and a great deal of electron cloud data has been collected with them. Measurements have been taken under a wide variety of beam conditions, which is useful for pinning down the various primary and secondary emission parameters. These data have also been used to directly compare the efficacy of various electron cloud mitigation techniques. To summarize these results:

- Beam pipe coatings (TiN, aC, DLC, and NEG) are effective in drifts, dipoles, and quadrupoles.
- Triangular grooves are effective in dipoles and wigglers.
- A combination of coating and grooves is better than either individually.

- In a wiggler, a clearing electrode is the best option.

Many interesting phenomena have been investigated using RFAs. Among these are:

- Multipacting resonances in drifts and dipoles
- Bifurcation of the peak central density in a dipole
- Long term cloud trapping in a quadrupole
- Cyclotron resonances in a dipole
- Signal threshold behavior as a function of wiggler field

Detailed models of our RFAs have been developed, and integrated into the cloud simulation code POSINST, allowing for analysis on a more fundamental level. In a drift, this has enabled the calculation of best fit simulation parameters, which describe the primary and secondary electron emission characteristics of each material in situ. The fits indicate that TiN and DLC have especially low secondary yields, while aC has the lowest quantum efficiency. Also, with the possible exception of diamond-like carbon, the coatings show mostly stable behavior over the long term.

Quantitative analysis has proved to be more difficult for RFAs in magnetic field regions, due to the complex interactions between the cloud and the detector. Nonetheless, qualitative agreement between data and simulation is readily achieved, and interesting phenomena can be simulated in detail.

The end results of the measurements and analysis presented here include a deeper understanding of the electron cloud, detailed evaluation of different

vacuum chamber materials and cloud mitigations, validation of cloud buildup codes, and input for future machines. Given the ubiquitousness of the electron-cloud effect, our results are directly and immediately applicable to other high-energy or high-intensity storage rings, whether lepton or hadron.

7.2 Future work

It is the opinion of the author that future work on this subject should focus on three areas:

- Further study of long term conditioning in each magnetic field element.
- Incorporation of fully self-consistent models for the dipole and quadrupole RFAs, and systematic fitting of the dipole, quad, and wiggler data.
- Detailed comparison with other measurement techniques (in particular shielded pickups and TE-waves)

APPENDIX A

ADDITIONAL MITIGATION COMPARISONS

BIBLIOGRAPHY

[1] The cesrta electron cloud research program phase i report, sections 2.2 - 2.3. Technical Report CLNS-12-2084, LEPP, Cornell University, Ithaca, NY, October 2012.

[2] Gerald Aarons, Toshinori Abe, Jason Abernathy, et al. International linear collider reference design report. Technical Report ILC-REPORT-2007-001, International Linear Collider, Batavia, IL/Tsukuba, Japan/Hamburg, Germany, August 2007.

[3] L. Boon and K. Harkay. Chamber surface roughness and electron cloud for the advanced photon source superconducting undulator. In *Proceedings of ECLOUD 2012: 5th International Workshop on Electron-Cloud Effects, La Biodola, Elba, Italy*, in press.

[4] Y. Cai, M. Pivi, and M. A. Furman. Buildup of electron cloud in the pep-ii particle accelerator in the presence of a solenoid field and with different bunch pattern. *Phys. Rev. ST Accel. Beams*, 7, February 2004.

[5] J. Calvey, J. A. Crittenden, G. Dugan, S. Greenwald, D. Kreinick, J. A. Livezey, M. A. Palmer, D. Rubin, K. C. Harkay, P. Jain, K. Kanazawa, Y. Suetsugu, C. M. Celata, M. Furman, G. Penn, M. Venturini, M. T. F. Pivi, and L. Wang. Simulations of electron-cloud current density measurements in dipoles, drifts and wigglers at cesrta. In *Proceedings of the 2009 Particle Accelerator Conference, Vancouver, BC*, pages 4628–4630, 2009.

[6] J. R. Calvey, M. G. Billing, J. V. Conway, G. Dugan, S. Greenwald, Y. Li, X. Liu, J. A. Livezey, J. Makita, R. E. Meller, M. A. Palmer, S. Santos, R. M. Schwartz, J. Sikora, C. R. Strohman, S. Calatroni, G. Rumolo, K. Kanazawa, Y. Suetsugu, M. Pivi, and L. Wang. Update on electron cloud mitigation studies at cesr-ta. In *Proceedings of the 2011 International Particle Accelerator Conference, San Sebastián, Spain*, pages 796–798, 2011.

[7] J. R. Calvey, C. M. Celata, J. A. Crittenden, G. F. Dugan, S. Greenwald, Z. Leong, J. Livezey, M. A. Palmer, M. Furman, M. Venturini, and K. Harkay. Cesrta retarding field analyzer modeling results. In *Proceedings of the 2010 International Particle Accelerator Conference, Kyoto, Japan*, pages 1970–1972, 2010.

[8] J. R. Calvey, J. A. Crittenden, G. Dugan, M. A. Palmer, and C. M. Celata. Electron cloud modeling considerations at cesrta. In *Proceedings of the 2009 Particle Accelerator Conference, Vancouver, BC*, pages 3306–3308, 2009.

[9] J. R. Calvey, J. A. Crittenden, G. F. Dugan, J. Makita, M. A. Palmer, W. Hartung, M. Furman, and M. Venturini. Modeling and simulation of retarding field analyzers at cesrta. In *Proceedings of the 2012 International Particle Accelerator Conference, New Orleans, LA*, pages 3138–3140, 2012.

[10] J. R. Calvey, J. A. Crittenden, G. F. Dugan, M. A. Palmer, M. Furman, and K. Harkay. Methods for quantitative interpretation of retarding field analyzer data. In *Proceedings of the 2011 Particle Accelerator Conference, New York, NY*, pages 501–503, 2011.

[11] J. R. Calvey, J. A. Crittenden, G. F. Dugan, M. A. Palmer, and K. Harkay. Methods for quantitative interpretation of retarding field analyzer data. In K. Smolenski, editor, *Proceedings of ECLOUD 2010: 49th ICFA Advanced Beam Dynamics Workshop on Electron Cloud Physics, Ithaca, NY*, number Paper PST03, in press.

[12] J. R. Calvey, Y. Li, J. A. Livezey, J. Makita, R. E. Meller, M. A. Palmer, R. M. Schwartz, C. R. Strohman, K. Harkay, S. Calatroni, G. Rumolo, K. Kanazawa, Y. Suetsugu, M. Pivi, and L. Wang. Cesrta retarding field analyzer measurements in drifts, dipoles, quadrupoles and wigglers. In *Proceedings of the 2010 International Particle Accelerator Conference, Kyoto, Japan*, pages 1973–1975, 2010.

[13] J. R. Calvey, J. Makita, M. A. Palmer, R. M. Schwartz, C. R. Strohman, S. Calatroni, G. Rumolo, K. Kanazawa, Y. Suetsugu, M. Pivi, and L. Wang. Electron cloud mitigation investigations at cesr-ta. In K. Smolenski, editor, *Proceedings of ECLOUD 2010: 49th ICFA Advanced Beam Dynamics Workshop on Electron Cloud Physics, Ithaca, NY*, number Paper MIT01, in press.

[14] J.R. Calvey, G. Dugan, W. Hartung, J.A. Livezey, J. Makita, and M.A. Palmer. Studies of electron cloud growth and mitigation in a field free environment using retarding field analyzers. *Phys. Rev. ST Accel. Beams*.

[15] C. M. Celata. Electron cloud dynamics in the cornell electron storage ring test accelerator wiggler. *Phys. Rev. ST Accel. Beams*, 14, April 2011.

[16] C. M. Celata, Miguel A. Furman, J.-L. Vay, D. P. Grote, J. S. T. Ng, M. T. F. Pivi, and L. F. Wang. Cyclotron resonances in electron cloud dynamics. In *Proceedings of the 2009 Particle Accelerator Conference, Vancouver, BC*, pages 1807–1811, 2009.

[17] R. Cimino, I. R. Collins, and V. Baglin. Vuv photoemission studies of candi-

date large hadron collider vacuum chamber materials. *Phys. Rev. ST Accel. Beams*, 2, June 1999.

[18] R. Cimino, M. Commisso, D. R. Grosso, T. Demma, V. Baglin, R. Flammini, and R. Larciprete. Nature of the decrease of the secondary-electron yield by electron bombardment and its energy dependence. *Phys. Rev. Lett.*, 109, August 2012.

[19] J. A. Crittenden, Y. Li, X. Liu, M. A. Palmer, J. P. Sikora, S. Calatroni, and G. Rumolo. Electron cloud modeling results for time-resolved shielded pickup measurements at cesrta. In *Proceedings of the 2011 Particle Accelerator Conference, New York, NY*, pages 1752–1754, 2011.

[20] J. A. Crittenden and J. P. Sikora. Electron cloud buildup characterization using shielded pickup measurements and custom modeling code at cesrta. In *Proceedings of ECLOUD 2012: 5th International Workshop on Electron-Cloud Effects, La Biodola, Elba, Italy*, in press.

[21] O. Domnguez, K. Li, G. Arduini, E. Metral, G. Rumolo, and F. Zimmermann. First electron-cloud studies at the large hadron collider. *Phys. Rev. ST Accel. Beams*, 16, January 2013.

[22] Vadim Dudnikov. Some features of transverse instability of partly compensated proton beams. In P. Lucas and S. Webber, editors, *Proceedings of the 2001 Particle Accelerator Conference, Chicago, IL*, pages 1892–1894, 2001.

[23] G. Dugan and D. Sagan. Synrad3d photon propagation and scattering simulation. In K. Smolenski, editor, *Proceedings of ECLOUD 2010: 49th ICFA Advanced Beam Dynamics Workshop on Electron Cloud Physics, Ithaca, NY*, in press.

[24] N. Eddy, J. Crisp, I. Kourbanis, K. Seiya, B. Zwaska, and S. De Santis. Measurement of electron cloud development in the fermilab main injector using microwave transmission. In *Proceedings of the 2009 Particle Accelerator Conference, Vancouver, BC*, pages 1967–1969, 2009.

[25] M. A. Furman, M. Pivi, K. C. Harkay, and R. A. Rosenberg. Electron-cloud measurements and simulations for the aps. In P. Lucas and S. Webber, editors, *Proceedings of the 2001 Particle Accelerator Conference, Chicago, IL*, pages 679–681, 2001.

[26] M. A. Furman and M. T. F. Pivi. Probabilistic model for the simulation of secondary electron emission. *Phys. Rev. ST Accel. Beams*, 5, December 2002.

[27] M.A. Furman. Electron cloud effects in accelerators. In *Proceedings of ECLOUD 2012: 5th International Workshop on Electron-Cloud Effects, La Biodola, Elba, Italy*, in press.

[28] Miguel A. Furman. The electron-cloud effect in the arcs of the lhc. Technical Report LHC Project Report 180/LBNL-41482/CBP Note 247, CERN, Geneva, Switzerland, May 1998.

[29] Miguel A. Furman and Glen R. Lambertson. The electron-cloud instability in the arcs of the pep-ii positron ring. In Yong Ho Chin, editor, *Proceedings of MBI97: International Workshop on Multibunch Instabilities in Future Electron and Positron Accelerators, Tsukuba, Japan, 1997*, number KEK Proceedings 97-17, page 170, 1997.

[30] O. Gröbner. Bunch induced multipactoring. In Yu. M. Ado, A. G. Afonin, V. I. Gridasov, A. F. Dunaitsev, E. A. Mjae, and A. A. Naumov, editors, *Proceedings of the X International Conference on High Energy Accelerators, Protvino, USSR, 1977*, pages 277–282, 1977.

[31] K. C. Harkay, L. Loiacono, and R. A. Rosenberg. Studies of a generalized beam-induced multipacting resonance condition. In Joe Chew, Peter Lucas, and Sara Webber, editors, *Proceedings of the 2003 Particle Accelerator Conference, Portland, OR*, pages 3183–3185, 2003.

[32] S. A. Heifets. Study of an instability of the pep-ii positron beam (ohmi effect and multipactoring). In Yong Ho Chin, editor, *Proceedings of the International Workshop on Collective Effects and Impedance for B-Factories: CEIBA95, Tsukuba, Japan*, number KEK Proceedings 96-6, 1995.

[33] M. Izawa, Y. Sato, and T. Toyomasu. The vertical instability in a positron bunched beam. *Phys. Rev. Lett.*, 74:5044–5047, June 1995.

[34] K. Kanazawa, H. Hukuma, H. Hisamatsu, and Y. Suetsugu. Measurement of the electron cloud density around the beam. In C. Horak, editor, *Proceedings of the 2005 Particle Accelerator Conference, Knoxville, TN*, pages 1054–1056, 2005.

[35] S. Kato and M. Nishiwaki. E-cloud activity of dlc and tin coated chambers at kekb positron ring. In K. Smolenski, editor, *Proceedings of ECLOUD 2010: 49th ICFA Advanced Beam Dynamics Workshop on Electron Cloud Physics, Ithaca, NY*, number Paper MIT00, in press.

[36] J. Kim, D. Asner, J. Conway, S. Greenwald, Y. Li, V. Medjidzade, T. Moore, M. Palmer, and C. Strohman. In situ sey measurements at cesrta. In K. Smolenski, editor, *Proceedings of ECLOUD 2010: 49th ICFA Advanced Beam Dynamics Workshop on Electron Cloud Physics, Ithaca, NY*, in press.

[37] D. L. Kreinick, J. A. Crittenden, G. Dugan, M. A. Palmer, G. Ramirez, R. L. Holtzapple, M. Randazzo, M. A. Furman, and M. Venturini. Application of coherent tune shift measurements to the characterization of electron cloud growth. In *Proceedings of the 2011 Particle Accelerator Conference, New York, NY*, pages 1680–1682, 2011.

[38] F. Le Pimpec, R. E. Kirby, F. King, and M. Pivi. Properties of tin and tizrv thin film as a remedy against electron cloud. *Nucl. Instrum. Methods Phys. Res.*, A551:187–199, July 2005.

[39] Kazuhito Ohmi. Beam-photoelectron interactions in positron storage rings. *Phys. Rev. Lett.*, 75:1526–1529, August 1995.

[40] M. A. Palmer, M. G. Billing, J. R. Calvey, G. W. Codner, S. Greenwald, Y. Li, X. Liu, J. A. Livezey, R. E. Meller, R. M. Schwartz, J. P. Sikora, C. R. Strohman, W. S. Whitney, and T. Wilksen. Design, implementation and first results of retarding field analyzers developed for the cesrta program. In *Proceedings of the 2009 Particle Accelerator Conference, Vancouver, BC*, pages 3510–3512, 2009.

[41] M. T. F. Pivi, J. S. T. Ng, F. Cooper, D. Kharakh, F. King, R. E. Kirby, B. Kuekan, C. M. Spencer, T. O. Raubenheimer, and L. F. Wang. Observation of magnetic resonances in electron clouds in a positron storage ring. *Nucl. Instrum. Methods Phys. Res.*, A621:33–38, September 2010.

[42] M. T. F. Pivi, L. Wang, T. Demma, S. Guiducci, Y. Suetsugu, K. Shibata, K. Ohmi, G. Dugan, M. Palmer, J. A. Crittenden, K. Harkay, L. Boon, M. A. Furman, and C. Yin Vallgren. Recommendation for mitigations of the electron cloud instability in the ilc. In *Proceedings of the 2011 International Particle Accelerator Conference, San Sebastián, Spain*, pages 1063–1065, 2011.

[43] R. A. Rosenberg and K. C. Harkay. A rudimentary electron energy analyzer for accelerator diagnostics. *Nucl. Instrum. Methods Phys. Res.*, A453:507–513, October 2000.

[44] D. Rubin. Cesrta program overview. In K. Smolenski, editor, *Proceedings of ECLOUD 2010: 49th ICFA Advanced Beam Dynamics Workshop on Electron Cloud Physics, Ithaca, NY*, number Paper OPR06, in press.

[45] D. L. Rubin. The challenges of ultra-low emittance damping rings. In *Proceedings of the 2011 International Particle Accelerator Conference, San Sebastián, Spain*, pages 956–960, 2011.

[46] Y. Suetsugu, H. Fukuma, L. Wang, M. Pivi, A. Morishige, Y. Suzuki, M. Tsukamoto, and M. Tsuchiya. Demonstration of electron clearing effect by means of a clearing electrode in high-intensity positron ring. *Nucl. Instrum. Methods Phys. Res.*, A598:372–378, January 2009.

[47] Y. Suetsugu, K. Kanazawa, K. Shibata, H. Hisamatsu, K. Oide, F. Takasaki, R. V. Dostovalov, A.A. Krasnov, K. V. Zolotarev, E. S. Konstantinov, V. A. Chernov, A. E. Bondar, and A. N. Shmakov. First experimental and simulation study on the secondary electron and photoelectron yield of neg materials (ti-zr-v) coating under intense photon irradiation. *Nucl. Instrum. Methods Phys. Res.*, A554:92–113, December 2005.

[48] Yoshiaki Susaki and Kazuhito Ohmi. Electron cloud instability in superkekb low energy ring. In *Proceedings of the 2010 International Particle Accelerator Conference, Kyoto, Japan*, pages 1545–1547, 2010.

[49] C. Y. Tan, K. L. Duel, and R. M. Zwaska. An improved retarding field analyzer for electron cloud studies. In *Proceedings of the 2009 Particle Accelerator Conference, Vancouver, BC*, pages 3540–3542, 2009.

[50] C. Yin Vallgren, G. Arduini, J. Bauche, S. Calatroni, P. Chiggiato, K. Cornelis, P. Costa Pinto, B. Henrist, E. Métral, H. Neupert, G. Rumolo, E. Shaposhnikova, and M. Taborelli. Amorphous carbon coatings for the mitigation of electron cloud in the cern super proton synchrotron. *Phys. Rev. ST Accel. Beams*, 14, July 2011.

[51] F. Zimmermann, G. Rumolo, and K. Ohmi. Electron cloud build up in machines with short bunches. In K. Ohmi and M. Furman, editors, *ICFA Beam Dynamics Newsletter*, number No. 33, pages 14–24. International Committee on Future Accelerators, April 2004.